D 2019

**U.**PORTO

FEUP **FACULDADE DE ENGENHARIA**
UNIVERSIDADE DO PORTO

# STUDY OF VESTIBULAR REHABILITATION IN VERTIGINOUS SYNDROME USING A BIOMECHANICAL APPROACH

**CARLA BIBIANA MONTEIRO FRANÇA SANTOS**
TESE DE DOUTORAMENTO APRESENTADA
À FACULDADE DE ENGENHARIA DA UNIVERSIDADE DO PORTO EM
ENGENHARIA BIOMÉDICA

# Study of Vestibular Rehabilitation in Vertiginous Syndrome using a Biomechanical Approach

Carla Bibiana Monteiro França Santos

**D**

**2019**

Faculdade de Engenharia da Universidade do Porto

# STUDY OF VESTIBULAR REHABILITATION IN VERTIGINOUS SYNDROME USING A BIOMECHANICAL APPROACH

**CARLA BIBIANA MONTEIRO FRANÇA SANTOS**
TESE DE DOUTORAMENTO APRESENTADA
À FACULDADE DE ENGENHARIA DA UNIVERSIDADE DO PORTO EM
ENGENHARIA BIOMÉDICA

Supervisor: Professor Doutor Maria Fernanda Gentil da Costa
Co-Supervisor: Professor Doutor Jorge Américo Oliveira Pinto Belinha

Janeiro 2019

# Resumo

O sistema vestibular é a estrutura do ouvido interno responsável por manter o equilíbrio do corpo humano. Os três canais semicirculares em conjunto com o vestíbulo contêm as cúpulas e a mácula constituídas por células ciliadas que propagam a informação do deslocamento e posicionamento do corpo, através da circulação da endolinfa. A sua modelação computacional e consequente análise será o principal objetivo da presente tese. Existem diversas doenças associadas ao sistema vestibular, sendo a vertigem o sintoma mais usualmente relatado resultante desses distúrbios. A sensação de incapacidade resultante dos sintomas de vertigem e tonturas afeta uma grande parte da população, principalmente acima dos 60 anos. Hoje em dia, a reabilitação vestibular é a principal terapia aplicada nestes casos, e apesar dos resultados com elevada taxa de eficiência, trata-se de um processo empírico, que pode beneficiar muito de ferramentas como a simulação computacional. Este facto associado ao desconforto e instabilidade gerado pelas síndromes vertiginosas numa parte significativa da população são a principal motivação para este trabalho.

O modelo computacional do sistema vestibular foi construído recorrendo ao método de elementos finitos e foi desenvolvido por etapas, de forma a validar os diferentes procedimentos. A validação da metodologia utilizada para simulação do fluído foi o primeiro passo, sendo um método sem malha pela primeira vez utilizado para simular a endolinfa. Os resultados obtidos com o método *Smoothed Particle Hydrodynamics* e utilizando um canal semicircular foram comparados com outros autores que utilizaram métodos convencionais. A este modelo tridimensional do canal semicircular foi adicionada a cúpula, tornando o modelo mais próximo da situação real do sistema vestibular. O modelo construído foi validado experimentalmente utilizando um modelo de silicone. Após estas etapas de desenvolvimento, foi construído o modelo global do sistema vestibular com todos os seus constituintes, o qual permitiu simular a manobra de Epley num caso de síndrome vestibular com uma otocónia no canal horizontal, denominada de canalitíase. A recolha do movimento efetuado durante as manobras de reabilitação através de um acelerómetro foi também obtida de forma a ser realizada uma simulação correspondente ao movimento real.

Um outro estudo desenvolvido no decorrer desta tese, foi a análise das vibrações livres da cúpula do ouvido interno. Dois modelos da cúpula (um bidimensional e outro tridimensional) foram construídos dando origem igualmente ao desenvolvimento de uma análise numérica de comparação da performance de dois métodos sem malha com o método de elementos finitos no caso de estruturas biológicas. Neste estudo também foi analisada uma doença do sistema vestibular denominada, cupulolitíase; a qual ocorre quando as otocónias aderem à cúpula induzindo sintomas de vertigem.

No âmbito da sintomatologia da vertigem foi ainda realizado um estudo estatístico com uma amostra de mulheres jovens, de modo a investigar a influência da intensidade da atividade física nos sintomas de vertigem. Foi utilizado um questionário validado para recolher os dados relativos à sintomatologia (Dizziness Handicap Inventory), e a quantificação da atividade física dos participantes do estudo foi efetuada com recurso a um acelerómetro.

Assim, os métodos numéricos computacionais provaram ser uma ferramenta importante no estudo da biomecânica, e neste caso em particular apresentaram resultados fundamentais para a expansão do conhecimento na área vestibular. O desenvolvimento de um modelo computacional do sistema vestibular do ouvido interno, bem como das suas estruturas, permitiu avaliar as duas principais situações de síndrome vertiginoso onde é aplicada a reabilitação vestibular que correspondem à vertigem posicional paroxismal benigna: a canalítiase e a cupulolitíase.

# Abstract

The vestibular system is the inner ear structure in charge for maintaining the human body balance. The three semicircular canals and the vestibule contain the cupulas and macula, respectively; which have hair cells that transmit the information regarding the displacement and position of the body through the endolymph flow. The computational numerical modeling and analysis of the vestibular system was the main goal of the present thesis. There are several vestibular system disorders, being vertigo and dizziness the most commonly symptoms reported. The disability developed from those symptoms affects a wide population range, mainly elders. Nowadays, vestibular rehabilitation is the main therapy applied in these cases. Despite the high efficiency results obtained, it is still an empirical process, which can profit from tools such as computational simulation. This factor combined with the anxiety and instability developed by vertiginous syndromes in a significant part of the population is the main motivation for this work.

The computational model of the vestibular system was built using the finite element method and it was developed along distinct stages, in order to validate the different procedures. The validation of the fluid simulation methodology was the first step, being the endolymph simulated with a meshless method for the first time. The results obtained with the Smoothed Particle Hydrodynamics method and using a semicircular canal were compared with other authors using traditional numerical methods. The cupula was added to this three-dimensional model of the semicircular canal, allowing to achieve a computational model closer to the actual semicircular canal. The computational model was validated experimentally using a silicone model. After these development stages, the global vestibular system model with all its components was built, allowing to simulate the Epley maneuver in a vestibular syndrome condition with an otoconia in the horizontal canal, which is called canalithiasis. Using an accelerometer, the movement data during the rehabilitation maneuvers was acquired, allowing to perform a computational simulation of the corresponding actual movement.

Another development during this thesis was the free vibrations analysis of cupula of the inner ear, using two-dimensional and three-dimensional models. Considering this biological structure, a numerical comparison between two meshless methods and the finite element method was performed. A vestibular system disorder called cupulolithiasis was also analyzed; which occurs when the otoconia get attached to the cupula inducing dizziness symptoms.

Considering the dizziness symptoms, a statistical analysis was also performed using a young women sample aiming to investigate the influence of physical activity intensity on the vertiginous symptoms. A validated questionnaire (Dizziness Handicap Inventory) was used to obtain the symptoms data,

and the physical activity quantification was made using an accelerometer during a week routine of the participants.

Therefore, computational numerical methods proved to be an important tool in biomechanics, and in this particular work shown fundamental results for the knowledge expansion in the vestibular field. The computational models development of the vestibular system structures allowed the evaluation of the two main conditions of vertiginous syndrome where vestibular rehabilitation is applied, corresponding to benign paroxysmal positional vertigo: canalithiasis and cupulolithiasis.

# Acknowledgments

No entanto, e como o que faz as instituições são as pessoas, é ainda mais importante agradecer-lhes; começando pelos meus orientadores Doutora Fernanda Gentil e Doutor Jorge Belinha, quero agradecer pelo apoio constante ao longo de todo o processo, a disponibilidade a toda a hora para discutir ideias, e principalmente agradecer por todos os ensinamentos que me transmitiram ao longo do caminho nas áreas em que construíram as suas carreiras no campos da Audiologia e Engenharia Mecânica respetivamente. Ao meu coorientador, Doutor Marco Parente, agradeço por toda a disponibilidade demonstrada em resolver os desesperos com as simulações e principalmente por todo o conhecimento partilhado no domínio de qualquer software de elementos finitos. O Professor Renato Natal merece um especial agradecimento, que como responsável do grupo de Biomecânica, me ensinou ao longo do caminho, que há sempre um lado positivo em todas as coisas, por me desafiar a alcançar os objetivos e por me permitir partilhar o meu trabalho em várias conferências internacionais. Aos colegas do ouvido Bruno Areias e Carolina Garbe, agradeço a partilha de conhecimento computacional e motivação ao longo do processo.

Ainda na órbita das instituições não posso deixar de agradecer (muito!!) aos meus colegas, que ao longo do tempo se tornaram a minha "família do trabalho" e amigos fora do trabalho. A todos que animaram os meus dias, que jogaram à sueca depois de almoço, que pagaram cafés na máquina, que partilharam comida (muita!), que partilharam piadas, que me fizeram rir, que tornaram as conferências ainda mais interessantes, que me acompanharam a ir à Bia, que ouviram os meus desabafos, que marcavam jantares, viagens e eventos vários, que fofocavam comigo e que me ensinaram tantas coisas! Obrigada Ana, Daniel, Dulce, Elisabete, Hélder, Joana, Júlia, Karlon, Marco, Nilza, Sérgio, Sofia (e muchacho Rui!), Thuane (e Schmitt, muitas saudades!) e a todos os outros colegas que mais ou menos presentes contribuíram de alguma forma para este crescimento.

A todos os outros amigos que ao longo destes anos de tese (e de todos os anos anteriores) tiveram um papel no meu crescimento pessoal e profissional, que sempre me incentivaram nas minhas decisões, que estavam lá para me dar um abraço e construir memórias de alguma forma, que me fizeram sentir importante, e que fizeram todos os minutos valer a pena! Obrigada Adriana, Carol, Célia, Cláudia, Deco, Diana, Erica, Gi, Gonçalo, Gustavo, Ivan, João, Lena, Luís, Mota, Odila, Ori, Pedro, Pita, Prisca, Rita, Sara, Sofia, Sylvie, Vila, e a todas as outras pessoas não mencionadas que de uma forma ou de outra acabaram por influenciar o meu percurso.

Quero agradecer muito(!) à minha família pela preocupação, apoio e incentivo constantes, mas principalmente por todos os mimos, por pensarem em mim a toda a hora e por terem investido em mim de todas as formas; Obrigada por tudo Mãe, Pai, Avós (em especial à avó Esperança! <3), Avôs, Tias, Tios, Primas, Primos (em especial o que se tornou afilhado! <3), Madrinha e Padrinho. E um agradecimento especial ao meu Irmão por me aturar quase todos os dias, por me preparar deliciosos manjares e principalmente por me fazer rir, até de mim própria!

E claro(!), agradecer muito ao meu Namorado por todo o carinho, por todo o suporte técnico, por me ouvir sempre, por gostar de mim todos os dias, por me fazer rir (e por rirmos juntos), pelos belos jantares, por todos os momentos partilhados, por todas as milhas percorridas, por todos os brindes com mojitos e principalmente por me fazer acreditar que tudo vai ficar bem! Marcelo, i love you too.

# Abbreviations

**BPPV**    Benign Paroxysmal Positional Vertigo

**CNS**    Central Nervous System

**DHI**    Dizziness Handicap Inventory

**FEM**    Finite Element Method

**FSI**    Fluid-Structure Interaction

**NNRPIM**    Natural Neighbor Radial-Point Interpolation Method

**PA**    Physical Activity

**RPIM**    Radial Point-Interpolation Method

**SCC**    Semicircular Canal

**SCD**    Semicircular Duct

**SPH**    Smoothed Particle Hydrodynamics

# List of Figures and Tables

x

# Contents

# Chapter I
# Structural Overview

## 1.1.    Introduction

The inner ear is a sensory organ, lodged in the temporal bone, that comprises the vestibular system and the cochlea. The hearing function is supported by the cochlea and the vestibular system rules the balance [1], which is the focus of the present thesis.

The human vestibular anatomy consists of a membranous labyrinth filled with endolymph enclosed by a bony labyrinth with the same configuration, see Figure 1.1. Between both labyrinths circulates the perilymph [2]. The bony labyrinth consists in the three semicircular canals (SCCs), anterior, posterior, and horizontal; placed orthogonally and connected to a central chamber called vestibule. Consequently, the membranous labyrinth contains three semicircular ducts (SCDs) within the SCCs and the otolith organs, utricle and saccule, inside the vestibule. Moreover, each SCD comprehends an ampullar section which contain the cupula. The cupula contains hair cells embedded on a tuft of blood vessels and nerve fibers covered by a gelatinous tissue, which is related with the angular head movements [3]. Inside the utricle and the saccule it can be found the macula, which detects the linear head movement and it is constituted by three layers. The bottom layer contains the sensory hair cells and it is covered by a jelly layer, while the top layer (above it) is composed by calcium carbonate crystals, known as otoconia [2,4,5].

The hair cells from the cupula and the macula are mechanoreceptors which send electrical signals to the brain about the movement performed by the head related to the body position. The cupula deflection, leading to the hair cell movement, is driven by the endolymph flow, and the macula hair cells are forced to move, helped by the otoconia.

Balance physiology is a complex process, which coordinates the vestibular signals with the visual and proprioceptive sensors. The central nervous system (CNS) integrates the sensory information provided by each one of these systems in order to maintain posture and control static and dynamic balance [6]. These integrated pathways have an important role in vestibular disorders diagnosis, considering that eye movement assessment and posture analysis were used to infer the functional status of the vestibular sensory organs [7,8]. The reduced dimensions of the vestibular system are one of the main hindrance to obtain direct data from its sensory cells.
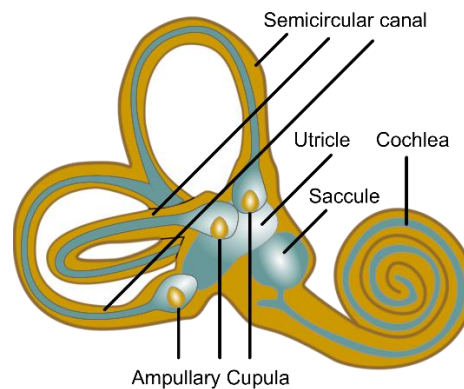


**Figure 1.1** – Scheme of the vestibular system.

All perturbations in the described process could induce vestibular syndromes. The pathologies that induce vestibular syndromes can have a peripheral or central origin. Peripheral disorders affect the end organ pathway, around or within the vestibular system, as benign paroxysmal positioning vertigo (BPPV), Ménière's disease, vestibular neuritis, bilateral vestibulopathy, vestibular paroxysmia, and superior canal dehiscence syndrome [9].

BPPV is the most common vestibular disorder, and it occurs when the otoconia are misplaced from the macula to the SCDs, inducing a vertigo sensation in the sensory cupula's hair cells [3,10]. The vertigo episodes start suddenly and last from a few seconds to minutes in severe cases. Furthermore, the dizziness spinning sensation is described by the patients as being an incapacitate condition, and it could happen in two distinct forms: canalithiasis and cupulolithiasis. During canalithiasis, the otoconia lost itself inside the duct path, and in the cupulolithiasis the otoconia attaches itself to the cupula. At the moment, the detachment of the otoconia debris from the macula is not entirely understood, however it is reported that impact sports or car accidents could lead to a BPPV condition, and it is also common during the usual aging process [11].

The main vestibular rehabilitation procedure applied to recover from canalithiasis consists in a set of personalized programed exercises, known as the otoconia repositioning maneuvers. After the diagnosis, where the affected canal is defined, the suitable maneuver is selected. The Epley or Semont maneuvers are applied when the posterior canal is affected, which is the most common occurrence, while the Gufoni or BBQ roll maneuvers are applied once a horizontal canal perturbation occurs [12]. Considering that the anterior canal is the least affected, there is no evidence on an effective maneuver, however, when it occurs, a reverse Epley maneuver is suggested.

Regarding the cupulolithiasis, the most common applied technique is an empirical shake of the head in order to detach the otoconia. However, there are only a few studies indicating which methodology is the most effective in each case. Some doubts remain to be clarified in cupulothitisis cases, for example to which side of the cupula are the otoconia attached, since such factor could influence the selection of the correct procedure to apply [13]. Additionally, medicines could be used, as a first clinical approach, in order to decrease the disturbing dizzy symptoms during BPPV episodes. In severe cases, surgery could also be required.

Besides the large success rates in decreasing the dizziness symptoms using vestibular rehabilitation, it is still an empirical methodology. The procedure integrated few evolutions since the maneuvers creation during the 80's [14,15]. Some rehabilitation protocols include limitations of movements, until some days after the procedure, which causes anxiety to several patients [16]. Furthermore, the vestibular rehabilitation fails in a certain amount of cases. Therefore, one of the leading authors in the vestibular rehabilitation field, recently stated that the negative response of some patients with the vestibular hypofunction exercises is not fully understood. Finally, there is lower evidence sustaining the efficiency of the maneuvers procedures applied in the horizontal and anterior canal BPPV, and also in the case of a  multiple-canal BPPV [17].

The demand for new and more effective therapies to use in all the BPPV cases (that do not have yet a stable solution) increase the need to deepen the knowledge on the vertiginous syndrome and related physiology.

## 1.2.   Biomechanical Background

Biomechanics could be defined as the study of biological structures, organisms or processes by an engineering point of view, essentially using mechanical tools. In the actual digital evolution era, the computational methods seem to be, most of the times, an economical way to reach approximate/satisfactory solutions in a short time span. Therefore, the methodologies used in this research to analyze the biomechanics of the human vestibular system described in the previous chapter are the computational numerical methods, mainly the finite element method (FEM). The FEM is one of the most common discrete numerical tool used to solve complex problems, such as domains with irregular geometries or structures built with materials showing a non-linear behavior, which are common features in biological systems. FEM is a mathematical method fully developed in the 60's. Usually the problem domain is divided into small parts called finite elements with the same properties [18]. The behavior of these elements can be described using variational methods (a particular application of differential equations) in order to minimize the system total energy and obtain the approximated solution. This method is widely used in some scientific fields, including several biological researches to reproduce human systems, due to its great flexibility and efficiency. Combined with a constitutive equation, FEM allows the analysis of displacements, stresses and strains, among other measurements [19].

In order to discretize the problem domain, the FEM divides the problem domain into finite elements, which can be triangular or quadrilateral elements in 2D analyses, or tetrahedral or hexahedral elements in 3D analyses. The sum of the volumes of each element is numerically equal to the volume of the discretized domain. The elements are composed by nodes, generally placed at the corners and boundaries of the finite element shape. Neighbor elements share common nodes, naturally enforcing the connectivity in FEM. There are some advantages in this kind of discretization, such as an easy representation of the complete domain and an accurate representation of the geometry. There are some steps that are important to follow in this technique, after defining the mesh it is necessary to attribute properties to the materials (in heterogeneous domains, each element can be associated with a distinct material). Then, after calculating the stiffness matrix of each element and establishing the global system of equations, the displacement field is obtained (the solution). With the displacement

field, it is possible to calculate the associated strain and stress field. The difference between the final deformation and the initial state of the model and the material properties define the strain/stress distribution. Other important parameters to define are the boundary conditions of the full model and the applied forces. After all the conditions are defined, it is possible obtain several mechanical results related to the model.

Although the FEM is often used with solids, it has some applications with fluids and the present study requires a Fluid–Structure interaction (FSI) approach, due the physiology of the vestibular system [19]. FSI attempts to predict the interaction of a deformable structure with an internal or surrounding fluid flow [20]. This technique plays an important role in many scientific and engineering fields, and it has been a challenge mainly for problems related with human body research, due to the strong nonlinearity and multidisciplinary nature [21]. The simulation of FSI can have two main approaches: the monolithic approach and the partitioned approach. If the equations governing the fluid flow and the displacement of the structure are solved simultaneously, it is called monolithic approach, which is the method applied in the present work. This approach leads to better approximation for a multidisciplinary problem, but it may require more computational resources [21,22].

One of the main challenges of the present work was the decision about the fluid simulation methodology. The alternatives considered to simulate the vestibular fluid were the Coupled-Eulerian Lagrangian (CEL) Method, the Computational Fluid Dynamics (CFD) and the Smoothed Particle Hydrodynamics (SPH) method. SPH was the selected option, mainly due to some software limitations regarding the other methods and also their computational cost.

Briefly, the SPH is a meshless numerical method used for simulating fluid flows. It is based in the Lagrangian formulation, in which the domain is divided in particles possessing a constant mass (mass conservation principle), the mesh is attached to the material and the particles deform as the material starts to deform. The resolution of the method can easily be adjusted with respect to variables, such as the density [23–25]. A comprehensive description of the SPH formulation will be shown in the developed work, mainly in Contribution I, presented in Chapter II.

The main software packages used in the present research for the vestibular model development and simulation, using FEM and SPH approaches, were ABAQUS and FEMAP. The work developed with these software is presented mostly in Contributions II and III in Chapter II.

Other meshless methods applied during the developed work, mainly in the research focused on the cupula, were the RPIM (Radial Point Interpolation Method) and NNRPIM (Natural Neighbor RPIM), using the academic software FEMAS (cmech.webs.com). Both meshless methods discretize the problem's domain with a cloud of nodes [26–30], instead of the rigid element concept used in FEM. In the early years, the solution of partial differential equations was the main focus of interest [27]. However, today, meshless methods are applied to a wide-range of applications [29]. In the present thesis, a free vibration analysis of the cupula was performed, using the RPIM and NNRPIM formulations. The corresponding results and conclusions obtained are demonstrated in the Contributions IV and V in the Chapter II.

## 1.3.    Motivation and Aim

The literature shows that 85% of balance dysfunctions could be related with inner ear disorders [31]. Furthermore, complains described as dizziness or vertigo, usually unbalance symptoms, are the most common medical complains [32,33]. Additionally, blurred vision, nausea, and complications in standing and walking could, also, occur as a consequence in a BPPV episode [34]. These incapacitating symptoms result from conflicting information received by the brain and the vestibular system concerning the body's position and movement [31]. Among the vestibular disorders, the BPPV is the most common cause of vertigo [35,36], affecting females twice as often as males [4,36]. Dizziness is present in all age ranges, although its prevalence increases with ageing, being the most frequent illness among elders. In Europe, the dizziness prevalence for ages between 50 and 80 years old is 12.4%, while in Portugal dizziness related hearing problems affect 28.7% of the same age group [37]. Thus, dizzy symptoms are the main focus of the Contribution VI, presented in Chapter II.

People suffering from vertigo and dizziness have a higher risk experiencing falls and depression. Furthermore, falls are one of the main causes of accidental deaths and bone fractures in

older patients [38]. The health care related with those fractures involves high costs and higher limitations; therefore, in order to avoid such expenses, and, at first instance, avoid the disable dizzy symptoms, it is important to decrease the number of people suffering from dizziness [38,39]. In light of the rising average life expectancy, vertigo should be viewed as a core health concern.

Based on all the reported facts, besides the biomechanical and vestibular research, it is possible to summarize the aims of the present thesis as:

- Literature review of the biomechanical models of the vestibular system, related structures and their analysis;
- Development of a functional computational geometric model of the vestibular system with all the meaningful structures using mechanical engineering tools;
- Simulation and direct validation of the endolymph fluid including the otoconia movement during the rehabilitation maneuvers;
- Validate the application of numerical tools as FEM, SPH, RPIM and NNRPIM to mimic the behavior of biological structures;
- Consider new application methodologies in the vestibular disorders field in order to numerically analyze the system response;
- Contribute to a better knowledge related with the vestibular rehabilitation process and physiology;
- Analyze the impact of physical activity in the dizziness symptoms in order to promote accurate and reliable clinical indications to the patients;
- Production and publication of the research outputs in international journals.

# Chapter II
# Original Developed Work

## 2.1. Introductory Remarks

The evolution of the FEM vestibular full model is explained in the first three publications of the present work. The first publication (2.2.1. Contribution I) presented the first SCC model, essential for the validation of the formulation used to simulate the endolymph. The second publication (2.3.1. Contribution II) contributed to the development of a methodology to simulate the real maneuvers performed to the patients. Following the previous achievements, the third paper (2.4.1. Contribution III) shows a model evolution, including all the vestibular structures, where an experimental validation was performed.

The next step after the global model analysis consisted in a detailed evaluation of the cupula behavior. The natural frequency vibrations of the cupula were obtained applying two distinct meshless methods; the NNRPIM (2.5.1. Contribution IV) and the RPIM (2.6.1. Contribution V) in order to theorize about an improved procedure to manage cupulolithiasis.

Maintaining the vestibular disorders target, while diverging from the biomechanical simulation scope, a statistical research was performed (2.7.1. Contribution VI). The goal was to analyze the influence of the physical activity intensity in the vertigo symptoms.

The present chapter includes the main highlights of all the contributions and publications, presented as an extended graphical abstract. Furthermore, the complete contributions can be found next.

10

## 2.2. Highlights of Contribution I

This contribution focused on the numerical simulation of the endolymph, for the first time, using the SPH methodology.

Therefore, the main contents of this publication include:

   I.   Literature review on vestibular system mechanical models;

   II.   SPH methodology applications and formulation;

   III.   One SCC FEM model construction, with the ampullar part:

Being the main aims of the present paper to validate the SPH method and to simulate the vestibular system fluid (as part of a global goal of the thesis of building a FEM vestibular system model), an elementary ring shape with an ampullar part seems to be a reliable profile model. Furthermore, expectably, such simple geometry would lead to low computational costs. Therefore, the model presented in Figure 1.2 was built using ABAQUS, with the membrane built with shell elements, and also containing the SPH particles inside, to simulate the fluid. Additionally, three different fluid discretization meshes were considered and simulated. The properties used in the model were obtained from the literature.
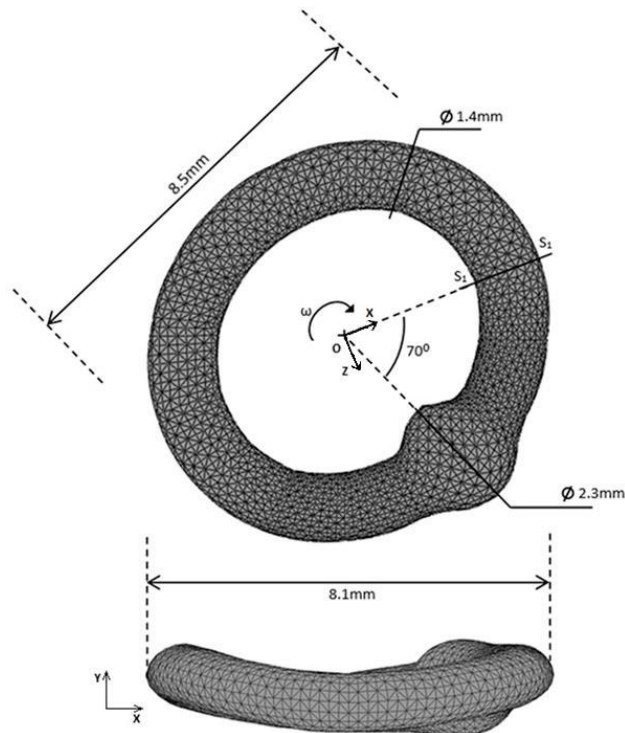


**Figure 1.2** - Model of the SCC membrane built with FEM, front and top view.

IV.   Simulation of two angular velocity time steps as boundary condition;

V.    Acquisition of global and sectional fluid velocity;

VI.   Validation of the obtained results by comparison with other solutions available in the literature:

In order to compare the results obtained with other authors with similar models of the SCC, the fluid discharge in a similar section of the canal was acquired (pointed as section $S_1$ in Figure 1.2). Figure 1.3 shows the results obtained along the simulation time with the two different time steps, applied as ω shown in Figure 1.2, and compared with the works of Selva, P. *et al.* [40] and Caiqin, WU., *et al.* [5].
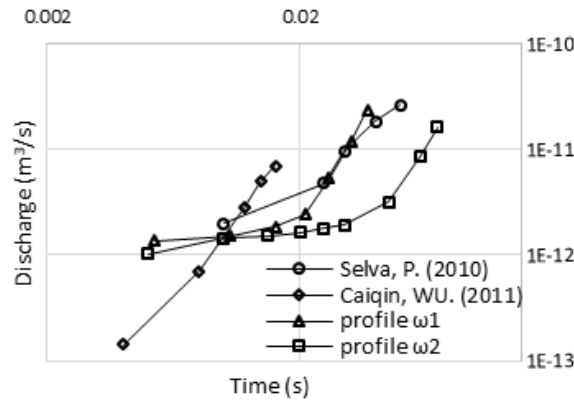


**Figure 1.3** – Comparison of the fluid discharge in section $S_1$ using the two different applied velocity profiles; with the literature.

VII.  Conclusion about the SPH performance as a vestibular fluid:

As main conclusion of the present contribution, the authors concluded that the SPH methodology is a reliable alternative approach of the endolymph simulation. Moreover, the solutions produced with this fluid-structure model were close to other authors, with the advantage of using a particle method, which allows an easier interaction with other geometrically complex structures, as the case of the otoconia in the upcoming SCC model.

The complete document can be found in the next sub-chapter.

## 2.2.1.    Contribution I

## An alternative 3D numerical method to study the biomechanical behavior of the human inner ear semicircular canal

# An alternative 3D numerical method to study the biomechanical behaviour of the human inner ear semicircular canal

Carla F. Santos[1]*, Jorge Belinha[1], Fernanda Gentil[2], Marco Parente[3], Renato N. Jorge[1]

[1] Faculdade de Engenharia Universidade do Porto – FEUP, Porto, Portugal.
[2] Clínica ORL-Dr. Eurico Almeida, Widex, ESTSP, Portugal.
[3] Instituto de Ciência e Inovação em Engenharia Mecânica e Engenharia Industrial – INEGI, Porto, Portugal.

*Purpose*: The vestibular system is the part of the inner ear responsible for balance. Vertigo and dizziness are generally caused by vestibular disorders and are very common symptoms in people over 60 years old. One of the most efficient treatments at the moment is vestibular rehabilitation, permitting to improve the symptoms. However, this rehabilitation therapy is a highly empirical process, which needs to be enhanced and better understood. *Methods*: This work studies the vestibular system using an alternative computational approach. Thus, part of the vestibular system is simulated with a three dimensional numerical model. Then, for the first time using a combination of two discretization techniques (the finite element method and the smoothed particle hydrodynamics method), it is possible to simulate the transient behavior of the fluid inside one of the canals of the vestibular system. *Results*: The obtained numerical results are presented and compared with the available literature. The fluid/solid interaction in the model occurs as expected with the methods applied. The results obtained with the semicircular canal model, with the same boundary conditions, are similar to the solutions obtained by other authors. *Conclusions*: The numerical technique presented here represents a step forward in the biomechanical study of the vestibular system, which in the future will allow the existing rehabilitation techniques to be improved.

*Key words*: vertigo, biomechanics, finite element method, vestibular system, fluid mechanics, inner ear

## 1. Introduction

### 1.1. Vestibular system

The manifestation of an organic problem associated with body balance is usually known as vertigo. This symptom is one of the most common medical complaints, affecting approximately 20%–30% of the world population [29]. Vertigo may be present in patients of all ages. Nevertheless, its prevalence increases with age, being the most frequent complaint in people over 70. Vertigo predominance is also associated with gender, being about two to three times higher in women than in men [17]. This disorder is an indicator of conflicting information being received by the brain. Some studies pointed out that 85% of balance dysfunctions could be related with inner ear disorders [6], mainly with the vestibular system. The vestibular system is the sensory system located in the inner ear that provides the leading contribution for movement and sense of balance.

Since human movements consist in rotations and translations, the vestibular system comprises two main components. One of the main components is the semicircular canals (SCC) system. Involving three canals placed orthogonally, the SCC is responsible for the detection of the rotational movements. The other main component is the set of otoliths located inside the utricle and the saccule. With the movement, these particles induce mechanical stimuli in the utricle and

the saccule cilium and linear accelerations are identified by the brain through electrical signals [10]. The main vestibular structures are represented in Fig. 1.
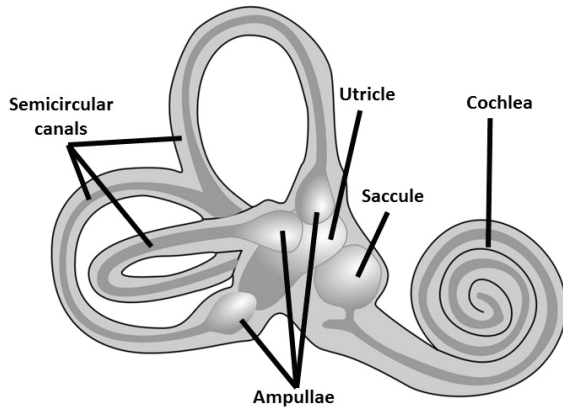


Fig. 1. Scheme of the human inner ear and the vestibular system

Each canal (Fig. 2) is comprised of a circular path filled with fluid, interrupted at the ampulla, which contains the sensory epithelium. The hair cells of the ampulla rest on a tuft of blood vessels, nerve fibers, and supporting tissue called the cupula [10]. The endolymph, inner ear fluid, is a complex component of the vestibular system. The correct computational simulation of the endolymph is a challenging and important task, since the endolymph influences significantly the maintenance of balance.
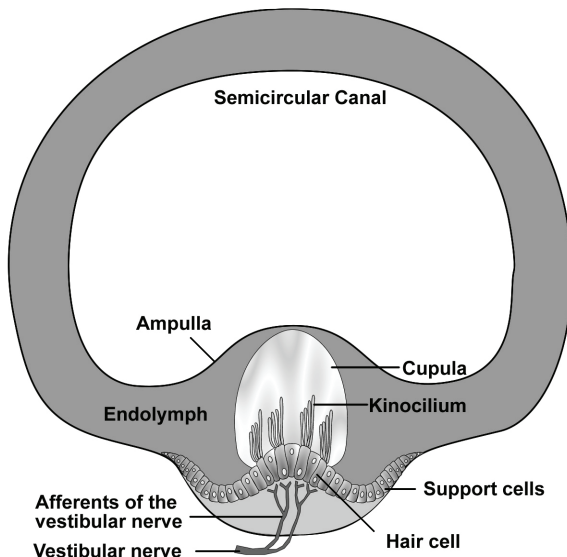


Fig. 2. Scheme of the human vestibular system – SCC

The sensory cells exhibit constant discharge of neurotransmitters, which are modified by the direction of the cupula deflection. This output signal is induced by the head rotation. Generally, these cells are called "sensors" in engineering terms.

Disorders in the vestibular system play a critical role in the quality of life of the older population. Frequently, in order to decrease the symptoms, drugs are used to suppress the activity of the inner ear. Additionally in some cases, combined with or without drug administration, physical head manoeuvres are performed within the scope of the vestibular rehabilitation program [11]. However, these manoeuvres are based on a set of empirical moves made by an audiologist, which has an associated high variability and could lead to inaccurate moves. The rehabilitation process, and even the vestibular system behaviour, can be analysed from the biomechanical point of view, taking into consideration its movements and component interactions during balance.

## 1.2. Biomechanical models of the vestibular system

In 1933, when the first investigations of the vestibular system were performed, Steinhausen formulated a mathematical description of the SCC which considered the dynamics of the cupula endolymph system as a highly damped torsion pendulum for the sensation of the angular motion [25].

The simulation of the fluid structure interaction between the endolymph and cupula during head rotation allows the measurement of the fluid interactions between the three ducts and the displacement of the cupula during the movement. This model could be considered useful to understand the physiological and mechanical aspects of SCC. Additionally, this model can be described as a band-pass filter relating the displacement of the cupula to the angular velocity of the head [30].

Van Buskirk and co-workers performed the first work focused on the fluid dynamics of the SCC. These researchers assumed that the endolymph has the properties of an incompressible Newtonian fluid [14], [27].

Some mathematical models have been made through the years to represent some parts of the vestibular system.

Table 1 describes the main studies related with the vestibular system and summarizes the studies with finite element models described below. Most of the research performed for vestibular system focuses only on one element of the system, usually the endolymph or the otolithic membrane. The vestibular system, however, is an integrated and complex structure, making it important to understand its function as a whole.

Table 1. Summary of numerical models related to vestibular system

|  | Kassemi et al. [14] | Kondrachuk [15] | Davis et al. [4] | Shuang Shen et al. [23] | Jaeger et al. [13] | Duncan and Grant [5] | Grieser and Obrist[7] |
|---|---|---|---|---|---|---|---|
| Main focus | Endolymph interaction | otolhotic membrane behaviour | otolhotic membrane behaviour | cupular deflection during caloric test | otolhotic membrane behaviour | cillium behaviour | Endolymph behaviour |
| Methodological approach | Arbitrary Lagrangian Eulerian (ALE), fluid–structural interaction (FSI) | Static analysis | Linear interpolation | caloric test, Arbitrary Lagrangian Eulerian (ALE), Comprehensive grid convergence tests | Cauchy's equation of motion | NA | quasi-steady Stokes flow regime |
| Material properties | Newtonian weakly compressible fluid | isotropic elastic parameters, | anisotropic and viscoelastic material properties, linear elastic, Kondrachuk's modeling efforts | slightly compressible Newtonian fluid | visco-elastic properties, Kelvin–Voight fluid, homogeneous isotropic materials | isotropic, linear elastic materials with circular cross-sections | NA |
| Boundary constraints | Non-slip stationary | one side of plate was fixed and other side is free from stresses | the neuroepithelium was fixed and the force was acting in the macular plane | Nonslip boundary conditions | the nodes at the gel-skull boundary was fixed | The stereocilium was fixed to the base | standard head maneuver, no-slip condition. |

The models used in these studies are mostly based on previous geometries and only two of them were built from original images [4], [12].

Each study uses a different methodology mainly due to the different kind of goals of each research. The material properties vary according to the components being studied: Newtonian compressible fluid for endolymph studies and viscoelastic and isotropic properties for otolithic membrane studies.

The complexity of the vestibular system leads sometimes to model simplifications; for example, Suhrud Rajguru and co-workers [20] studied just one SCC instead of the whole system [20]. The 3D geometrical model was built from temporal bone histological sections and it was considered as a rigid structure. The study permitted to estimate the dynamic cupular and endolymph displacements during maneuvers [20].

Kondrachuk [15] developed a model of the otoconia membrane structure based on the Finite Element Method (FEM). This study allowed the mechanical parameters of the structure to be assessed. This model was also used to study the effect of the endolymphatic pressure on the otolithic membrane deformation. This research work concluded that the perception of inertial acceleration can be changed by the fluid redistribution due to the endolymphatic pressure [15]. In the literature it is possible to find another FEM model of the otolithic membrane [4]. This model showed the importance of 3D models in the global comprehension of the structural response. The geometrical variables studied were: the curvature of the surface, thicknesses of the three layers and the shape of the perimeter. The simulations permitted to analyze the static mechanical gain in each variable and the results showed that the three variables affected the magnitude and directional properties of the otoconia membrane [4].

An SCC model using virtual reality, to simulate the surrounding physical environment, was developed by Selva et al. [21]. The aim was to represent the vestibular sensors and simulate several rotation movements of the head occurring during a diagnosis of the vestibular system disorder. It can be used as a learning and demonstrating tool to understand the behavior of the sensors during any kind of motion [21].

A recent paper from Shen et al. [23] showed a caloric response of a complete vestibular system obtained by FEM analysis. The results of the caloric test on the model developed show the efficiency of the analysis on the evaluation of the functionality of the horizontal canal [23].

Another FEM simulation was presented by Jaeger et al. in 2002 [13]. The results show that the curvature of the maculae surface has no effect on the mechanical response, since the elastic coupling in the otolith membrane is insufficient [13].

Duncan and Grant [5] presented a study focusing on just one part of the vestibular system mechanics: the hair cells in the cupula. The FEM model representing the hair cells was used to better understand the mechanotransduction phenomenon [5].

Dominik Obrist et al. [18] proposed a simple numerical model to study the canalithiasis phenomenon, which is a condition that leads to a vestibular disorder called Benign Paroxysmal Positional Vertigo (BPPV). The work demonstrated that variations in the cross sectional area of the SCC are not necessary conditions for a positional nystagmus [18].

In the vestibular field, a new mathematical tool has been developed by Bradshaw et al. [2] for modeling the three dimensional geometry of SCC in humans. The main goal of the methodology is to understand the physiology of these canals. The technique devel-

oped allows the SCC geometry to be automatically reconstructed based on computed tomography images. After this step, the geometrical model is mathematically modeled using Fourier equations. The aim of this model is to help the diagnosis and clinical treatment of BPPV in each patient [2].

In the literature, there are other research studies focusing on the determination of coefficients that are a non-linear function of the morphological parameters of the SCC system. Thus, a mathematical model of the SCC mechanics was constructed for this purpose [28]. The work performed by Vega et al. [28] is based on Steinhausen's work, which uses a linear model of the torsion pendulum to study the dynamics of the cupula-endolymph system. The proposed model focuses on the mechanical coupling of angular accelerations with the movement of the sensory hair cells. The mechanical coupling largely determines the type of mechanical stimuli that is responsible for activation of hair cells [28].

There are already some studies on the fluid mechanics of the SCC that show that endolymph is a transducer for angular velocity of the head [27].

Grieser and Obrist [7] studied the endolymph motion of one SSC using FEM. The simulations performed consisted of a head rotation from a relative angle of 0° to 120° (a standard head maneuver). The rotation axis is oriented perpendicularly to the plane of the horizontal SCC. During the acceleration of the head, the walls of the SCC displace the adjacent fluid layer along their path. The work confirms the validity of all assumptions that were made in previous studies of the endolymph motion [7].

A fluid dynamic model of the vestibular system was proposed to understand the fluid/solid interaction phenomenon occurring between the thin membrane, separating the SCC from the cupula, and the endolymph flow [3]. Using real mechanical and anatomical parameters, a realistic vestibular model was also built using a 3D printer in order to study the best way to mimic the vestibular system [3].

In the field of mathematical models, another study was performed to examine two mechanisms proposed for BPPV [24]. The research concluded that a larger volume displacement on the cupula could be originated from larger or multiple otoconia [24].

Beyond the computational simulation, there are some research studies using in vitro models of the SCC. Valli et al. [26] performed some simulations using animal isolated posterior SCC to investigate if otoconia can produce transcupular pressures able to stimulate ampullar receptors. Obrist et al. [19] published an in vitro research work regarding the study of canalithia-sis, which confirmed the fundamental mechanism of BPPV [19].

Within the same topic, Selva et al. [22] developed a 2D finite element model of a single SCC, for which the displacements and velocities of the cupula were analyzed.

The aim of the present work is to study the mechanical behavior of the vestibular system in order to develop new and more efficient techniques to assist the vestibular rehabilitation, helping to avoid in the near future the high costs and problems associated with these symptoms.

Under these assumptions the use of engineering tools, such as the computational analysis, is an opportunity to create virtual simulations close to the real scenarios [8]. Thus, to achieve this goal, a 3D SCC model similar to the real system was constructed. The SCC is discretized with the FEM and the endolymph is simulated with the smoothed particle hydrodynamics method.

# 2. Smoothed Particle Hydrodynamics

The fluid/solid interaction is a highly demanding topic in computational mechanics. Nowadays, the Smoothed Particle Hydrodynamics (SPH) is one of the most popular numerical methods to study such phenomenon. The SPH can be used to simulate body fluids with low velocities, such as hemodynamics [16].

The SPH method works by dividing a continuous field into a set of discrete sample points, called particles. These particles have a spatial distance, over which their properties are "smoothed" by a *kernel function*. The kernel function helps to ensure the stability of the numerical solution [16]. The particles are identified with some characteristics such as mass, position and velocity. Additionally, particles can also carry estimated physical properties depending of the problem, such as mass-density, temperature and pressure.

The SPH approximation is based on two steps, the first one is the kernel approximation and the second is the particle approximation [16]. The result of the first step is the following quantity function

$$f(x) = \int_N f(x')W(x - x', h)dx' \qquad (1)$$

where $x$ is any point in $N$, the support domain, and $W(x - x', h)$ is a smoothing kernel function. The

smoothing length, $h$, defines the influence area of the smoothing function $W(x - x', h)$ [16]. This parameter can be fixed in space and time, however, this procedure does not take advantage of the full power of SPH. Thus, assigning to each particle its own smoothing length and allowing it to vary with time can lead to an automatic adaptation of the simulation resolution depending on the local conditions [16].

There are two main functions leading to equation (1), $f(x)$ and $W(x)$ as demonstrated below. The basis of integral representation of a function used in SPH is the function that represents the three dimensional position vector $x$,

$$f(x) = \int_N f(x')\delta(x - x')dx' \qquad (2)$$

where $\delta(x - x')$ represents the Dirac delta function given by

$$\delta(x - x') = \begin{cases} 1 & x = x', \\ 0 & x \neq x'. \end{cases} \qquad (3)$$

If the delta function of equation (3) is replaced in equation (2) by the smoothing function $W(x - x', h)$, it is possible to obtain equation (1). The particle approximation plays an important role within the SPH method. Consider Fig. 3, in which a set of particles possessing individual mass are scattered in space.
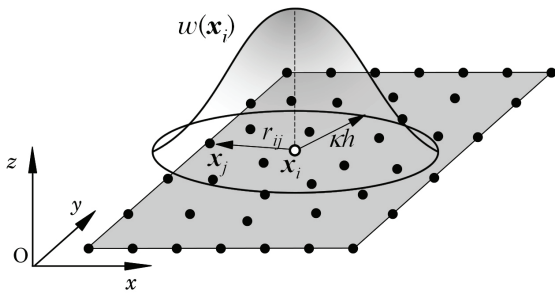


Fig. 3. Particle approximation. $W$ function of particle $i$

The mass of a particle is defined by the relation between the density and the volume by the following expression

$$m = V\rho. \qquad (4)$$

Thus, the function approximation for a particle $i$ can be represented by equation (5), with the infinitesimal volume $dx'$ in the above equations being replaced by the finite volume of the particle $j$.

$$f(x_i) = \sum_{j=1}^{N} \frac{m_j}{\rho_j} f(x_j)X(x_i)W(x_i - x_j, h) \qquad (5)$$

where $\rho_j$ is the density of each particle in the domain $N$ and $m_j$ is the mass of each particle.

The SPH was first developed to simulate astrophysical phenomena. Afterwards, it has been successfully applied to a vast range of problems, such as explicit fluid flow analysis. It was developed by Gingold and Monaghan (1977) and Lucy (1977) and it can be combined with the governing equations of the classical Newtonian hydrodynamics [16].

Within the SPH, the computational domain is represented by a set of computational points – particles – completely discretizing the problem domain.

This method has some advantages over grid-based techniques because its concept is simple and it is relatively easy to incorporate complicated physical effects into the SPH formalism [16].

Liu et al. [16], after some tests with SPH conditions, proposed a reproducing kernel particle method, which improves the accuracy of the SPH approximation.

The SPH method was initially developed as a probabilistic meshfree particle method and was later modified to a deterministic meshfree method [16].

There are several applications for the SPH method [1], [16]. One advantage of this method is the adaptability of the particles to many fields and subjects. For instance, the SPH was already used in astrophysical studies to study galaxies, the star formation process and even to simulate cosmological impacts [16].

Additionally, the SPH is capable of solving efficiently high velocity impact problems. Benz and Asphaug used the SPH method to simulate the fracture of brittle solids. In 2000, this method was also applied in the metal forming processes [1].

The SPH presents several advantages when compared with other numerical methods. The SPH deals efficiently with large local distortions of the discretized domain, it permits the mass conservation of the particles. It allows calculating the pressure by neighboring particles and not by solving linear equations and it is suitable to simulate the fluid free surface and the fluid/solid interactions.

Furthermore, SPH is well-known in the computational mechanics research community by its efficiency in the simulation of fluids motion. The first fluid flow application of the SPH was performed by Swegle with elastic flow. Later, Morris applied the SPH to solve magneto-hydrodynamics and Morris and Monhagan solved multi-phase, quasi-incompressible flows, gravity currents, flow through porous media, heat conduction and shock simulations. In 1995, Cleary applied SPH in heat transfer and mass flow [16].

Over the years, the method has been optimized in order to increase the solution accuracy and to enlarge the application field.

# 3. Methods

This work used the commercial software ABAQUS® to build and analyze the 3D model of the SCC. The analysis combined both the FEM and SPH methods.

## 3.1. Numerical model of the SCC

The 3D model developed was composed of two main parts: a small shell ring, representing one SCC with the cupula, as shown in Fig. 4, and the particles representing the endofluid.

The measures of the SCC represented in Fig. 4 were obtained from a 3D model of the complete vestibular system that can be found in the work of Henson et al. [9], which was constructed based on magnetic resonance imaging with fine resolution. In Fig. 4, it is only possible to visualize the outer FEM shell, which represents the vestibular membrane of the SCC. This shell was defined as a rigid body, because it does not present significant deformations. The particles defining the endofluid are inside the shell. The particle distribution is regular and the sum of the particles volume is equal to the volume of the SCC with the cupula.

Table 2 shows the material properties for the endolymph and the outer membrane. These values were obtained in the literature for the components of the vestibular system.

Additionally, in order to validate the model, three distinct particle discretizations were considered and analyzed: mesh M1 (1790 particles), mesh M2 (7410 particles), and mesh M3 (13637 particles).



Fig. 4. Model of one SCC built with finite elements, front and top view

## 3.2. Boundary conditions

Regarding the essential boundary conditions, to each node of the elements belonging to the membrane a prescribed angular velocity ($\omega = \pi/2$ rad/s) is enforced, accordingly with Fig. 4. The angular velocity, with respect to point O, is a time dependent function.

In order to analyze the biomechanics of the SCC model, two distinct angular velocity functions were considered: profile $\omega 1$ and profile $\omega 2$. Both functions are shown in Fig. 6. Both angular functions were enforced to the three discretized models presented in Fig. 5b–d. The functions considered were previously used by Selva et al. [22] and Wu Cai-qin et al. [30].

Additionally, in the present model, the density and volume of each particle were assumed, as Table 2 indicates. Thus, this model considers the gravity acceleration along the $zz$ axis, following the referential indicated in Fig. 4.

Regarding the contact between the distinct discrete elements of the model, the SPH formulation rules the contact between the particles. The general contact between the membrane elements and the fluid particles is performed explicitly by ABAQUS.

In order to compare the results from the several models considered in Fig. 5, the instantaneous and local discharge variable was used. The discharge is the

Table 2. Material properties of the model [39]

| Component | Young's modulus [Pa] | Poisson's ratio | Density [Kg/m$^3$] | Viscosity [Pa.s] |
|---|---|---|---|---|
| Endolymph | – | – | $1.0 \times 10^{-3}$ | $4.8 \times 10^{-3}$ |
| Membrane | 5.0 | 0.48 | – | – |

The model shown in Fig. 5a represents the outer membrane of the SCC. In Fig. 5b–d, it is possible to visualize the particles discretizing the endolymph, which were used by the Smoothed Particle Hydrodynamic (SPH) method to simulate the fluid flow.
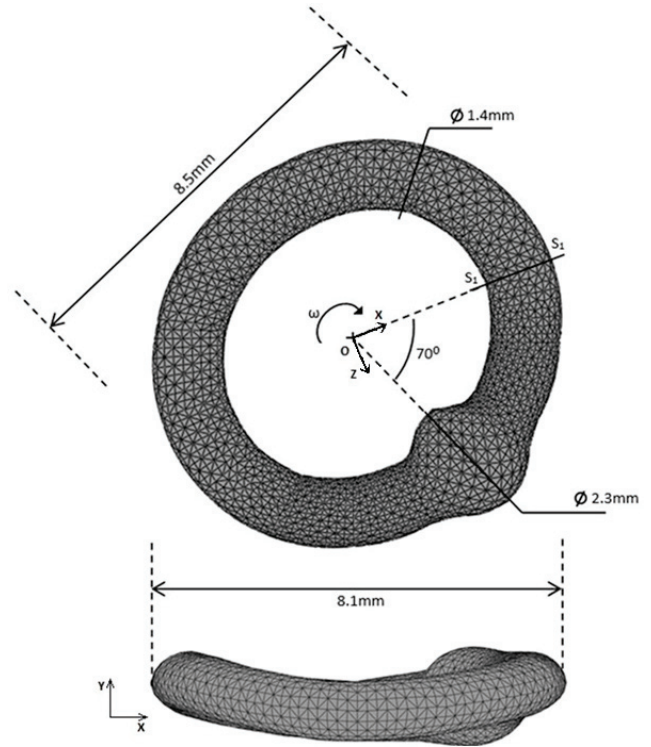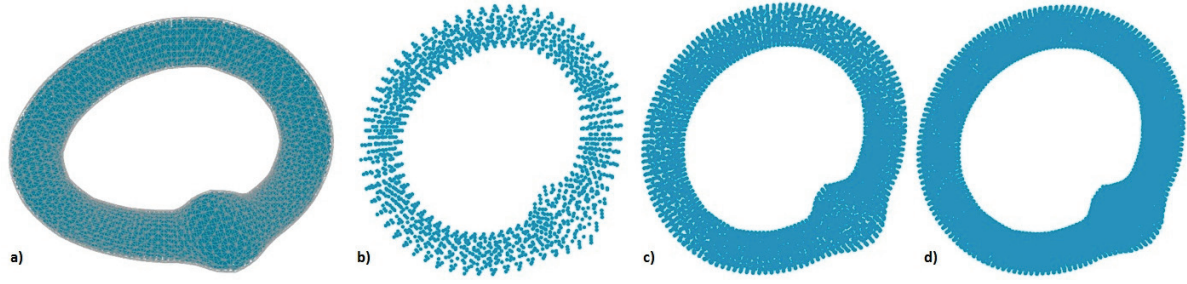
Fig. 5. Model of the SCC FEM mesh (a). Examples of the particle discretization:
(b) 1790 particles, (c) 7410 particles, (d) 13637 particles

volume rate of fluid flow transported through a given cross-sectional area. The discharge is calculated by the following equation

$$Q = v \times A \tag{6}$$

with $v$ being the fluid average normal velocity at a given cross-section and $A$ the area of that cross-section. The section analyzed in this work is indicated in Fig. 4 with the line segment $S_1$. Furthermore, the results from works [22], [30] were processed in order to present the discharge values of those and permit a valid comparison with the results obtained here.
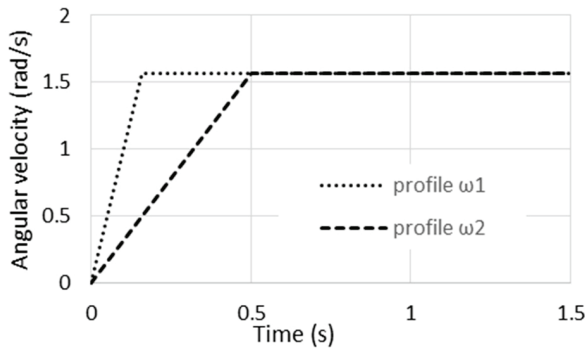


Fig. 6. Representation of the two angular velocity functions imposed in the model

## 4. Results

After the simulation of the rotational motion of the SCC 3D model presented in Fig. 4, the obtained results were processed and compared with other similar works in the literature [22], [30].

A comparison of the discharge variable for distinct time steps of the full analyses is presented in Fig. 7.

Figure 8 shows the comparison between the discharge obtained with each of the three meshes presented previously and the works of Selva et al. [22] and Wu Caiqin et al. [30].

In order to perceive the model behavior during the imposed angular velocity, the velocity of the fluid over time was analyzed.

The fluid velocity, at some instants of the simulation, is presented in Fig. 9. As it is perceptible, the inner fluid velocity increases with time, as expected.

After the general analysis of the global domain, a section of the SCC was analyzed in detail. The results were obtained for the section marked as S1 in Fig. 4. Figures 10 and 11 correspond to profile $\omega 1$ and profile $\omega 2$, respectively, and show the 2D sectional view on the left side and the velocity 3D distribution on the right side.
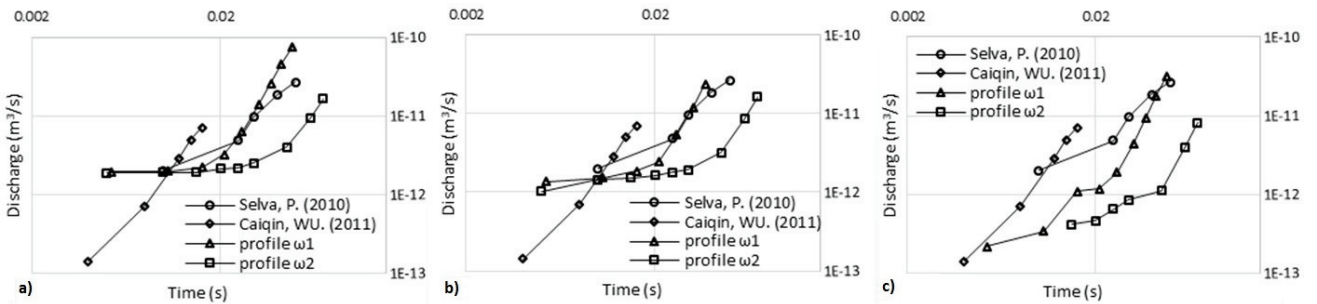


Fig. 7. Discharge of the fluid in the chosen section with the three meshes and comparison
with (a) M1, (b) M2, (c) M3
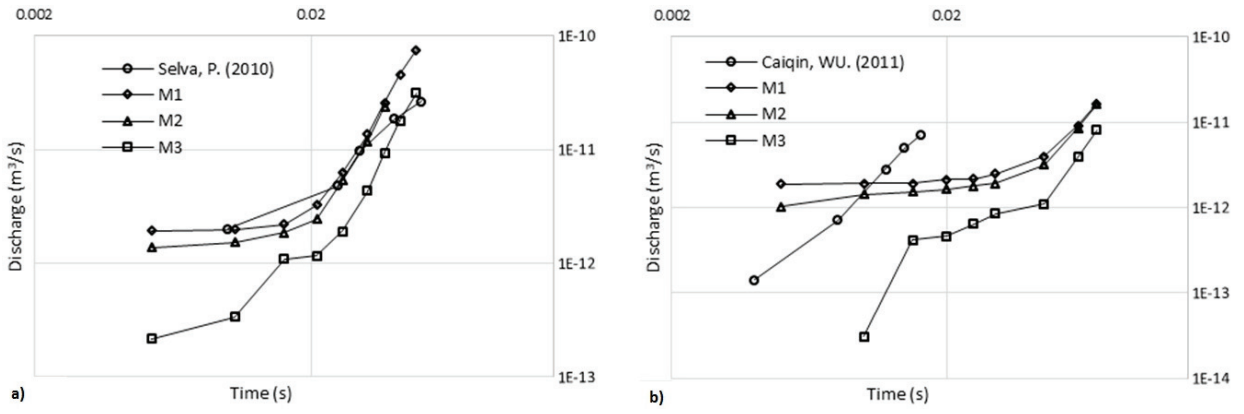
Fig. 8. Discharge in the three meshes from both time steps:
(a) profile $\omega 1$, (b) profile $\omega 2$
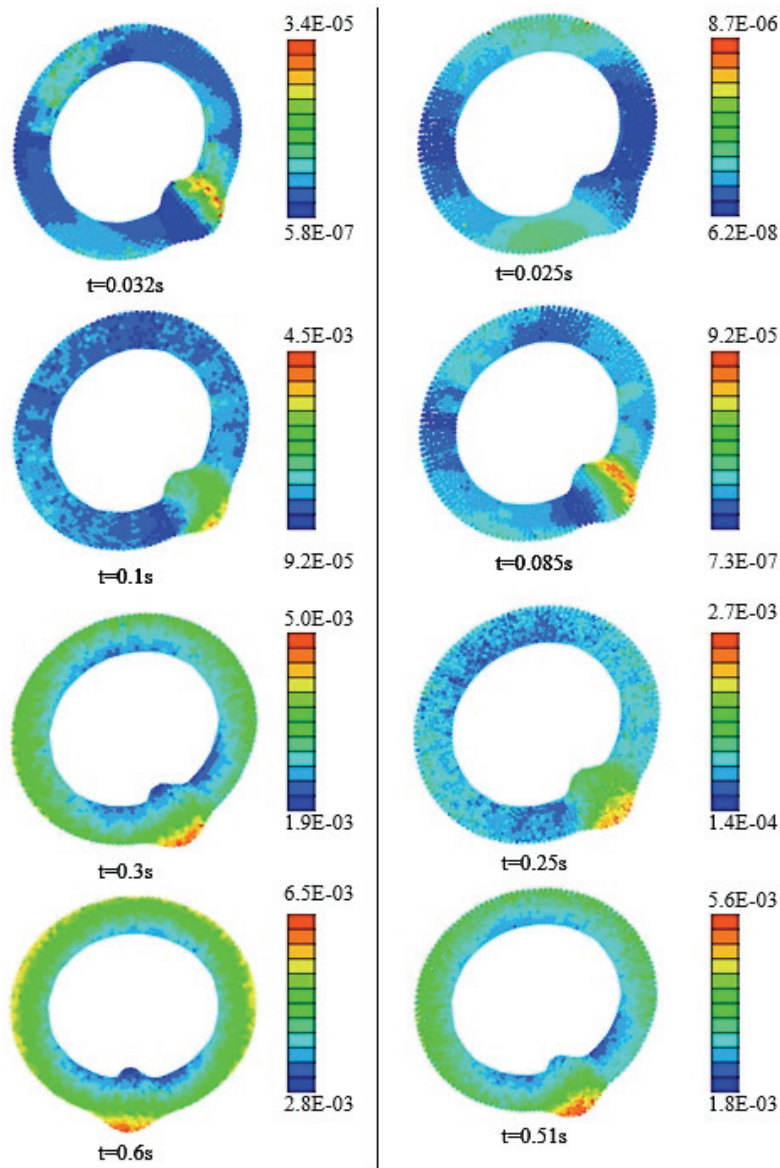


Fig. 9. Fluid velocity (m/s) with M2 along time
from both profile $\omega 1$ (left column) and $\omega 2$ (right column)

$t = 0.005$ s



$t = 0.04$ s



$t = 0.08$ s



$t = 0.11$ s
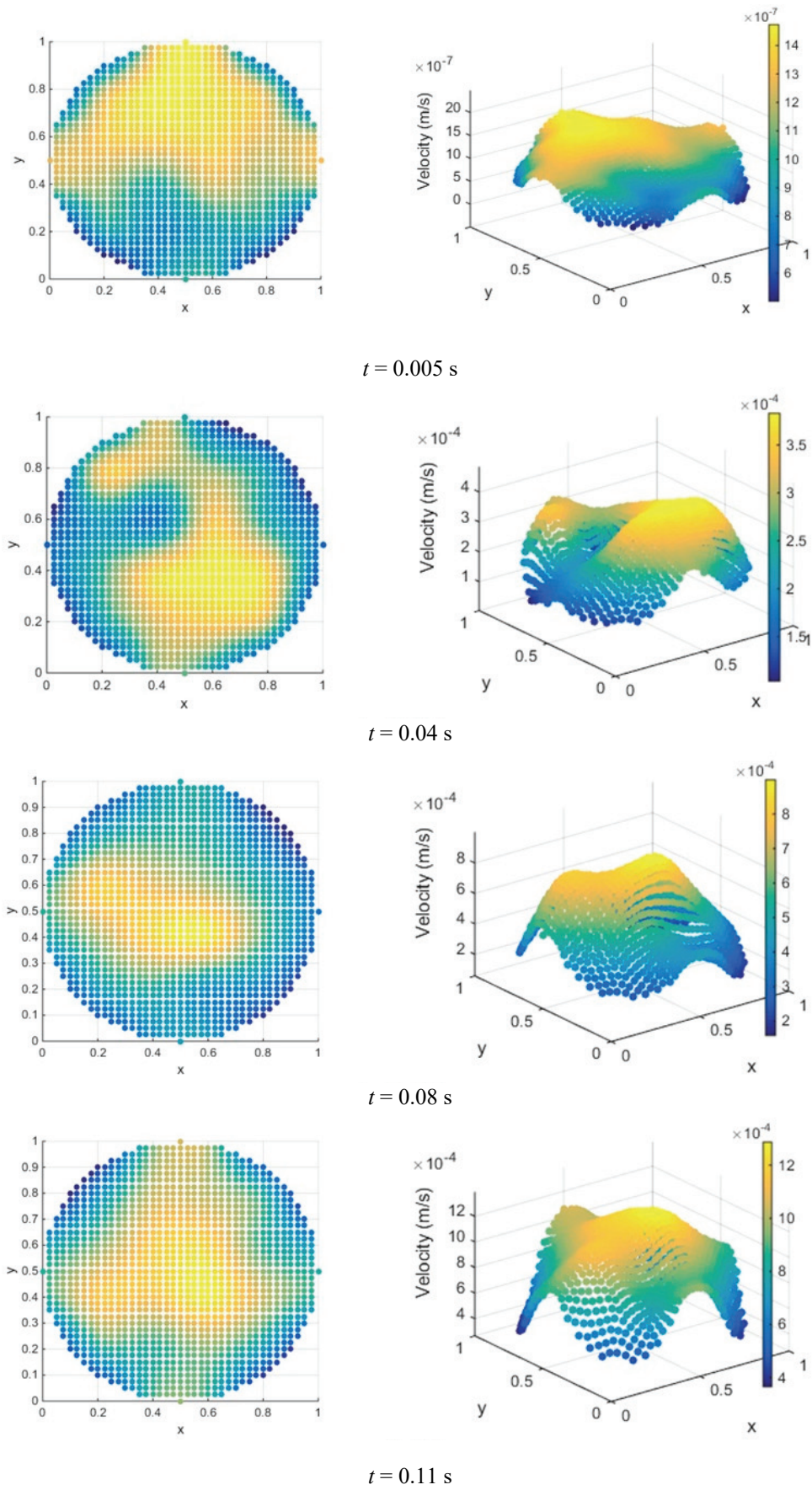
Fig. 10. 3D velocity field along time obtained with profile $\omega 1$
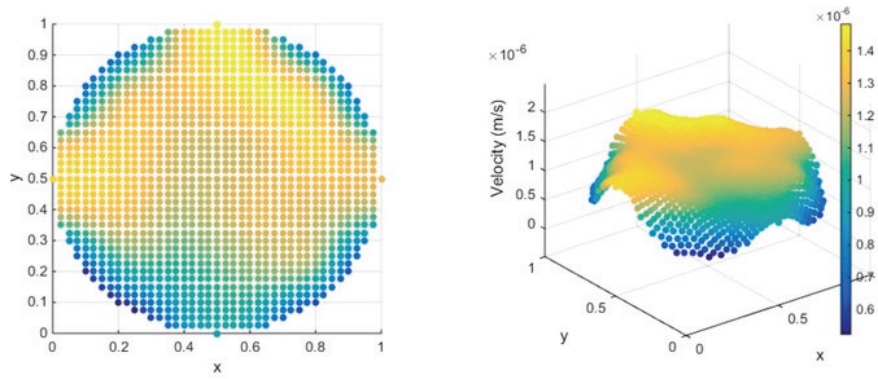
$t$ = 0.005 s
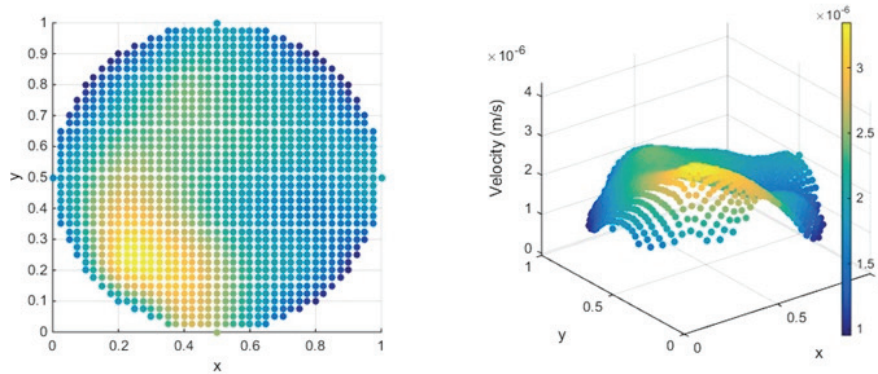


$t$ = 0.045 s
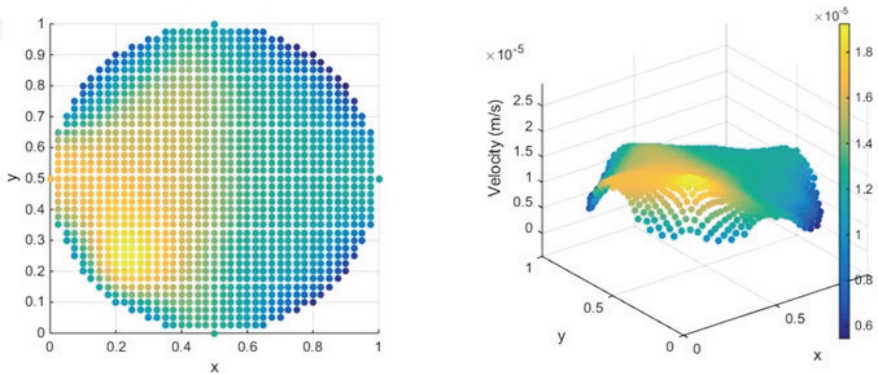


$t$ = 0.075 s
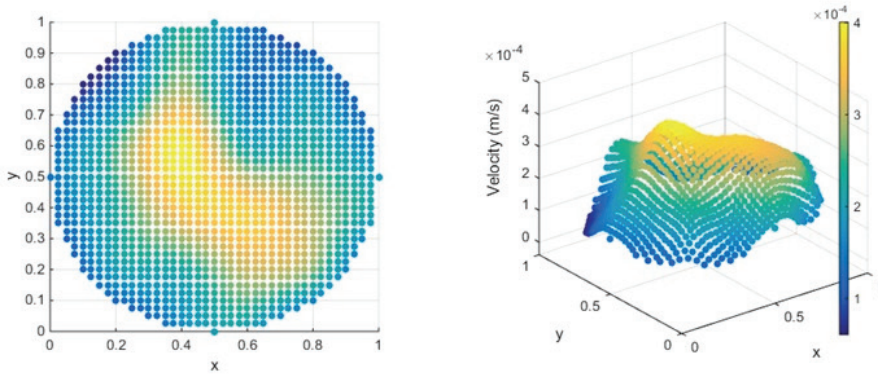


$t$ = 0.105 s

Fig. 11. 3D velocity field along time obtained with profile $\omega$2

# 5. Discussion

The aim of the study presented in this paper is to improve the knowledge of the vestibular system. For this purpose the research is based on the simulation of the rehabilitation process, which need to be more enhanced, and to describe the pathway leading to good rehabilitation results for the patient.

A new model of the vestibular system was developed including a representation of the sections of the SCC, which are the focus of this study. The physiological behavior of the SSC represents the more challenging phase of the complex rehabilitation process.

Thus, it is necessary to construct an accurate model representing such structure of the vestibular system. The three-dimensional model constructed permits a more precise geometric representation of the SSC and allows the trajectory of the fluid inside the canal to be visualized.

The FEM demonstrates once again that this numerical method is a robust technique to obtain fast and reliable results even in the biomechanical field. Additionally, the use of SPH allows a more realistic representation of the fluid behavior. The methodology used permitted us to obtain promising results, considering the biomechanical properties of the components available in the literature.

The results obtained with the three different particle meshes were compared with the works of Selva et al. [22] and Wu Caiqin et al. [30]. The results obtained in this work are very close the solution obtained by Selva et al. [22] and Wu Caiqin et al. [30] when a similar angular velocity is applied to the SCC model, regardless of the particle mesh considered. Additionally, the convergence of the analysis was confirmed.

As Fig. 8 shows, the present analysis produces results closer to Selva et al. solution. The slight differences between the solutions can be explained with the dimensional dissimilarity between the model presented here (a 3D model) and the models of both Selva et al. [22] and Wu Caiqin et al. [30], which are 2D models. The range of results obtained for the discharge are equal in all the simulations (Fig. 8a, b), but in terms of evolution of the fluid flow, our results show more similarity with the work by Selva et al. [22].

Figure 9 shows a lateral section of the model during the simulation. The velocity of the fluid was higher in the cupula, similar to the work of Selva et al. [22], and in the external part of the canal, because of the centrifugal force. When the two velocity profiles are stabilized (after a 0.5 s period) both models present a similar average velocity, as can be seen in Fig. 9.

The velocity 3D distribution is almost fully developed in the last frame of Figs. 10 and 11. The 3D velocity field obtained in both simulations is increasing, as expected. The velocity obtained in the 3D velocity field at instant 0.1 s is three times higher in profile $\omega 1$, the result being in accordance with the velocity applied to the models for that time step, as shown in Fig. 6.

The velocity maps, representing the fluid flow of the entire canal, permitted us to observe the centrifugal force and the consequent higher velocity in the cupula, due to the shape of the SCC. The use of a three dimensional model allowed the visual evidence of a 3D velocity field in a section of the canal at some instants of the simulation. The analysis of the fluid in the section analyzed showed, as expected, that the velocity is higher in the center of the canal.

The encouraging results obtained with this 3D model of just one SCC make it possible to develop and build with confidence the entire model, containing all the main structures of the vestibular system.

The simulation model allows the study of the rehabilitation process in a new perspective without the suffering of the patient. The possibility of modification of all the variables that could influence the symptoms is also an important step in the study of the vestibular diseases.

# 6. Conclusion

This paper presents an alternative reliable numerical approach to study the biomechanical behavior of the vestibular system. In general terms, the results obtained with the 3D numerical model were very similar with the results from literature. However, the 3D velocity distribution which can be obtained in any section of interest is a significant improvement of the present work allowing the velocity field to be analysed point by point, which will allow the otoconia movement to be predicted accurately in future developments of the research. The finite element method combined with SPH for the fluid simulation seems suited to simulate the biomechanical behavior of the SCC.

From the obtained results, it is possible to conclude that the numerical approach presented is convergent and robust, indicating that the increasing particle discretization leads to accurate results.

Additionally, it was found that the SPH approach is able to produce solutions very close to the results

obtained in the work of Selva et al. [22], which uses a Lagrangian–Eulerian approach combined with the FEM formulation.

The development of scientific knowledge of the vestibular system biomechanics is an important step to create new and more precise tools, which can be helpful in the daily routine of people with vestibular disorders. In this field, a better comprehension of the biomechanical behavior of the vestibular system is vital, in order to enhance the computational simulations and the numeric models. This work contributes with an innovating numerical approach to predict the complex movement of the endolymph inside the SSC, which will make it possible to experiment in silico new maneuvers for the rehabilitation therapy.

# Acknowledgements

# References

[1] BONET J., KULASEGARAM S., *Correction and stabilization of smoothed particle hydrodynamics method with applications in metal forming simulations*, International Journal for Numerical Methods in Engineering, 2007, 47, 1189–1214.

[2] BRADSHAW A.P., CURTHOYS I.S., TODD M.J., MAGNUSSEN J.S., TAUBMAN D.S., HALMAGYI G.M., *A mathematical model of human semicircular canal geometry: a new basis for interpreting vestibular physiology*, Journal of the Association for Research in Otolaryngology: JARO, 2010, 11(2), 145–159.

[3] CIARAVELLA G., LASCHI C., DARIO P., *Biomechanical modeling of semicircular canals for fabricating a biomimetic vestibular system*, Conf. Proc. IEEE Eng. Med. Biol. Soc., 2006, 1, 1758–1761.

[4] DAVIS J.L., XUE J., PETERSON E.H., GRANT J.W., *Layer thickness and curvature effects on otoconial membrane deformation in the utricle of the red-ear slider turtle: static and modal analysis*, J. Vestib. Res., 2007, 17(4), 145–162.

[5] DUNCAN R.K., GRANT J.W., *A finite-element model of inner ear hair bundle micromechanics*, Hear Res., 1997, 104(1–2), 15–26.

[6] GAMIZ M., LOPEZ-ESCAMEZ J., *Health-related quality of life in patients over sixty years old with benign paroxysmal positional vertigo*, Gerontology, 2004, 50, 82–86.

[7] GRIESER B., OBRIST D., *Validation of assumptions on the endolymph motion inside the semicircular canals of the inner ear*, 2013.

[8] GENTIL F., GARBE C., PARENTE M., MARTINS P., SANTOS C., ALMEIDA E., JORGE R.N., *The biomechanical effects of stapes replacement by prostheses on the tympano-ossicular chain*, Int. J. Numer Method Biomed. Eng., 2014, 30(12), 1409–1420.

[9] HENSON O.W. et al., Department of Cell and Developmental Biology, University of North Carolina, Chapel Hill and The Center for In Vivo Microscopy, Duke University, Durham, NC, Copyright 2000.

[10] HERDMAN S.J., editor. *Vestibular rehabilitation*, 3rd ed., FA Davis Co., Philadelphia 2007.

[11] HERDMAN S.J., *Vestibular rehabilitation*, Current Opinion in Neurology, 2013, 26(1), 96–101.

[12] HUMPHRISS R.L., BAGULEY D.M., PEERMAN S., MITCHELL T.E., MOFFAT D.A., *Clinical outcomes of vestibular rehabilitation*, Physiotherapy, 2001, 87, 7, 368–373.

[13] JAEGER R., TAKAGI A., HASLWANTER T., *Modeling the relation between head orientations and otolith responses in humans*, Hearing Research, 2002, 173(1–2), 29–42.

[14] KASSEMI M., DESERRANNO D., OAS J.G., *Fluid–structural interactions in the inner ear*, Computers & Structures, 2005, 83(2–3), 181–189.

[15] KONDRACHUK V., *Finite element modeling of the 3D otolith structure*, J. Vestib. Res., 2001, 11(1), 13–32.

[16] LIU G.R., LIU M.B., *Smoothed Particle Hydrodynamics – A Meshfree Particle Method*, World Scientific Publishing Co., Pte., Ltd., 2003,

[17] NEUHAUSER H.K., LEMPERT T., *Vertigo: epidemiologic aspects*, Semin. Neurol., 2009, 29(5), 473–481.

[18] OBRIST D., HEGEMANN S., *Fluid-particle dynamics in canalithiasis*, Journal of the Royal Society, Interface / the Royal Society, 2008, 5(27), 1215–1229.

[19] OBRIST D., HEGEMANN S., KRONENBERG D., HÄUSELMANN O., RÖSGEN T., *In vitro model of a semicircular canal: design and validation of the model and its use for the study of canalithiasis*, J. Biomech., 2010, 43(6), 1208–1214.

[20] RAJGURU S.M., IFEDIBA M.A., RABBITT R.D., *Biomechanics of horizontal canal benign paroxysmal positional vertigo*, J. Vestib. Res., 2005, 15(4), 203–214.

[21] SELVA P., MORLIER J., GOURINAT Y., *Development of a Dynamic Virtual Reality Model of the Inner Ear Sensory System as a Learning and Demonstrating Tool*, Model Simul. Eng., 2009, 2009, 1–10.

[22] SELVA P., MORLIER J., GOURINAT Y., *Toward a three-dimensional finite-element model of the human inner ear angular accelerometers sensors*, Int. J. Comput. Vis Biomech. (IJCV B), 2010.

[23] SHEN S., LIU Y., SUN X. et al., *A biomechanical model of the inner ear: numerical simulation of the caloric test*, Scientific World Journal, 2013, 160205.

[24] SQUIRES T.M., WEIDMAN M.S., HAIN T.C., STONE H.A., *A mathematical model for top-shelf vertigo: the role of sedimenting otoconia in BPPV*, J. Biomech., 2004, 37(8), 1137–1146.

[25] STEINHAUSEN W., *Uber die Beobachtung der Cupula in den Bogengangsampullen des Labyrinths des Lebenden Hechts*, Pflugers Arch. Ges. Physiol,, 1933, 23, 500–512.

[26] VALLI P., BOTTA L., ZUCCA G., VALLI S., BUIZZA A., *Simulation of cupulolithiasis and canalolithiasis by an animal model*, J. Vestib. Res., 2008, 18(2–3), 89–96.

[27] VAN BURSKIRK W.C., WATTS R.G., LIU Y.K., *The Fluid Mechanics of The Semicircular Canals*, J. Fluids Mechanics, 1976, 78(1), 87–98.

[28] VEGA R., ALEXANDROV V., ALEXANDROVA T.B., SOTO E., *Mathematical Model of the Cupula-Endolymph System with Morphological Parameters for the Axolotl (Ambystoma tigrinum) Semicircular Canals*, The Open Medical Informatics Journal, 2008, 2, 138–148.

[29] VON BREVERN M., NEUHAUSER H., *Epidemiological evidence for a link between vertigo and migraine*, Journal of Vestibular Research: Equilibrium & Orientation, 2011, 21(6), 299–304.

[30] WU CAIQIN, HUA C., YANG L., DAI P., ZHANG T., WANG K., *Dynamic analysis of fluid-structure interaction of endolymph and cupula in the lateral semicircular canal of inner ear*, Journal of Hydrodynamics, Ser. B. 2011, 23(6), 777–783.

## 2.3.  Highlights of Contribution II

This publication focused on accurately simulate the vestibular maneuvers based on accelerometer data. In the author's best knowledge, this was the first time accelerometer data and computational model were combined to simulate the vestibular maneuvers.

Therefore, the main contents of this publication include:

I.    Literature review on short vestibular rehabilitation evolution;

II.   Accelerometer data acquisition during a patient neck-flexion-extension, as part of a vestibular rehabilitation maneuver;

III.  Obtaining the exact displacement from the accelerometer data, to be used as an input in the simulation using the SCC model built in the previous paper:

> The main purpose of the present paper was to establish a methodology to simulate the exact movements performed by the audiologist expert during the rehabilitation maneuvers, in order to monitor what actually occurs inside the vestibular labyrinth during the procedure, specifically in the otoconia pathway. Figure 1.4 shows the location where the accelerometer was placed during the maneuvers acquisition (point P) to obtain the movement performed. Furthermore, the point O represents the instantaneous center of rotation, which is in accordance with one of the degrees of freedom of the neck in the Oyz plane, allowing the flexion-extension movement ($\omega$).
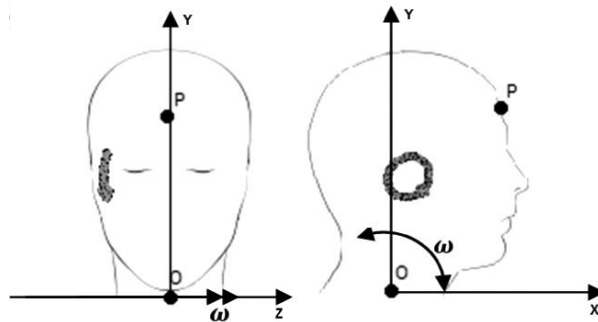


**Figure 1.4** – Scheme of the position of the model in the human body and the accelerometer position (P).

> From the accelerometer data it is possible to obtain the linear acceleration. Thus, using the following kinematic equation (Eq. (1)), it is possible to obtain the displacement field at any given time in a point belonging to the head represented in Figure 1.4.

$$\vec{u}(t) = \begin{Bmatrix} 0 \\ R\sin(\omega(t)) \\ R\cos(\omega(t)) \end{Bmatrix} \tag{1}$$

Where R is the Euclidian distance between O and an interest point in the head, defined as 0.2 m in the present work, since it represents an approximated measured distance from the neck to the inner ear.

IV. Comparison of the velocity obtained in the canal and in the defined section as a consequence of the applied displacement obtained in the previous task, used as input in the simulation;

V. Fluid particle pathway analysis inside the canal along the simulation, starting in different locations:

A representation of the fluid path inside the duct in one of the chosen locations is illustrated as an example, in the Figure 1.5. The point I marks the initial location of this specific fluid particle, while the point II and III seems to be nearly the time instants 1.2s and 3.2s, respectively; which correspond to the moments where a direction change occurs during the flexion-extension movement performed.
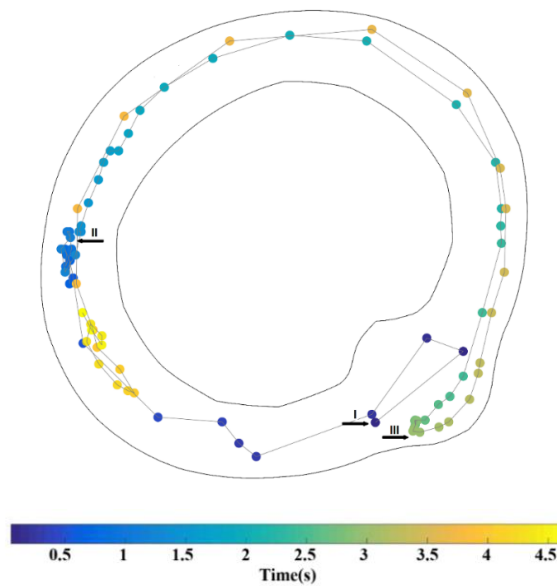


**Figure 1.5** – Particle path inside the canal along the simulation, in seconds.

VI. Conclusions regarding the realistic vestibular rehabilitation procedure simulation achieved from accelerometer data.

The complete document can be found in the next sub-chapter.

## 2.3.1.    Contribution II

# A computational framework to simulate the endolymph flow due to vestibular rehabilitation maneuvers assessed from accelerometer data

Taylor & Francis
Taylor & Francis Group

Check for updates

# A computational framework to simulate the endolymph flow due to vestibular rehabilitation maneuvers assessed from accelerometer data

Carla F. Santos[a] [iD], Jorge Belinha[b] [iD], Fernanda Gentil[c] [iD], Marco Parente[a] [iD], Bruno Areias[a] [iD] and Renato Natal Jorge[a] [iD]

[a]University of Porto, Faculty of Engineering, INEGI, Porto, Portugal; [b]Department of Mechanical Engineering, School of Engineering, Polytechnic of Porto, Portugal; [c]Clínica ORL - Dr. Eurico Almeida, Escola Superior de Saúde, Porto, Portugal

## ABSTRACT

Vertiginous symptoms are one of the most common symptoms in the world, therefore investing in new ways and therapies to avoid the sense of insecurity during the vertigo episodes is of great interest. The classical maneuvers used during vestibular rehabilitation consist in moving the head in specific ways, but it is not fully understood why those steps solve the problem. To better understand this mechanism, a three-dimensional computational model of the semicircular ducts of the inner ear was built using the finite element method, with the simulation of the fluid flow being obtained using particle methods. To simulate the exact movements performed during rehabilitation, data from an accelerometer were used as input for the boundary conditions in the model. It is shown that the developed model responds to the input data as expected, and the results successfully show the fluid flow of the endolymph behaving coherently as a function of accelerometer data. Numerical results at specific time steps are compared with the corresponding head movement, and both particle velocity and position follow the pattern that would be expected, confirming that the model is working as expected. The vestibular model built is an important starting point to simulate the classical maneuvers of the vestibular rehabilitation allowing to understand what happens in the endolymph during the rehabilitation process, which ultimately may be used to improve the maneuvers and the quality of life of patients suffering from vertigo.

## 1. Introduction

Vertigo is a type of dizziness that normally occurs due to a dysfunction in the vestibular system, which is located in the inner ear. The patient has the perception of a spinning motion, a feeling of displacement of the environment relative to the individual or an intensive sensation of rotation inside the head (Taylor and Goodkin 2011). In these situations, it is important to avoid falls. Such symptoms are often associated with nausea and vomiting, and it can cause difficulties in standing or walking if it is related with central lesions (Karatas 2008). Other debilitating symptoms such as blurred vision and hearing loss may also occur (Strupp et al. 2011). Vertigo can be classified as either peripheral or central, depending on the location of the dysfunction in the vestibular pathway, and its most common cause is benign paroxysmal positional vertigo (BPPV) (Karatas 2008), although it can be caused by other factors (Wippold and Turski 2009).

## 1.1. Vestibular system

The vestibular system is the sensory system that provides the leading contribution about movement and sense of balance. As our movements consist of rotations and translations, the vestibular system comprises two connected main components; the three semicircular canals (SCCs), which are placed orthogonally to measure rotational movements, and the utricle and the saccule, which contain the otoliths to measure linear accelerations. Each SCC is comprised of a circular section of continuous fluid, connected with the ampulla and the vestibule (which contains the sensory epithelium).

The SCCs comprise the bony labyrinth, which enclose a membranous labyrinth with the same structure called semicircular ducts (SCD) containing the endolymph; between both labyrinths, another fluid called perilymph is present.

The hair cells of the ampulla rest on a tuft of blood vessels, nerve fibers, and supporting tissue called

---

cupula. The sensory-cells exhibit a constant discharge of neurotransmitters, which are modified by the direction of the cupula deflection, and this output signal has its origin in the velocity of head rotation. Thus, these cells placed in the cupula on the SCD, are known, in the engineering field, as "rate-sensor" (Herdman 2007).

## 1.2. Physical therapy evolution

The original treatment for vestibular disorders was developed in the 1950s and included a set of progressive exercises, called Cawthorne-Cooksey exercises (Cooksey 1946), designed to manage dizziness and improve balance following damage to the inner ear. More recently, techniques have been developed to address specific problems with gaze and postural instability, motion sensitivity, and vertigo in patients with a variety of vestibular disorders such as BPPV, Ménière's disease and others (Zhou and Cox 2004). Some studies (Deveze et al. 2014; Herdman 2013) have analyzed the use of advanced technologies, such as a "balance vest" providing patients with vibrotactile feedback to help them regain balance control. Other methodologies include computerized techniques to help restore steady vision during head movements (gaze stability) and to document improvements in the ability to focus on tasks in the presence of distractions (perceptual and motor inhibition). A device similar to a mirrored "disco ball" has been used to provide optokinetic stimulation for patients with vestibular disorders (Pavlou 2010). Another study (Cox & Jeffery 2010) shows that gaze stability exercises can reduce the risk of falling in older adults with vestibular disorders. Further works (Honaker et al. 2012) show the effectiveness of vestibular rehabilitation on vestibular-visual-cognitive function following blast-induced head trauma sustained by soldiers in war, while in another study (Alsalaheen et al. 2010) an improvement in dizziness, walking and balance was reported after a customized vestibular physical therapy program in children and adults with concussion was developed. All these studies are crucial to document the effectiveness of specific rehabilitation techniques for specific groups of patients with different vestibular dysfunctions.

## 1.3. Vestibular Rehabilitation

Vestibular rehabilitation is becoming an interesting treatment option for a patient with dizziness and balance problems, because such therapy can improve symptoms, functioning, and compliance (Boyer et al. 2008). The vestibular rehabilitation exercises stimulate the brain to use visual clues and proprioceptive alternatives to maintain balance and gait, and there is evidence that it improves nystagmus, control postural dizziness and all other vertigo symptoms, making it the definitive treatment for most patients (Swartz & Longwell 2005). Specific methods include maneuvres to repositioning otoliths, adaptation or substitution exercises that can be vestibular-ocular, vestibular-cervical, or vestibular-spinal, spatial-orientation. Non-specific methods consist generally in rehabilitating overall endurance and strengthening specific muscle groups to sustain posture or balance. The fact that good results can be obtained without drug side effects and that the treatment is both convenient and targeted leads to a gain in confidence by the patient in carrying out its daily activities (Herdman 2013). The first empirical vestibular rehabilitation programs were developed for subjects presenting brain injuries, and later on, the hypothesis of canalithiasis (when the otoconia are loose within the fluid pathways of the inner ear) in the SCD was validated by the success of dislodging maneuvers (Boyer et al. 2008). Physical therapists play a central role in vestibular rehabilitation, not only as care providers but also in helping advance new research in the field. The next wave of vestibular rehabilitation approaches could include virtual reality feedback and training, vestibular implants, and even stem cell techniques (Pavlou 2010; Herdman 2013). With the ultimate goal of improving the quality of life of persons with vestibular disorders, it is important to study the problem from a multi-disciplinary point of view, such that physical therapists, engineers, and physicians all contribute to better understand how the vestibular system works to improve rehabilitation techniques.

## 1.4. Motivation

Although various treatments exist, none can be confidently labeled as the best option because not enough scientific evidence exists, both due to the questionable efficacy of controlled studies and also the difficulty in obtaining data from randomized clinical trials (Boyer et al. 2008). As stated by Herdman (Herdman & Clendaniel 2014), the phenomena that occur during treatment should be correctly identified in order to develop better rehabilitation procedures, and computational models can greatly help study the vestibular system. The present study aims to computationally

model the exact movements performed in that procedure.

## 2. Methods

Studying the movements made during the vestibular maneuvers is the most important step in the rehabilitation process. To this end, such movements were performed by a qualified physical therapist (audiology expert) on a patient and were registered by an accelerometer, which is used to measure acceleration

(and consequently velocity and displacement by integration).

### 2.1. Accelerometer data collection

The accelerometer used in the present work (available in Porto Biomechanics Laboratory) is a BIOPAC© device. The accelerometer was placed in a specific position in the forehead of the patient (point P shown in Figure 1(a)) while the audiologist performed the maneuvers, and data were collected using a sampling rate of 200 Hz. The accelerometer location was chosen
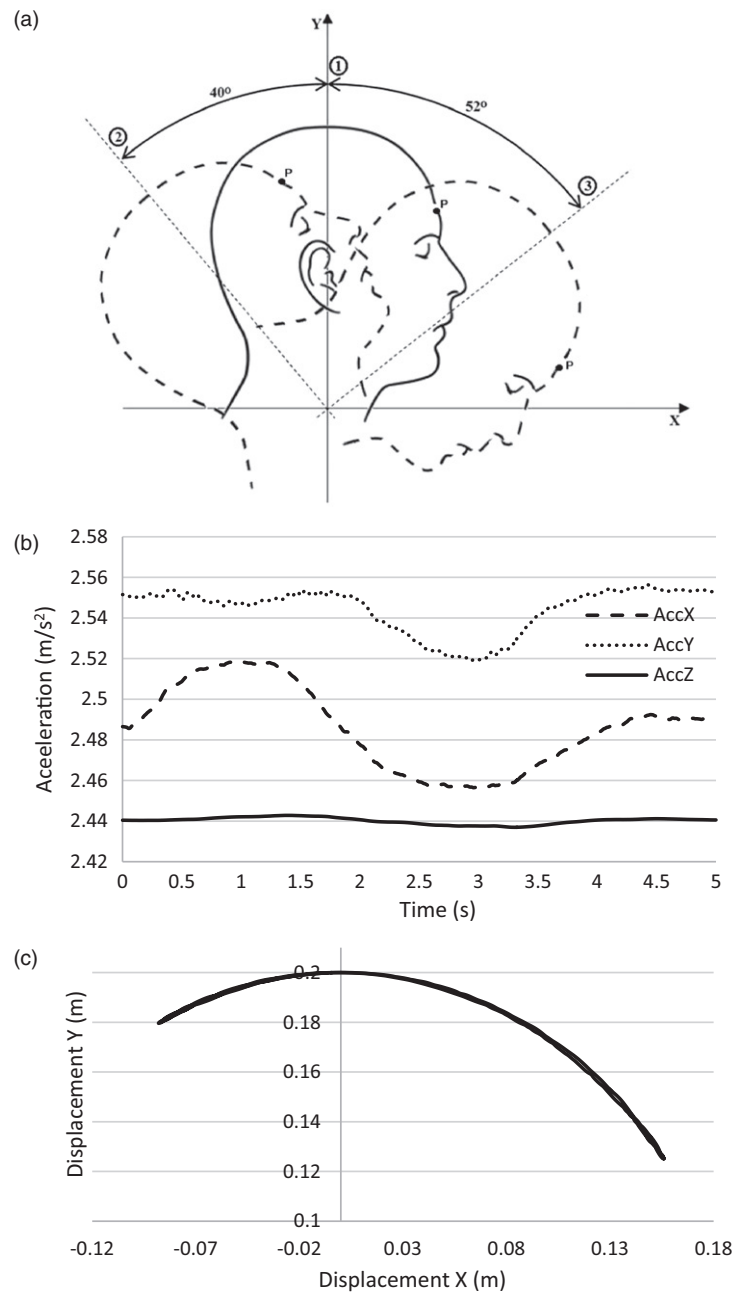


**Figure 1.** (a) Movement performed with the accelerometer, flexion-extension. (b) Acceleration for the movement of the neck. (c) Displacement in the sagittal plane.

35
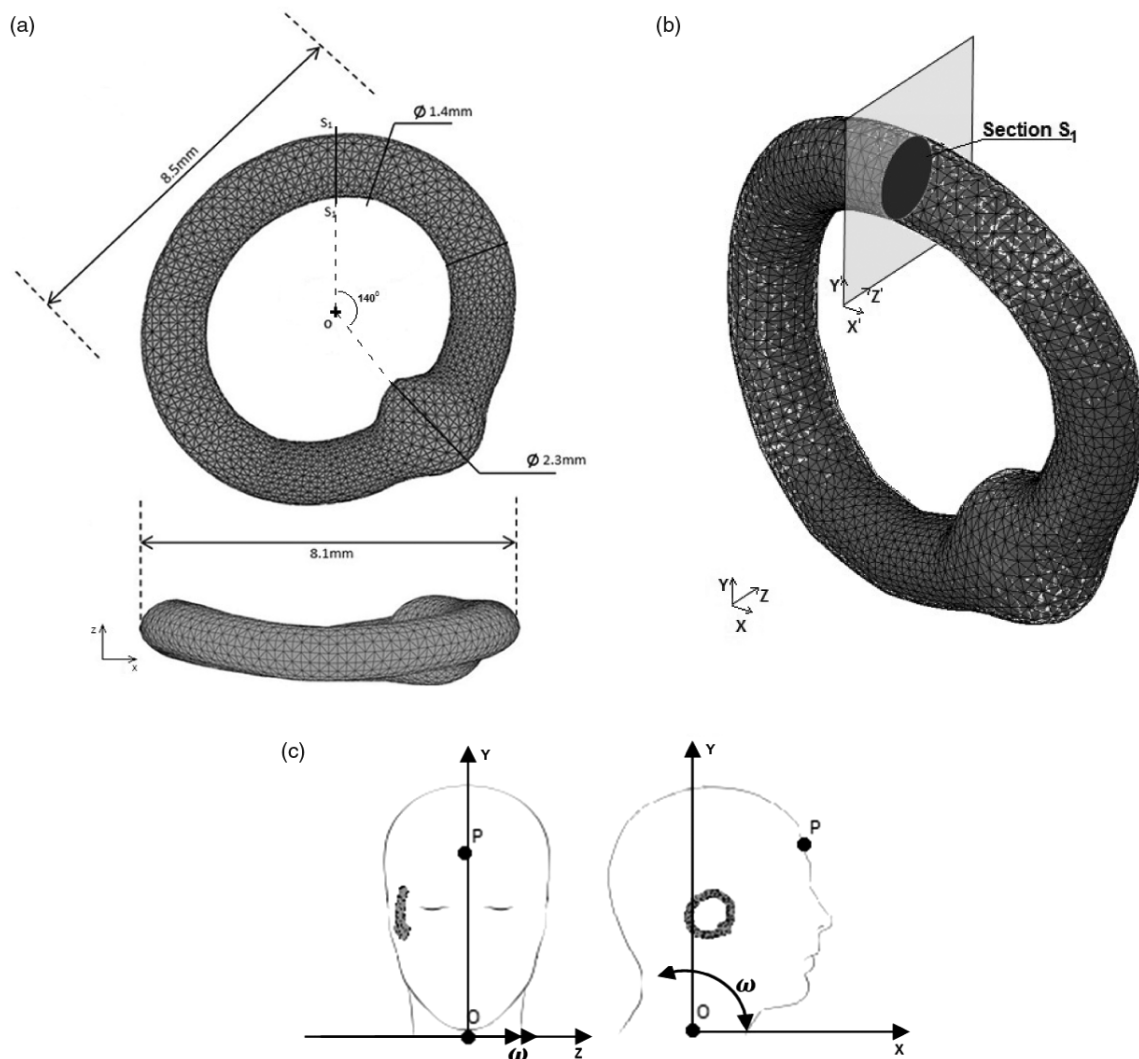
**Figure 2.** Model of one SCC built in finite element method, (a) dimensions of the model, (b) particles inside the canal and Section $S_1$, and (c) Scheme of the position of the model in the human body and the accelerometer.

to capture the movement in the sagittal plane, which is the main plane of the flexion-extension movement.

To test the proposed method, a movement of flexion-extension of the neck was measured, starting by move the head backward and followed by a movement forward until the maximum possible angle (Figure 1(a)). The data obtained from the accelerometer was in volts, which were then converted to g-units and then to the SI units ($m/s^2$) in the three principal axes. Figure 1(b,c) shows the displacement obtained from the accelerometer data (since that the movements performed during the flexion-extension of the neck happened mainly in the sagittal plane as shown in Figure 1(b)). The data were also normalized to zero mean. This movement was the one related with the anterior canal of the vestibular system, which is the most affected by vertigo symptoms in the case of dehiscence syndrome.

Since this is a preliminary study, a simple subset of the full Semont maneuver (Califano et al. 2014) was selected to allows the validation of the proposed numerical approach. The displacement shown in Figure 1(c), obtained by double integration and posterior trigonometric relations due to the angular movement, was applied to the finite element model of the SCD described in the next section in order to simulate the real flexion-extension movement.

## 2.2. Finite element model characterization

The software used to build the model of the vestibular system with finite elements is ABAQUS® (Hibbit & Karlsson 2004). This software is one of the most well-known and robust computational frameworks developed for finite element analysis, mainly used for solid
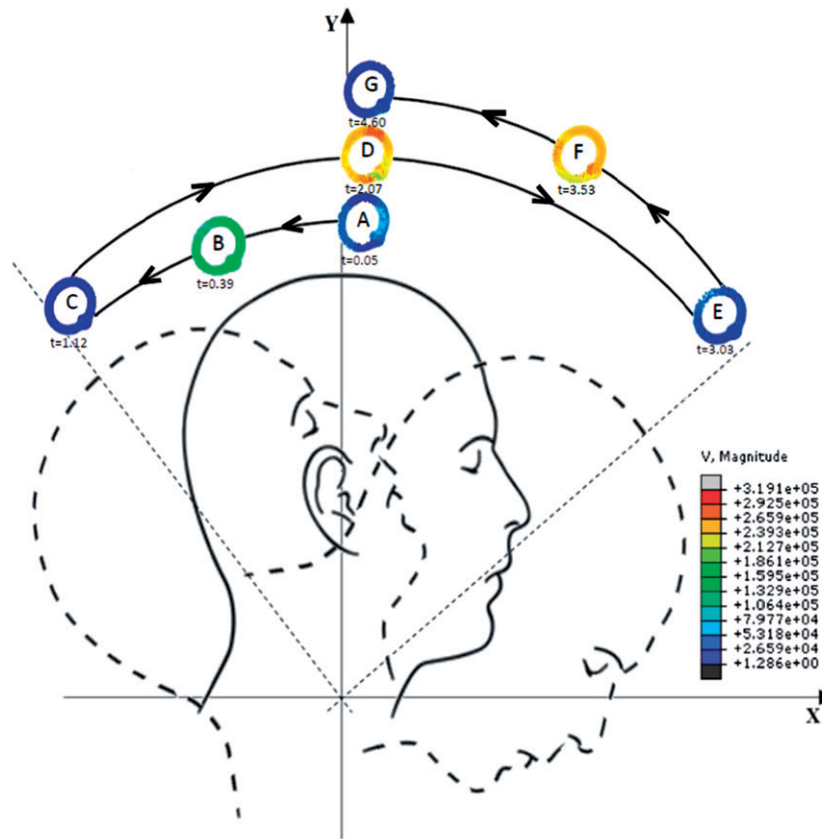
**Figure 3.** Velocity(m/s) of the fluid along the movement.

models but also successfully used to study biological models (Gentil et al. 2011).

The developed 3D model was composed of two main parts: a shell ring that represents one SCD, as shown in Figure 2(a), and inside the ring are particles that represent the endolymph fluid. The model represents the vestibular membrane of the SCD and it is defined as a rigid body, which is a model simplification in order to reduce the computational cost and simulation complexity. The kind of elements used for the shell are linear 4-node shell (S4R). Section $S_1$ (Figure 2(b)) is coincident with the section of the YZ plane where the fluid will be analyzed. The properties of the endolymph used in the model follow those described in the literature (Wu et al. 2011): a density of $1.0 \times 10^{-3}$ kg/m$^3$ and a viscosity of $4.8 \times 10^{-3}$ Pa.s.

The boundary conditions imposed in the model include the general contact between the membrane and the fluid, the gravitational force and finally the angular movement. The model shown in the Figure 2(b) illustrates the SCD filled with fluid with the section analyzed. The dots inside the duct represent the discrete particles related to the endolymph. The simulation of the particles movement is performed considering the

Smoothed Particle Hydrodynamics (SPH) method, which is a meshless method, widely used in bio-fluid simulations (Liu and Liu 2003; Ye et al. 2016). The dimensions of the model were obtained from a CT-scan of the SCC, with more detailed information about that procedure available in a previous work (Santos et al. 2017). An updated survey concerning geometric models and SPH applications to biomechanics (Santos et al. 2017), shows the reduced number of research works simulating this important pathology. In the scheme represented in Figure 2(c), point O represents the instantaneous center of rotation, which is in accordance with one of the degrees of freedom of the neck in the yOz plane, allowing the flexion-extension movement. Therefore, in the represented movement, only rotations around the Oz axis are allowed.

Notice that Figure 2(c) does not represent a real scale canal, as the dimensions are enlarged for easier understanding. As already mentioned, from the accelerometer it is possible to obtain the linear acceleration. Thus, using the following kinematic equation, it is possible to obtain the displacement field at any given time in a point belonging to the head represented in Figure 2(c),

37
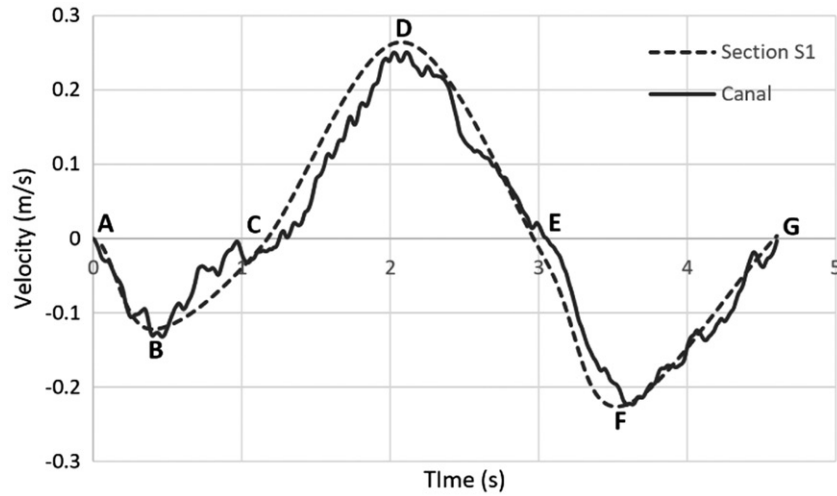
**Figure 4.** Smoothed average x-velocity component in section $S_1$ and the canal.

$$\vec{u}(t) = \begin{cases} 0 \\ R\sin(\omega(t)) \\ R\cos(\omega(t)) \end{cases} \quad (1)$$

Being $R$ the Euclidian distance between O & an interest point in the head. With the displacement field fully defined, in Cartesian coordinates, it is possible to define the velocity,

$$\frac{d\vec{u}(t)}{dt} = \vec{v}(t) = \begin{cases} 0 \\ R\dfrac{d\omega(t)}{dt}\cos(\omega(t)) \\ -R\dfrac{d\omega(t)}{dt}\sin(\omega(t)) \end{cases} \quad (2)$$

and then the acceleration field,

$$\frac{d\vec{v}(t)}{dt} = \vec{a}(t) = \begin{cases} 0 \\ R\dfrac{d^2\omega(t)}{dt^2}\cos(\omega(t)) - R\left(\dfrac{d\omega(t)}{dt}\right)^2\sin(\omega(t)) \\ -R\dfrac{d^2\omega(t)}{dt^2}\sin(\omega(t)) - R\left(\dfrac{d\omega(t)}{dt}\right)^2\cos(\omega(t)) \end{cases}$$
$$(3)$$

Knowing the exact position of point P & point O, it is possible to obtain $R$. In this work, $R = 0.2\,m$ was used, since it represents an approximated measured distance from the neck to the inner ear. Then, matching Equation (3) to the acceleration coming from the accelerometer, it was possible to obtain the instantaneous angular velocity $\omega(t)$. Knowing the approximate location of the vestibular system, point Q, it was possible to determine a new $R = \|\overrightarrow{OQ}\|$, which is inserted in Equation (1) to obtain the displacement field of the vestibular system in Cartesian coordinates.

After the simulation performed the results were obtained & analyzed.

## 3. Results

Simulations were carried out using the parameters defined in the previous section, & the results regarding fluid velocity along the duct are shown in Figure 3, where various frames ranging from A to G cover the totality of the experimentally measured head movement.

The A, D & G frames correspond to location 1 in Figure 1(a) but to different instants of the simulation, while frames C & E correspond to the instants when there is a change in the direction of movement, visible due to the lower velocities, & refer to position 2 & 3 in Figure 1(a) respectively. Finally, frames B, D, & F are the ones with higher velocity, coinciding with the midway moments between each change in direction. After this preliminary analysis, one section of the duct ($S_1$ showed in Figure 2(b)) was analyzed. Figure 4 shows the averaged x-velocity component of the fluid particles in section $S_1$ along the simulation, compared with the x-velocity component of the duct. The letters correspond to the same moments as in Figure 3.

A representation of the fluid path inside the duct is illustrated in Figure 5, which shows five different paths with different initial locations (point I), to simulate the start of the simulation at different quadrants of the duct apart from the locations anterior & posterior to the cupula. Figure 5 shows the real movement of the fluid inside the duct. Thus, the path of five different fluid particles was shown inside the duct. At the beginning of the analysis, five particles (representing distinct finite volumes of fluid, at distinct spatial positions) were selected: particle **a**, **b**, **c**, **d**, & **e**, respectively represented in Figures 5(a–e). The five different locations were selected in relevant positions, such as posterior & anterior to the cupula (particles **a** & **b** respectively), in the opposite position to the cupula (particle **c**) & in the halfway distance between the cupula & particle **c**
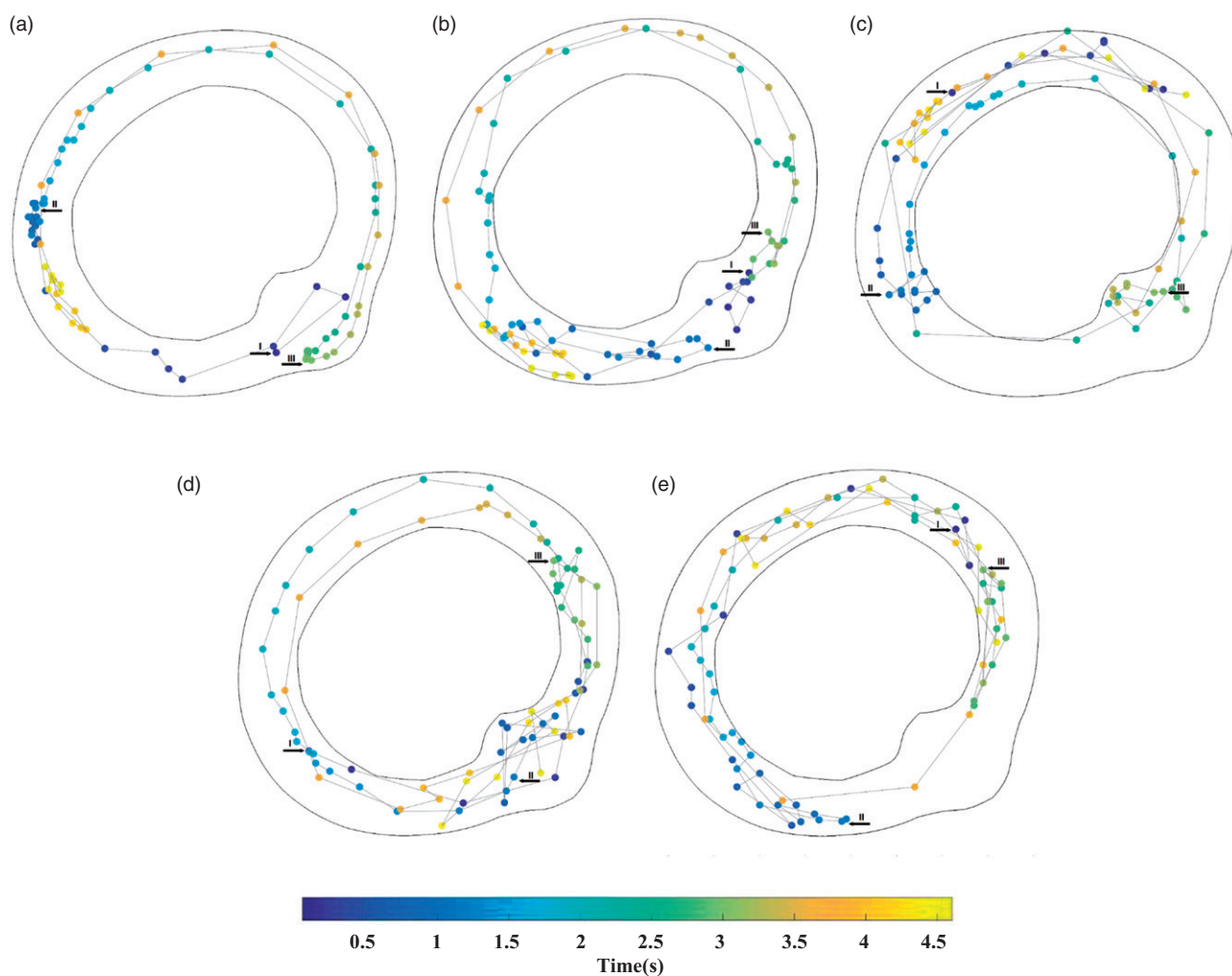
**Figure 5.** Particle path along the simulation, in seconds, starting in five different locations: (a) posterior to the cupula, (b) anterior to the cupula, (c) opposite position to the cupula, (d) halfway distance between the cupula and particle c in left side, and (e) halfway distance between the cupula and particle c in right side.

(particles **d** & **e**, respectively). Such analysis intends to understand the influence of the initial position of the particle in its trajectory.

Therefore, the motion of these particles was tracked. Allowing to capture a global position with respect to time. In the figure, it is possible to see the trajectory of the particle along time. Furthermore, to enhance the comprehension of the trajectory, in Figure 5, a color bar is included indicating the time step of the analysis (in seconds). Thus, the blue color represents the particle at the initial time & the yellow color represents the position of the same particle at the final time.

Notice that the particle alters its movement direction (see point II & point III) at the same instant as the head movement change (frames C & E in Figure 3).

## 4. Discussion

The representation of fluid velocity along the SCD, shown in Figure 3, seems to follow what would be

expected: the beginning & end of the simulation (frames A & G, respectively) present velocities very close to zero, as do the points of the simulation where change of direction occurs (frames C & E). This is expected because near the beginning of the simulation the fluid is still gaining traction (after being completely still at $t = 0$ $s$), while in both changes of direction (frames C & E) the value is naturally low due to the fact that the head is stopped in a specific instant (therefore only the residual fluid velocity from the immediately previous instant affects the distribution of velocities), & the same reason justifies the velocity profile of the end frame G (the head stops moving at that point). The remaining frames (B, D & F) all present considerable velocity values, which is in accordance with the fact that such frames refer to instances where the head is moving in a certain direction, which induces movement in the fluid. Regarding the relative magnitude of the fluid velocity for those frames, frame B presents the lowest values due to it

occurring shortly after the start of the simulation & also that the angle between frames A & C is 40° (Figure 1(a)), while frame D corresponds to a time step specifically in the middle of C to E which spans 92° of movement, thus a higher magnitude of the movement is expected as the fluid has more time to reach a higher velocity. Finally, frame F is in the middle of a 52° movement, which explains why the velocity magnitude is higher than frame B but slightly lower than frame D.

The range of movement obtained in the sagittal plane are in agreement with the average angle for the flexion-extension of the neck found in the literature (Dunleavy and Goldberg 2013). The amplitude of the neck movement is higher in the anterior part of the body like the results shows. The 0.20 m used as reference in Figure 1(c) is the average distance from the neck to the inner ear.

Figure 4, which shows the average fluid velocity across section $S_1$ as a function of simulation time, follows a similar trend: instants C and E, where the velocity is zero, correspondi to the instants around seconds 1 and 3 in Figure 1(b), where the x-component of the acceleration changes its direction. Such change in direction corresponds to the derivative being zero, which confirms the results presented in Figure 4 and the velocity magnitudes in Figure 3. Comparing both curves in Figure 4, both velocities present similar results, indicating the reliable behavior of the model towards the imposed displacement, which is what was expected. The average velocity of all particles in section $S_1$ is also an indicator of result reliability, as higher velocities correspond, as expected, to the longer part of the movement without direction changes, between point 2 and 3 (see Figure 1(a)).

As for Figure 5, it is visible that the starting point of the analysis influences the results, which is expected due to the varying geometry of the duct, which affects the dynamics of the fluid in different ways and is what happens in the real situation due to this model geometry being similar to the geometry of the inner ear. The pathway between point I and II is the shortest, as expected, compared with the one between point II and III. This output, obtained in Figure 5, reveals the possibility to track/analyse any particle fluid or otoconia path inside the SCD during the simulation.

Comparing the results obtained with the chosen particles it is possible to observe that particles **a** and **b** (posterior and anterior to the cupula) are the ones with the best-defined path along the duct. This behavior could be a helpful guide in the common BPPV cases where the otoconia rest near the cupula. Also,

the distance between two color points allows us to conclude if the analyzed particle is slower or faster in each specific part. Particles **c** and **e**, which start their path in the superior part of the duct, appear to show slower movements, as the points looks closer between each other. All the selected particles showed a final position (the yellowest spot) at a similar distance from the initial position in the five paths.

These results show the effectiveness of the model and prove that it is possible to infer about the inner movement of the endolymph and, consequently, the movement of otoconia. Nevertheless, the authors would like to clarify that the model has some limitations that should be considered, as the structure of the ducts and the canals. In future works, the model of the vestibular system should be enhanced to include the vestibules and the crus commune in order to obtain simulation outcomes closer to the anatomical system. Additionally, despite the limitations, the current model showed similar results with other authors (Santos et al. 2017).

Since all the maneuvers performed in the vestibular rehabilitation are based in angular movements, it appears that the used method, based in trigonometric relationships, is a valid numerical technique to deduce the displacement of the head, allowing for successful simulations based in the accelerometer data.

## 5. Conclusion

The main aim of this work is to improve the knowledge on the vestibular rehabilitation process. Since the vestibular rehabilitation performed nowadays consist in a set of movements which lack accuracy and consistent reproducibility, the method presented in this paper intends to be a step to improve this procedure. An overall analysis of the results shows that such main aim was achieved. Data obtained using an accelerometer from a patient treated by a qualified physical therapist was combined with a finite element model to simulate the flexion-extension movement of the SCC, and the results allow us to validate this method as a starting point of the rehabilitation maneuvers simulation, as the fluid velocity distribution as a function of analysis time is coherent and follows the head movement. This work is an important first step both because it validates the model and also because it is focused on the less studied canal associated with BPPV, which opens the way for further studies into the diseases occurring in this canal, as emphasized by Herdman (Herdman 2013).

The study of vestibular rehabilitation is also very important as it is a treatment for vestibular disorders which does not administers drugs (Rosengren et al. 2010), making it a natural alternative free of pharmaceuticals. As for future work, this model should be tested using the same method under different conditions – such as the three more common maneuvers used in the vestibular rehabilitation.

In conclusion, the use of computational simulation is an exceptional opportunity to create realistic simulations in biomedicine, as proved in this research work where the movements involved in vestibular rehabilitation was numerically reproduced.

## Acknowledgments

## Disclosure statement

No potential conflict of interest was reported by the authors.

## ORCID

Carla F. Santos (iD) https://orcid.org/0000-0002-0304-1356
Jorge Belinha (iD) http://orcid.org/0000-0002-0539-7057
Fernanda Gentil (iD) https://orcid.org/0000-0002-6521-3475
Marco Parente (iD) http://orcid.org/0000-0002-3326-6345
Bruno Areias (iD) https://orcid.org/0000-0001-9583-3571
Renato Natal Jorge (iD) http://orcid.org/0000-0002-7281-579X

## References

Alsalaheen BA, Mucha A, Morris LO, Whitney SL, Furman JM, Camiolo-Reddy CE, Collins MW, Lovell MR, Sparto PJ. 2010. Vestibular rehabilitation for dizziness and balance disorders after concussion. J Neurol Phys Ther. 34(2):87–93.

Boyer FC, Percebois-Macadré L, Regrain E, Lévêque M, Taïar R, Seidermann L, Belassian G, Chays A. 2008. Vestibular rehabilitation therapy. Neurophysiol Clin. 38(6):479–487.

Califano L, Salafia F, Mazzone S, Melillo MG, Califano M. 2014. Anterior canal BPPV and apogeotropic posterior canal BPPV: two rare forms of vertical canalolithiasis. Acta Otorhinolaryngol Ital. 34(3):189–197.

Cooksey FS. 1946. Rehabilitation in Vestibular Injuries. Proc R Soc Med. 39(5):273–278.

Cox PG and Jeffery N. 2010. Semicircular canals and agility: the influence of size and shape measures. J Anat. 216(1):37–47.

Deveze A, Bernard-Demanze L, Xavier F, Lavieille J-P, Elziere M. 2014. Vestibular compensation and vestibular rehabilitation. Current concepts and new trends. Neurophysiol Clin. 44(1):49–57.

Dunleavy K and Goldberg A. 2013. Comparison of cervical range of motion in two seated postural conditions in adults 50 or older with cervical pain. J Man Manip Ther. 21(1):33–39.

Gentil F, Parente M, Martins P, Garbe C, Jorge RN, Ferreira A, Tavares JM. 2011. The influence of the mechanical behaviour of the middle ear ligaments: a finite element analysis. Proc Inst Mech Eng H. 225(1):68–76.

Herdman S. 2007. Vestibular rehabilitation. F.A. Davis, Philadelphia.

Herdman SJ, Clendaniel R. 2014. Vestibular Rehabilitation (Contemporary Perspectives in Rehabilitation) 4th Edition. F.A. Davis, Philadelphia.

Herdman SJ. 2013. Vestibular rehabilitation. Curr Opin Neurol. 26(1):96–101.

Hibbit SPD, Karlsson B. 2004. Software License Agreement for Academic Institutes, ABAQUS: Theory Manual", Providence, USA.

Honaker JA, Tomasek R, Bean K, Logan B. 2012. Impact of visual disorders on vestibular and balance rehabilitation therapy outcomes in soldiers with blast injury. Int Tinnitus J. 17(2):124–133.

Karatas M. 2008. Central vertigo and dizziness. Neurologist. 14(6):355–364.

Liu GR, Liu MB. 2003. Smoothed Particle Hydrodynamics. WORLD SCIENTIFIC, Singapore.

Pavlou M. 2010. The use of optokinetic stimulation in vestibular rehabilitation. J Neurol Phys Ther. 34(2):105–110.

Rosengren SM, Welgampola MS, Colebatch JG. 2010. Vestibular evoked myogenic potentials: past, present and future. Clin Neurophysiol. 121(5):636–651.

Santos CF, Belinha J, Gentil F, Parente M, Jorge RN. 2017. An alternative 3D numerical method to study the biomechanical behaviour of the human inner ear semicircular canal. Acta Bioeng Biomech. 19(1):3–15.

Strupp M, Thurtell MJ, Shaikh AG, Brandt T, Zee DS, Leigh RJ. 2011. Pharmacotherapy of vestibular and ocular motor disorders, including nystagmus. J Neurol. 258(7):1207–1222.

Swartz R, Longwell P. 2005. Treatment of vertigo. Am Fam Physician. 71(6):1115–1122.

Taylor J, Goodkin HP. 2011. Dizziness and vertigo in the adolescent. Otolaryngol. Clin North Am. 44(2):309–321.

Wippold FJ, Turski PA. 2009. Vertigo and Hearing Loss AJNR. Am J Neuroradiol. 30(8):1623–1625.

Wu C, Hua C, Yang L, Dai P, Zhang T, Wang K. 2011. Dynamic analysis of fluid-structure interaction of endolymph and cupula in the lateral semicircular canal of inner ear. J Hydrodyn Ser B, 23(6):777–783.

Ye T, Phan-Thien N, Lim CT. 2016. Particle-based simulations of red blood cells-A review. J Biomech. 49(11):2255–2266.

Zhou G and Cox LC. 2004. Vestibular evoked myogenic potentials: history and overview. Am J Audiol. 13(2):135–143.

## 2.4.    Highlights of Contribution III

This contribution focused on the experimental validation of the SCC model and, for the first time, on the numerical simulation of the vestibular system using human shaped cupulas.

Therefore, the main contents of this publication include:

I.    A brief review of the vestibular system physiology, with a focus on the BPPV condition;

II.    Numerical description on the discrete geometrical models built as an enhanced process from the previous models:

> The methodology approach regarding the numerical models followed the previous manuscripts, applying the FEM and SPH as simulation methods. Therefore, the enhanced model includes the SCC with the cupula and otoconia as integral structures; which naturally evolved to the total vestibular system model with the three SCCs and the corresponding structures, as it can be observed in Figure 1.6. The properties used in this model were the same used in the preceding models.

a)                                                                b)

6.63 mm

x
y

z
x
y
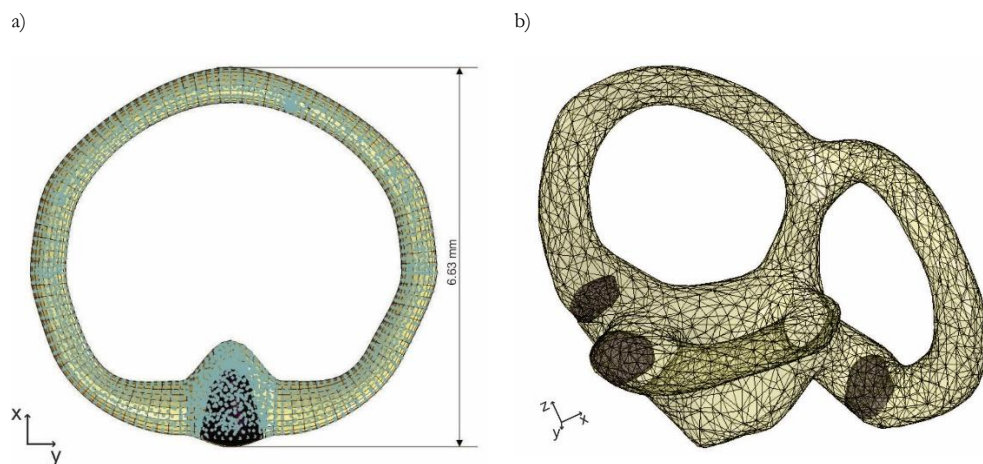
**Figure 1.6** – Numerical model of the vestibular system with and without fluid: a) one SCC, b) total model.

III.    Characterization of the experimental setup of the manufactured SCC silicone model used to validate the numerical results;

IV.    Validation of the SCC numerical model, including the cupula and otoconia structures interaction:

> The angle between the otoconia and the cupula, during the otoconia's movement until it reached the cupula, was compared between the experimental and numerical models. Three simulations were performed, with the otoconia's initial position set in three distinct locations inside the canal. Figure

1.7 shows the results obtained for one of those simulated situations, corresponding to the one where the initial otoconia position is closer to the cupula.
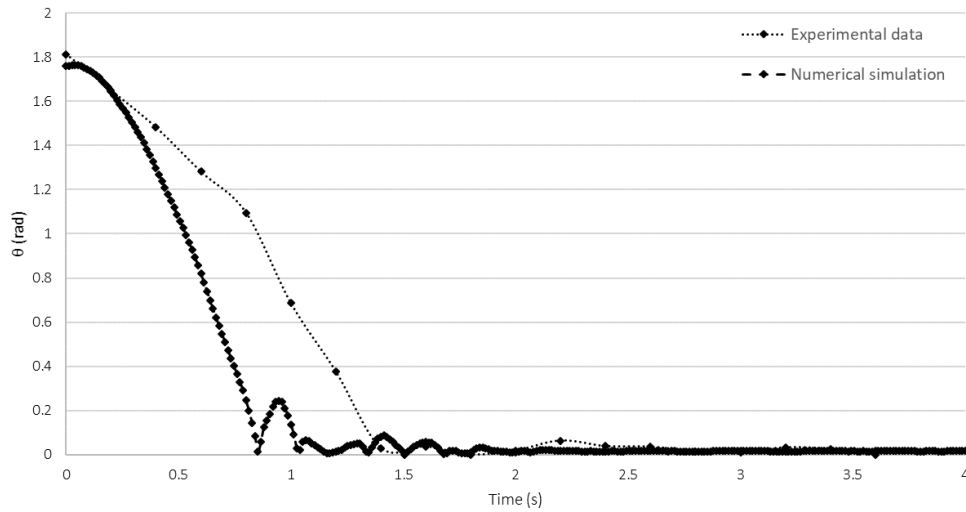


**Figure 1.7** – Angle ($\theta$) between the otoconia and the cupula as a function of time.

V. Analysis of the cupula displacement behavior in the model with one SCC, along time, imposing the same smooth step and testing three different situations: without otoconia, one otoconia and two otoconia;

VI. Evaluation and discussion of the results obtained with the simulation of the full model of the vestibular system, after imposing Epley vestibular maneuver segments of a realistic condition of BPPV, using an otoconia;

VII. Discussion of the main validation and simulation challenges, and conclusion on the achievements to the vestibular research field:

Despite the excessive computational time required to reach the simulation results, they allowed to increase the comprehension about the inner ear biomechanical behavior and increase the knowledge in this research field, which will help the worldwide population that daily experience incapacitating dizziness symptoms and suffer from vestibular disorders.

The complete document can be found in the next sub-chapter.

## 2.4.1.   Contribution III

## Simulation of Epley Maneuver using an Enhanced Vestibular System Computational Model developed using a Realistic Anatomical Human Shape

*Submitted to an International Journal*

# Simulation of Epley Maneuver using an Enhanced Vestibular System Computational Model developed using a Realistic Anatomical Human Shape

Carla F. Santos [a,d], J. Belinha [a,b] , Fernanda Gentil [c], Marco Parente [a,d,] M.M.F. Machado and Renato Natal Jorge [a,d]

a INEGI, Institute of Mechanical Engineering and Industrial Management, Rua Dr. Roberto Frias, Porto, Portugal.
b School of Engineering, Polytechnic of Porto, (ISEP), Porto, Portugal
c Clínica ORL-Dr. Eurico Almeida, Widex, Escola Superior de Saúde – I.P.Porto, Porto,Portugal
d FEUP, Faculty of Engineering of the University of Porto, Rua Dr. Roberto Frias, Porto, Portugal.

**Abstract**

The main role of the vestibular system, which is part of the inner ear, is maintaining the sense of balance and spatial orientation. The consequent disorders commonly lead to dizziness, which daily affects the insecurity of many people worldwide. Increase the knowledge in order to improve or avoid the vestibular therapy methodologies is the main goal of the present work.

Developing a complete and functional numerical model of such a sensory structure, such is the human vestibular system, includes several steps, being the model validation one of the most significant in the all process. The geometrical model was created combining the finite element method with a particle meshless method, the Smoothed-Particle Hydrodynamics method to simulate the endolymph.

First, in order to validate the computational approach, a physical semicircular canal silicone model was built and submitted to a known movement law. A particle was introduced inside the semicircular canal model and its position along time was documented. Afterwards, a computational simulation was performed, allowing to compare the numerical solution with the experimental data.

Next, the complete vestibular system was simulated, including the three semicircular canals with the respective cupulas. Thus, a Benign Paroxysmal Positional Vertigo condition with an otoconia lost in the posterior canal was simulated applying the Epley maneuver, including a pioneering cupula shape. The numerical simulation showed that the movement imposed by Epley maneuver replaces the otoconia back to the vestibule in an unexpected way, explaining the high success rates of the vestibular rehabilitation repositioning maneuvers.

# 1.Introduction

Human postural control demands an active contribution from several body sensors, such as the visual, vestibular and proprioceptive. Postural imbalance is often the main consequence of vestibular dysfunctions [1]. The role of the vestibular system is maintaining the body balance by continuously providing accurate information, related to the position of the head and body, to the brain. The main structure of this system is the group of the three semicircular canals (SCCs), placed orthogonally and linked to each other [2]. Each ear has its own canals; therefore, each individual has six semicircular canals, which work in a coordinated manner to maintain balance. The structure of the canal comprises a membranous labyrinth, embraced by a bony labyrinth with the same shape. The membranous labyrinth is filled with a fluid called endolymph. Moreover, a fluid called perilymph takes place between both labyrinths [3]. The complex and detailed structure of the vestibular system is not completed without mentioning the cupula and the macula. These structures contain the sensory hair cells, responsible for sending signals to the brain, signaling the physical movement. The sensory cells exhibit a constant discharge of neurotransmitters that are modified by the direction of the cupula deflection [4] during angular acceleration. The macula, placed in the saccule and the utricle, which are the adjacent structures of the semicircular canals, is a membranous structure composed by a gel layer containing calcium carbonate crystals, known as otoconia. The mass of the otolithic membrane allows the macula to be sensitive to gravity and linear acceleration.

There are several reasons that could lead to a mismatch of information between the systems in control of the balance function. When it occurs, all the process fail, leading to equilibrium loss [5], [6]. Benign Paroxysmal Positional Vertigo (BPPV) is the most common cause of vertigo, and it is described as a brief, intense sensation of spinning that occurs when there are changes in the head orientation with respect to gravity [7]. BPPV occurs when the otoconia remains in the SCC, which are normally located in the macula of the otolith organs, as explained before. If they dislodge from the utricle and become loose in the SCC, it will induce a false spinning sensation when no head rotational motion is actually occurring, generated by the distinct information sent to the brain by the two different systems, visual and vestibular [7], [8].

Moreover, one of the main consequences of any BPPV episode is the risk of falls, which is an important factor when considering the ageing population worldwide. The World Health Organization (WHO) states that falls are the second leading cause of accidental or unintentional deaths worldwide. Thus, WHO proposes and prioritizes the implementation of prevention strategies and fall-related research [9]. It is therefore of high interest to develop improved solutions that contribute to prevent these kinds of vestibular related complications.

The main effective therapy applied in the reported condition is vestibular rehabilitation, comprised by particle repositioning maneuvers and habituation therapy. Nevertheless, such procedures have some drawbacks, mainly considering their empirical nature, premise endorsed by Herdman whom encourage new research on the subject [10]. Moreover, it requires an active and regular home routine exercises to prevent new episodes [11], which is hard to successfully achieve without help, taking into account that the most affected group is the elderly population. The proposal of this work is to develop and validate a finite element model of a semicircular duct, to simulate the real otoconia behavior during vestibular rehabilitation. In order to improve the process, the subsequent step include the otoconia pathway simulation in a complete computational vestibular system model. Furthermore, the groundbreaking factor in this present research is the pioneer shape of the cupula (and corresponding discrete virtual model) used in the computational analysis, modeled based in histological data, which will be detailed in the next section.

# 2.Methods

Advanced discretized techniques, such as the finite element method (FEM) and meshless methods, are widely used to simulate and study several biological effects in computational biomechanics [12]. Such advanced discretization techniques have shown that they are useful and reliable tools to perform biomechanical simulations [13], [14], mainly in the medical field where it is challenging and hard to obtain anatomical and physiological results. The validation process of a computational model is an essential step to add solid scientific value to the results obtained. The present work proposes an experimental validation of the SCC biomechanical model to validate the proposed numerical approach, which was also addressed in previous publications [15] .

### 2.1. 3D Discrete model

The 3D SCC numerical model was built using the commercial software ABAQUS® [16]. The analysis combined the FEM with a particle meshless method – the smoothed particle hydrodynamics (SPH) - to simulate the endolymph. SPH is a computational technique widely used for fluid flow simulation due its efficiency [17]. One advantage of this method is the adaptability of the particles to many fields and subjects [17], [18], such as astrophysical studies [17]. Regarding the biological fluids field, it has already been used by various authors with reliable simulation results [15], [17], [19]. Therefore, it was used in the present work to simulate the endolymph, represented in Figure 1 by the blue particles.

Regarding FEM, the method was applied to the remaining structures of the model: membranous duct, cupula and otoconia. The membranous duct was modeled using a shell ring with an ampullar part, and it was defined as a rigid body. This model simplification was sustained by the rigid bony labyrinth surrounding the vestibular system. It allowed to reduce the computational cost and simulation complexity maintaining the essential interactions inside the duct (the perilymph effect was disregard). The cupula was placed in the ampullar part of the membranous duct, as shown in Figure 1. The otoconia is the small structure shown in the superior part of the canal, used to simulate a BPPV episode, Figure 1a). The number and type of elements used in each structure of the one SCC model are presented in Table 1.
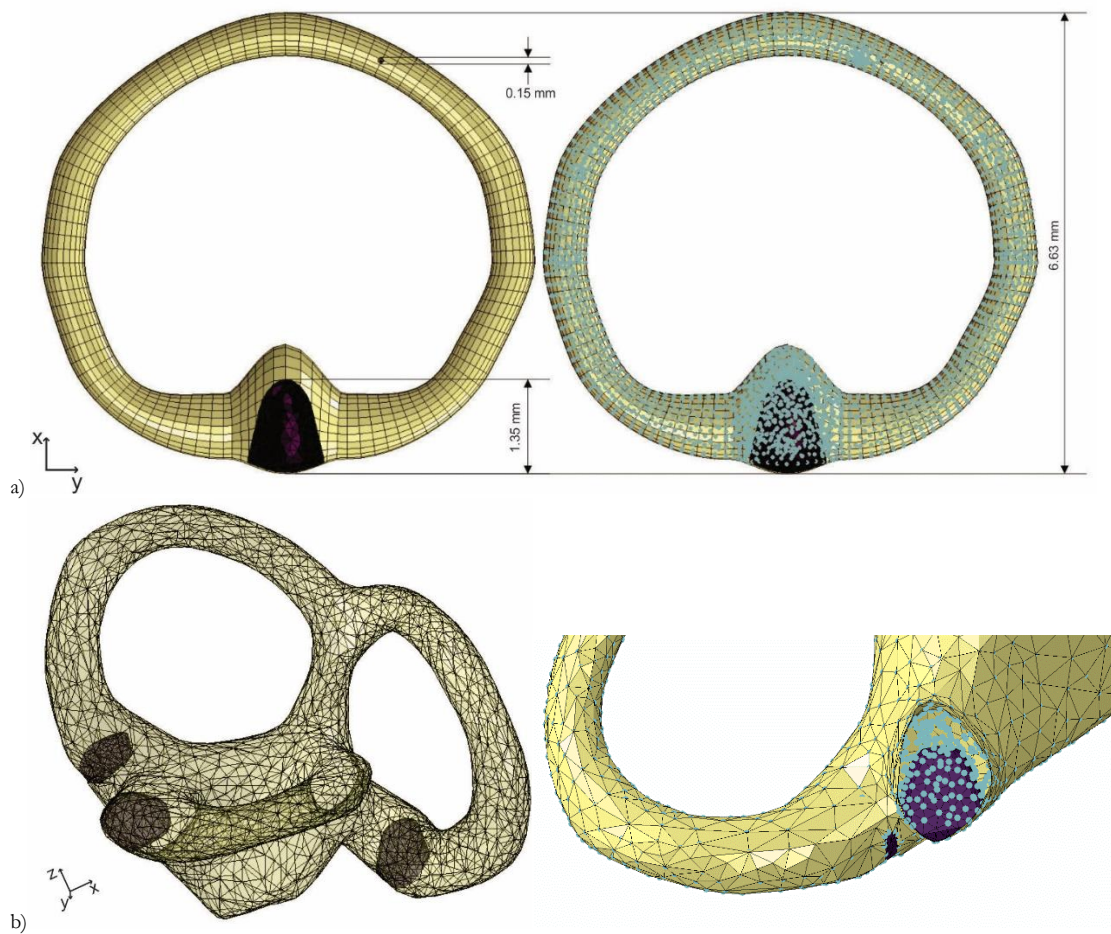


**Figure 1** – Vestibular system model with and without fluid, a) one SCC, b) total model.

Concerning the dimensions of the model, they were obtained from the literature [20], [21] ; the dimensions of the different parts of the canal were obtained by proportionally ratios. Since the human otoconia is known to range in size from 3 to 30 μm [22], and exhibits an irregular shape [23], it was modeled with 0.1 mm diameter and with an asymmetrical and sparse mesh.

The properties used in the one SCC model (Figure 1a)) follow those described in the literature for the structures of the vestibular system, and are presented in Table 1 [24], [25].

**Table 1** – Material properties and elements used in the model [24], [25].

| | Young's Modulus (MPa) | Poisson's ratio | Density (ton/mm³) | Viscosity (MPa.s) | Elements (Number / Type) |
|---|---|---|---|---|---|
| Endolymph | - | - | $1 \times 10^{-9}$ | $8.52 \times 10^{-10}$ | 4450 / PC3D |
| Membrane | 13700 | 0.49 | $1.85 \times 10^{-8}$ | - | 2496 / S4R |
| Cupula | $5 \times 10^{-6}$ | 0.48 | $1 \times 10^{-9}$ | - | 1461 / C3D4 |
| Otoconia | 6.6 | 0.45 | $3 \times 10^{-9}$ | - | 14 / C3D4 |

The boundary conditions imposed in the model include the general contact between all the simulated components, the gravitational force and the angular velocity imposed in the canal, which was obtained from the experimental procedure described in Section 2.3. After the model validation with the one SCC model, the same properties and boundary conditions were adapted to perform the simulations with the global vestibular system model shown in Figure 1b). The Epley maneuver in a BPPV condition was simulated with the global model.

## 2.2. Cupular Structure

Since 1933, when Steinhausen described the dynamics of the cupula-endolymph relation as a highly damped torsion pendulum [26], that several modelling configurations have been developed for the cupular structure and corresponding interactions. Additional discussions by some authors inquire, for example, about the permeability of the cupula [27]. However, the most common computational models of the cupula base their geometry in animal anatomical experiments, such as fishes or birds [28]. It is possible to observe in those works that the cupula reaches the apex of the ampullar part of the canal. Nevertheless, several histological works have shown that the human cupula does not interact with the apex of the ampulla [29], as shown in Figure 2b).
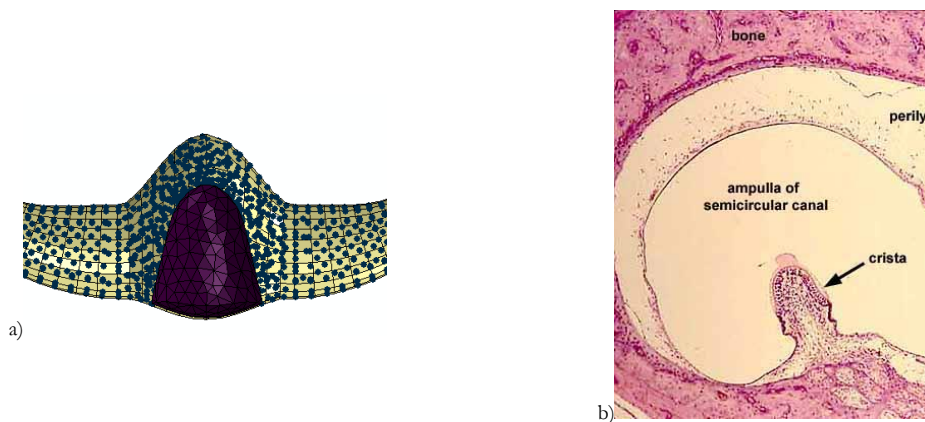


**Figure 2** –Cupula; a) FEM model, b) histological picture.

Instead of the previously mentioned research works, which models the cupula as a compact obstacle to otoconia migration based on animal morphology, the present work proposes a modelling of the cupula that mimics a human cupula structure (Figure 2a). The authors believe that a cupula with a higher flexibility could influence the endolymph flow and consequently the otoconia movement.

## 2.3. Experimental model

Regarding the experimental model, a silicone physical structure was manufactured using the computational model geometry of the one SCC described in Section 2.1, Figure 3a). Silicone experimental models have been developed, in several fields, to evaluate biological structures [30]. In the present work, a platinum-based silicone rubber (Ecoflex 0050) with a hardness of 50 shore was used to build the SCC model shown in Figure 3 b), where l=18.5 cm and h=6.2 cm.
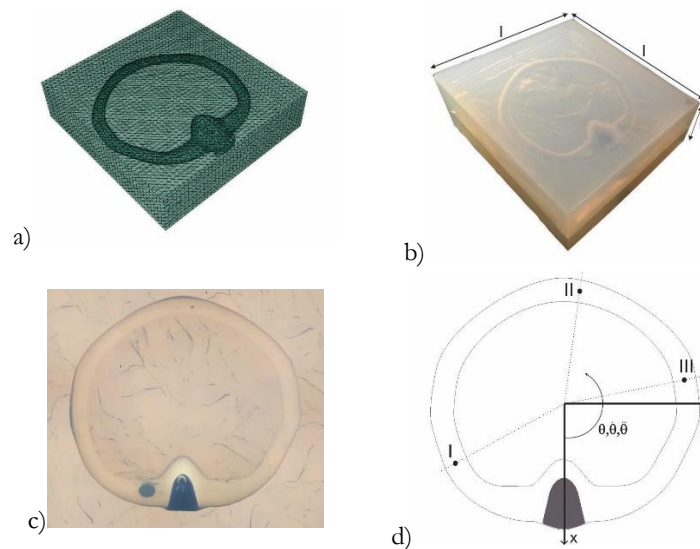


**Figure 3** – SCC experimental model. a) Numerical model, b) Experimental model, c) Experimental model during the experiment d) Angle obtained.

The silicone used was translucent, since it was necessary to analyze the motion inside the experimental model during the experiment, Figure 3c). Furthermore, the used material allows for a color pigmentation to be applied, a useful feature to distinguish different structures, thus a blue pigment was applied to the cupula to easy its recognition during image analysis. Also, the cupula structure was built using a material with a lower hardness, in order to simulate the structure softness. The real microscopic dimension of the SCC is one of the main obstacles to experimental studies on the subject, hence the silicone model was manufactured using a scale ratio of 1:20 in order to promote improved visual measurement conditions. The endolymph was simulated as water, since it has similar mechanical properties and an analogous behavior. To

simulate the otoconia, chalk spheres with a diameter of 0.3 mm were used, due to the calcium carbonate composition, similar to the composition of the real structure.

In the set of performed experiments, the silicone SCC model was positioned in a rotating support, filled with water, and finally an angular movement was applied. The experiment was recorded in video. The digital image processing analysis allowed to obtain the actual angular velocity, which was later applied as an input boundary condition in the computational simulation. Three different otoconia starting locations were defined, as shown in Figure 3d), pointed as I, II and III. The same configuration was established in the experimental and numerical models. The angle ($\theta$), as a function of time, between the otoconia position and the cupula was measured (using the cross product between both vectors), which is compared in the next section.

## 3.Results

Analyze the output video of the experimental data with the three distinct initial otoconia locations allowed to obtain the movement law of each experiment. Then, the corresponding discrete movement law was applied as an input in the numerical simulations, respecting the same otoconia positions and boundary conditions. The angle ($\theta$) obtained between the otoconia position and the reference axis ($Ox$) fixed to the cupula (as a function of time), due to the imposed movement law, is shown in the Figure 4 for both experimental and numerical models.



a)

b)



c)
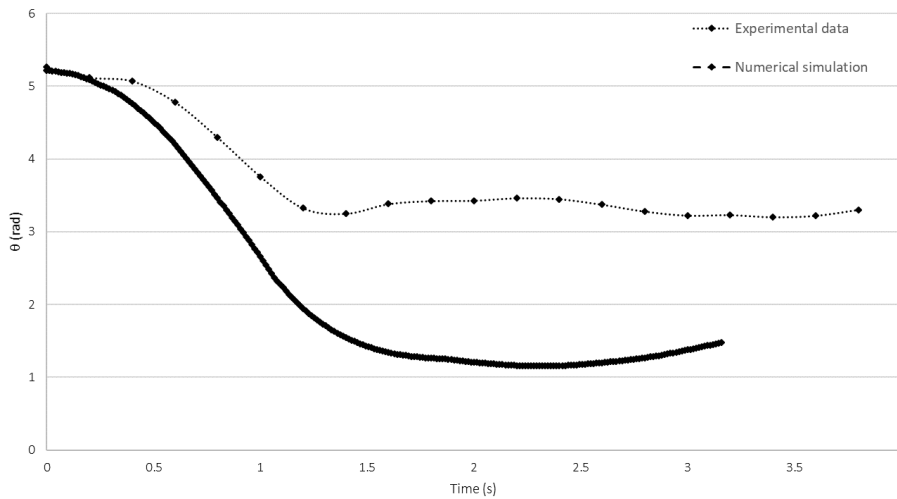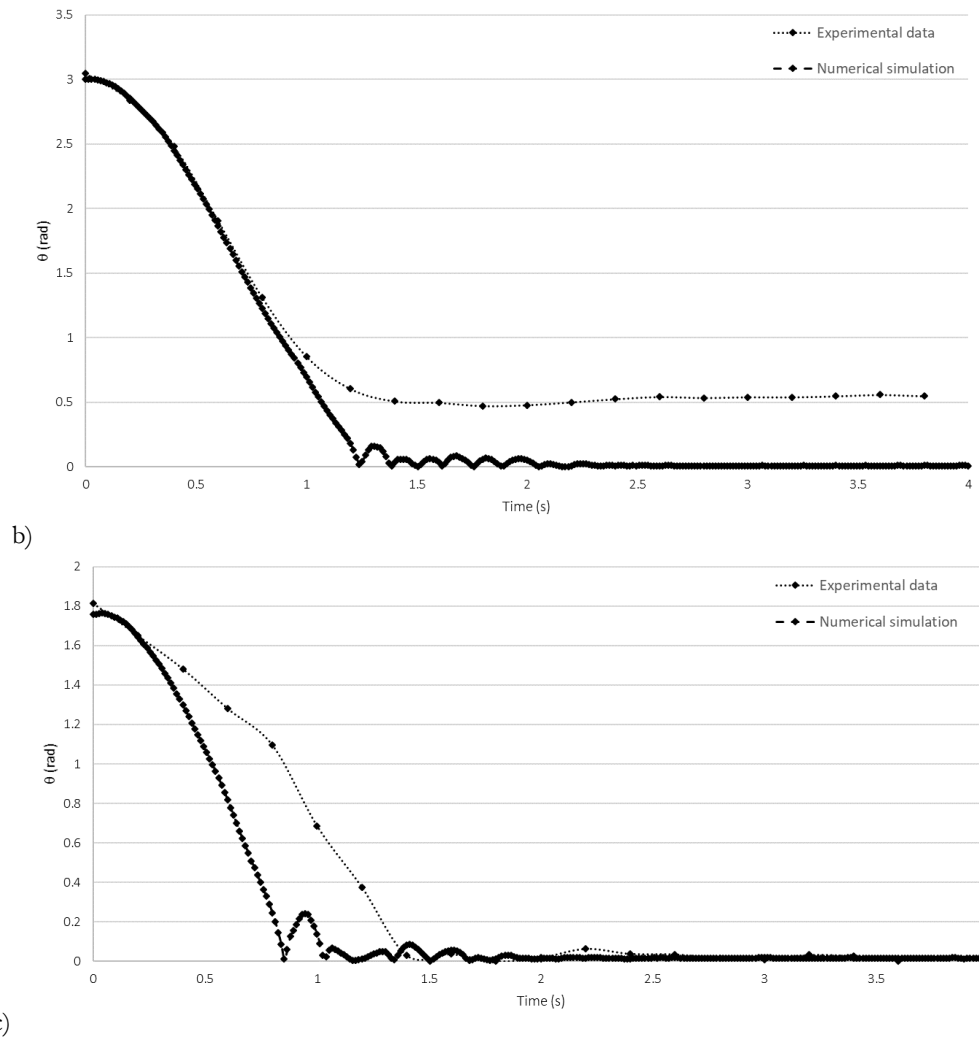
**Figure 4** – Angle (θ) between the otoconia and reference axis (Ox) fixed to the cupula, experimental and numerical comparison in three different situations. a)I; b)II, c)III.

The results presented in Figure 4a) corresponds to the situation where the otoconia had assume the initial position I, shown in Figure 3d), presenting an initial angle $\theta = 5.2\ rad$ between its position and the reference axis (Ox) fixed to the cupula, measured on the movement direction. Figure 4b) corresponds to situation II, where the otoconia's initial position registered $\theta = 3\ rad$ to the reference axis (Ox) fixed to the cupula. In the last defined case, corresponding to situation III, where the otoconia was closer to the cupula, the initial angle was approximately $\theta = 1.8\ rad$.

Figure 5 represents the real spatial otoconia position, for selected instants, comparing the experimental data with the numerical simulation for the three situations. This visualization allows a clearer perception of the otoconia path towards the cupula in the three simulated situations.
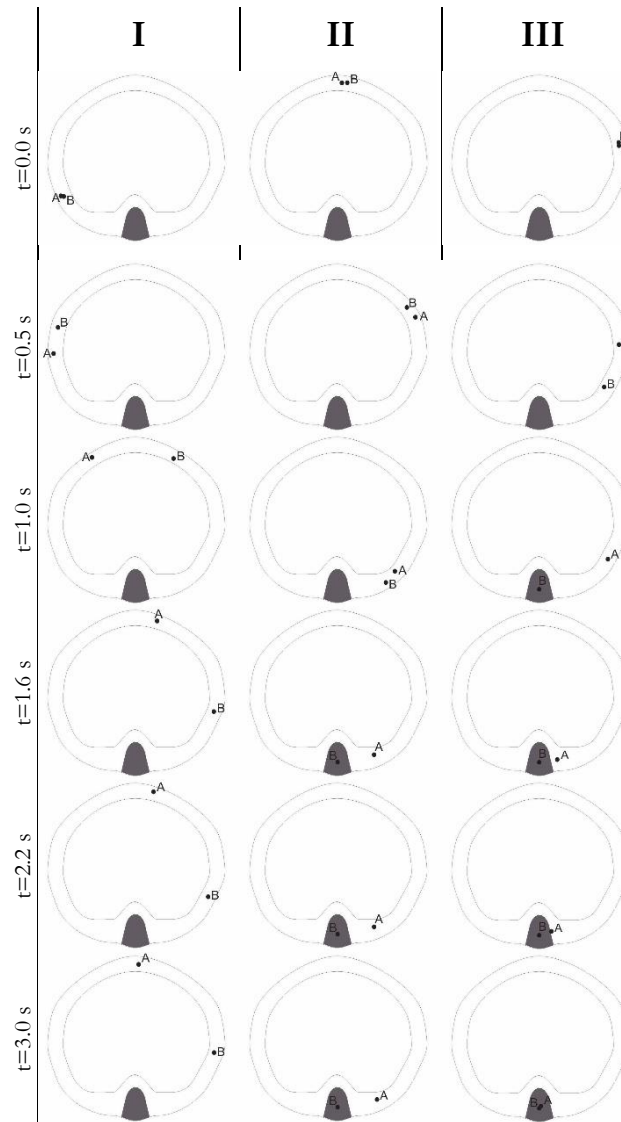
**Figure 5** – Otoconia position along time in the experimental (A) and numerical (B) models in the three simulated siutations.

It is perceptible that the numerical results (B) are generally close with the experimental data (A), validating the numerical approach.

After the model validation, it was analyzed the mechanical behavior of the cupula in the computational model. The influence of the otoconia presence in the cupula behavior was numerically investigated. The results obtained are presented in the Figure 6, representing the transverse displacement of the cupula apex measured in the Oy direction (Figure 3d). Three simulations with the same movement law were performed. The differences between the simulations was the number of otoconia included in the analysis: zero, one or two. In the cases in which otoconia are included, the initial position is the one shown in Figure 1a).
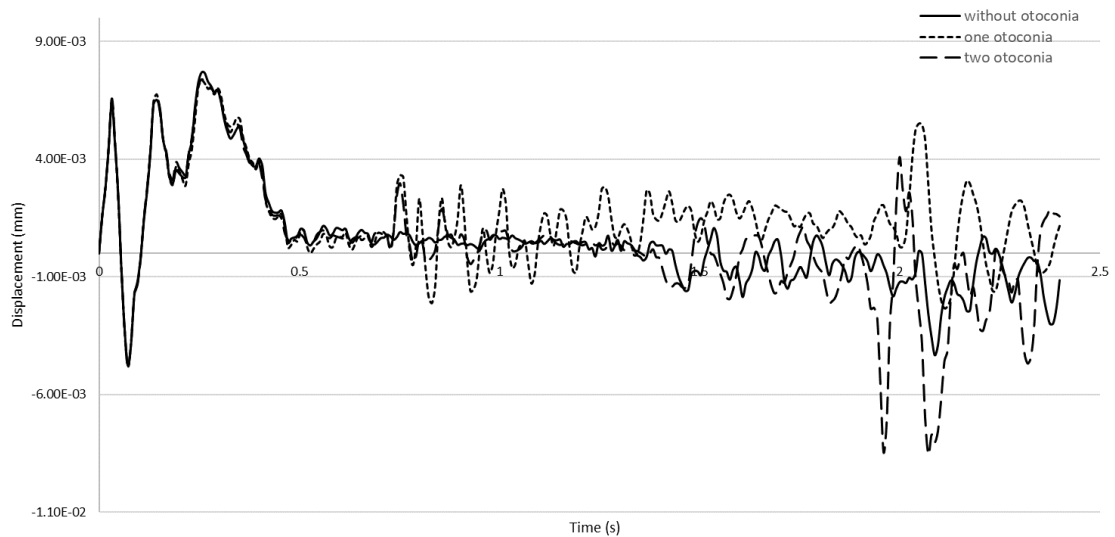
**Figure 6** – Cupula's transverse displacement in three different situations.

The simulation with the vestibular system model were carried out based on the previous validations. An Epley maneuver was applied with an otoconia placed near the cupula in the posterior canal. Considering that some fast movements are applied in this maneuver, the cupula's Young's modulus was slightly adjusted (increased by a factor of 10) to allow a non-deformable simulation without compromising the computational time. The obtained results from the otoconia position inside the vestibular system along time in the rehabilitation maneuver are represented in Figure 7, marked with a red arrow, at specific time instants. The simulation comprises 19 seconds of total time.
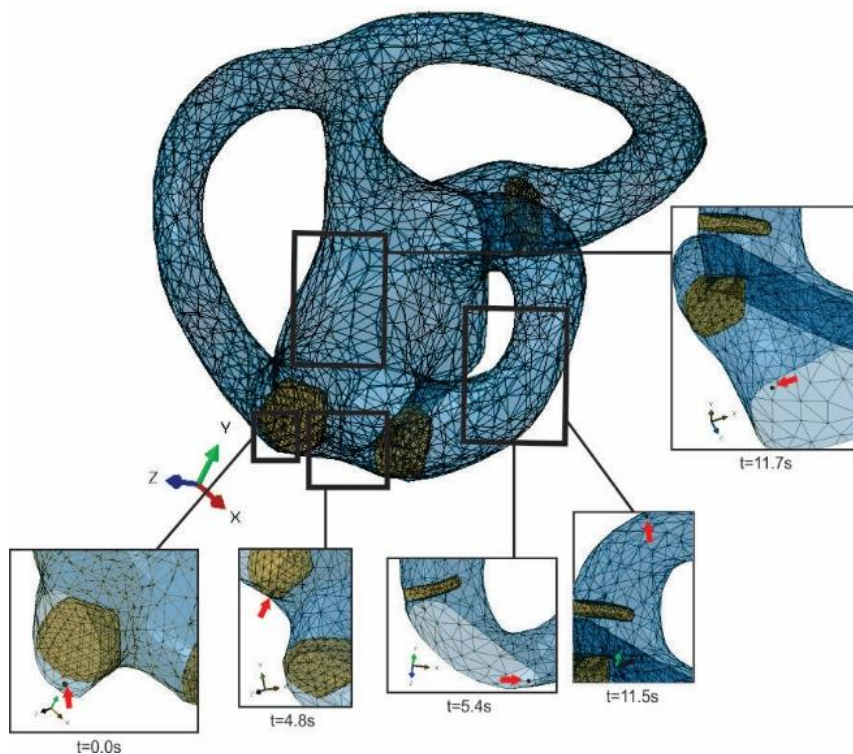


**Figure 7** – Otoconia pathway inside the vestibular system model during Epley maneuver.

56

The time instants between 5.4s and 11.5s regards to the Epley maneuver step when the patient is in the supine position and rotates the head 90 degrees in the opposite direction; which explains the otoconia fall in the vestibule.

# 4.Discussion

Regarding the experimental validation, the results of the computational simulations and experimental tests show a satisfactory similarity. The data comparison is presented in Figure 4. It is possible to observe that in all the situations, the otoconia moves faster along the pathway in the numerical simulation. This can be explained by the friction contact present in the experimental model, conferred by the small irregularities of the silicone surface, mainly due to the mold mesh. Also, the chalk spheres used to simulate the otoconia possess, actually, a rhomboid shape close to the real otoconia particles [23]. All these conditions increase the friction between the structures, which lead to a slower movement of the otoconia, in the experimental simulations.

In experimental cases I and II, the otoconia did not reach the cupula region; actually, the longer the otoconia path to reach the cupula, the farther it stayed in the end of the experiment. This could be explained by materials friction and the same time step imposed. Despite the different velocities of the otoconia in the experimental and numerical data, the otoconia behavior is quite similar. For example, in situation I, in both numerical and experimental tests, the otoconia slightly changes its movement direction at the final segment. This behavior could also be observed in Figure 5. In situation III, which is the shorter path, the otoconia reaches the cupula in both numerical and experimental tests, behaving as expected.

Figure 5 shows the otoconia location at six different time instants, complementing the results of Figure 4. A spatial visualization of the relative position of the otoconia pathway inside the SCC provides a clearer interpretation of the results. Furthermore, the otoconia faster migration noticed in the numerical simulation, is also demonstrated in Figure 5. However, considering the non-linearity of the human tissues, the otoconia pathway of the experimental result is probably closer to the one occurring inside the human ear.

Efforts to normalize the parameters of the experimental tests have been employed, which are evidently conducted in less controlled environments than the numerical simulations. Factors such as friction between materials, manufacturing imperfections, angular velocity application at the initial instant and image aquisition resolution all can influence the accuracy of the results in ways that the numerical simulation does not, leading to some differences between both approaches. Nevertheless, comparing the experimental and numerical results yields a very good

agreement between them. Thus, it can be said that the silicone experimental model allowed the validation of the numerical model, which will be used to support the following simulations using this SCC numerical model.

Considering the results obtained with the simulation of the SCC with and without otoconia, presented in Figure 6, where the cupula transverse displacement was measured in its apex, it can be observed that in the first simulation segment, until 0.5 s, the cupula behavior is similar in the three simulations. This could be explained by the initial position of the otoconia, since it is far from the cupula (as Figure 1a indicate) it will influence less its displacement. During the rest of the simulation, the otoconia is getting closer to the cupula, which influences more the cupula's movement.

Despite the perceived differences in cupula displacement between the three situations along time, the larger displacement was achieved for the case with two otoconia. However, comparing with the one otoconia situation, the displacement is not twice higher, as could be expected. This could be justified because in the two otoconia simulation, one of them slowed the migration half-way from the cupula, probably due to a turbulent flow situation, which is characterized by chaotic changes in flow velocity.

Since the cupula displacement result obtained from the situation without otoconia had some similarities to the one otoconia situation, this may bring an additional question. This result may lead to the hypothesis that maybe there are people with detached otoconia from the macula, lost in the SCC, who have not possessed dizziness symptoms because influence of detached otoconia in the cupula's displacement is not high enough to be distinguished from a healthy situation.

In order to support this argument, a conversion from mechanical energy to electrical energy, as an electrical impulse, should be performed, with the purpose of accurately evaluate the difference between both cases, since it is the brain's input signal regarding the body balance position that triggers dizziness symptoms.

Regarding the global model results presented in Figure 7, it can be observed that the maneuver was able to replace the otoconia to the expected place (the vestibule). However, it did not occur as the theoretical model propose or expects, at which the otoconia goes all the way through the posterior canal. The results shown that the human shaped cupula possesses an important role in the high efficiency rates on such empirical rehabilitation process, since it allows a less restricted otoconia flow inside the labyrinth. The visual representation of such a vestibular rehabilitation procedure could be unclear, therefore, the specific time instants chosen to represent the rehabilitation simulation was defined in crucial steps to understand the otoconia position.

# 5. Conclusion

The SCC numerical model validation shown in the present work opened a new branch in vestibular research. The cupula displacement results have shown the differences between a healthy SCC and a pathological one in a case of detached otoconia, which lead to the dizziness symptoms. However, further work is required to accurately distinguish the influence of otoconia in the cupula behavior. The global vestibular model simulation of a regular rehabilitation maneuver, commonly performed in BPPV situations, has shown that a human shaped cupula increases the possibility of obtaining a desirable therapy result.

Concluding, the computational simulation of such structures and procedures is an essential step in the biological tissues research, mainly for the following considerations: the confirmed accurate results obtained in several fields, the possibility to analyze in controlled environments those fragile and small anatomical configurations, and the advantage of eliminating (almost) all ethical barriers.

## References

[1]    S. Herdman, *Vestibular rehabilitation*. F.A. Davis, 2007.

[2]    S. P. Broglio, J. J. Sosnoff, K. S. Rosengren, and K. McShane, "A comparison of balance performance: computerized dynamic posturography and a random motion platform.," *Arch. Phys. Med. Rehabil.*, vol. 90, no. 1, pp. 145–50, Jan. 2009.

[3]    J. L. Davis, J. Xue, E. H. Peterson, and J. W. Grant, "Layer thickness and curvature effects on otoconial membrane deformation in the utricle of the red-ear slider turtle: static and modal analysis.," *J. Vestib. Res.*, vol. 17, no. 4, pp. 145–62, 2007.

[4]    J. M. Wolfe, *Sensation &amp; perception*. Sinauer Associates, 2012.

[5]    D. A. Winter, "Human balance and posture standing and walking control during," 1995.

[6]    F. B. Horak, "Clinical assessment of balance disorders," *Gait Posture*, vol. 6, no. 1, pp. 76–84, Aug. 1997.

[7]    H. Reisine, J. I. Simpson, and V. Henn, "A geometric analysis of semicircular canals and induced activity in their peripheral afferents in the rhesus monkey.," *Ann. N. Y. Acad. Sci.*, vol. 545, pp. 10–20, 1988.

[8]    R. Jaeger, A. Takagi, and T. Haslwanter, "Modeling the relation between head orientations and otolith responses in humans.," *Hear. Res.*, vol. 173, no. 1–2, pp. 29–42, Nov. 2002.

[9]    World Health Organization, "Falls," 2018.

[10]   S. J. Herdman, *Vestibular rehabilitation.*, vol. 26, no. 1. 2013.

[11]   E. I. Ismail, A. E. Morgan, and M. M. Abdeltawwab, "Home particle repositioning maneuver to

prevent the recurrence of posterior canal BPPV," *Auris Nasus Larynx*, vol. 45, no. 5, pp. 980–984, Oct. 2018.

[12]   H. B. Henninger, S. P. Reese, A. E. Anderson, and J. A. Weiss, "Validation of computational models in biomechanics.," *Proc. Inst. Mech. Eng. H.*, vol. 224, no. 7, pp. 801–12, 2010.

[13]   D. A. Oliveira, M. P. L. Parente, B. Calvo, T. Mascarenhas, and R. M. Natal Jorge, "Numerical simulation of the damage evolution in the pelvic floor muscles during childbirth.," *J. Biomech.*, vol. 49, no. 4, pp. 594–601, Feb. 2016.

[14]   M. E. T. Silva, S. Brandão, M. P. L. Parente, T. Mascarenhas, and R. M. Natal Jorge, "Biomechanical properties of the pelvic floor muscles of continent and incontinent women using an inverse finite element analysis," *Comput. Methods Biomech. Biomed. Engin.*, vol. 20, no. 8, pp. 842–852, Jun. 2017.

[15]   C. F. Santos, J. Belinha, F. Gentil, M. Parente, and R. N. Jorge, "An alternative 3D numerical method to study the biomechanical behaviour of the human inner ear semicircular canal.," *Acta Bioeng. Biomech.*, vol. 19, no. 1, pp. 3–15, 2017.

[16]   S. P. Hibbit D, Karlsson B, "Software License Agreement for Academic Institutes," 2004.

[17]   G. R. Liu and M. B. Liu, *Smoothed Particle Hydrodynamics*. WORLD SCIENTIFIC, 2003.

[18]   J. Bonet and S. Kulasegaram, "Correction and stabilization of smooth particle hydrodynamics methods with applications in metal forming simulations," *Int. J. Numer. Methods Eng.*, vol. 47, no. 6, pp. 1189–1214, Feb. 2000.

[19]   T. Ye, N. Phan-Thien, and C. T. Lim, "Particle-based simulations of red blood cells-A review.," *J. Biomech.*, vol. 49, no. 11, pp. 2255–2266, Jul. 2016.

[20]   I. S. Curthoys and C. M. Oman, "Dimensions of the Horizontal Semicircular Duct, Ampulla and Utricle in the Human," *Acta Otolaryngol.*, vol. 103, no. 3–4, pp. 254–261, Jan. 1987.

[21]   W. Daocai, W. Qing, W. Ximing, H. Jingzhen, L. Cheng, and M. Xiangxing, "Size of the semicircular canals measured by multidetector computed tomography in different age groups.," *J. Comput. Assist. Tomogr.*, vol. 38, no. 2, pp. 196–9, 2014.

[22]   R. Kniep, D. Zahn, J. Wulfes, and L. E. Walther, "The sense of balance in humans: Structural features of otoconia and their response to linear acceleration," *PLoS One*, vol. 12, no. 4, p. e0175769, Apr. 2017.

[23]   L. E. Walther *et al.*, "The inner structure of human Otoconia," *Otol. Neurotol.*, vol. 35, no. 4, pp. 686–694, 2014.

[24]   C. Wu, C. Hua, L. Yang, P. Dai, T. Zhang, and K. Wang, "Dynamic analysis of fluid-structure interaction of endolymph and cupula in the lateral semicircular canal of inner ear," *J. Hydrodyn. Ser. B*, vol. 23, no. 6, pp. 777–783, Dec. 2011.

[25]   J. L. Davis, J. Xue, E. H. Peterson, and J. W. Grant, "Layer thickness and curvature effects on otoconial membrane deformation in the utricle of the red-ear slider turtle: static and modal analysis.," *J. Vestib. Res.*, vol. 17, no. 4, pp. 145–62, Jan. 2007.

[26]   W. Steinhausen, "Über die Beobachtung der Cupula in den Bogengangsampullen des Labyrinths des lebenden Hechts," *Pflugers Arch. Gesamte Physiol. Menschen Tiere*, vol. 232, no. 1, pp. 500–512, Dec. 1933.

[27]   H. Jijiwa *et al.*, "Does the endolymph pass through the base of the cupula?," *Acta Astronaut.*, vol. 49, no. 3–10, pp. 365–369, Aug. 2001.

[28]   J. W. Grant and W. C. Van Buskirk, "Experimental measurement of the stiffness of the cupula," *Biophys. J.*, vol. 16, no. 6, pp. 669–678, Jun. 1976.

[29]   R. Vega, V. V Alexandrov, T. B. Alexandrova, and E. Soto, "Mathematical Model of the Cupula-Endolymph System with Morphological Parameters for the Axolotl (Ambystoma tigrinum) Semicircular Canals.," *Open Med. Inform. J.*, vol. 2, pp. 138–48, Jan. 2008.

[30]   E. Doutel, J. Carneiro, J. B. L. M. Campos, and J. M. Miranda, "Experimental and numerical methodology to analyze flows in a coronary bifurcation," *Eur. J. Mech. - B/Fluids*, vol. 67, pp. 341–356, Jan. 2018.

## 2.5.    Highlights of Contribution IV

The present contribution aimed to obtain the natural frequencies of vibration of the cupula in distinct situations testing a new meshless formulation.

Therefore, the main contents of this publication include:

I.    A succinct comparison between FEM and meshless approaches;

II.   Detailed description of the meshless formulation (NNRPIM), including integration scheme, nodal connectivity and shape functions [41];

III.  Free vibration analysis of the cupula using FEM and NNRPIM, with two models (2D and 3D), and also using four different types of mesh discretization for each model;

IV.   Acquisition of the natural frequencies of the cupula with both methodologies:

Regarding the results, Figure 1.8 shows the three first vibration modes of the two dimensional cupula using the FEM and NNPRIM (using a low order nodal connectivity) and the corresponding natural frequencies. The mesh discretization presented correspond to the most (M4 with 3221 elements) and less (M1 with 131 elements) refined meshes. The full manuscript presents the obtained results with the four meshes, plus the results using a higher order nodal connectivity in the NNRPIM. Furthermore, the three dimensional cupula results are shown as well.



|   | FEM | | NNRPIM | |
|---|---|---|---|---|
|   | M1 | M4 | M1 | M4 |
| 1 | 57.17 Hz | 53.13 Hz | 53.43 Hz | 52.60 Hz |
| 2 | 127.08 Hz | 117.88 Hz | 122.89 Hz | 117.68 Hz |

| 135.86 Hz | 128.90 Hz | 129.69 Hz | 128.05 Hz |
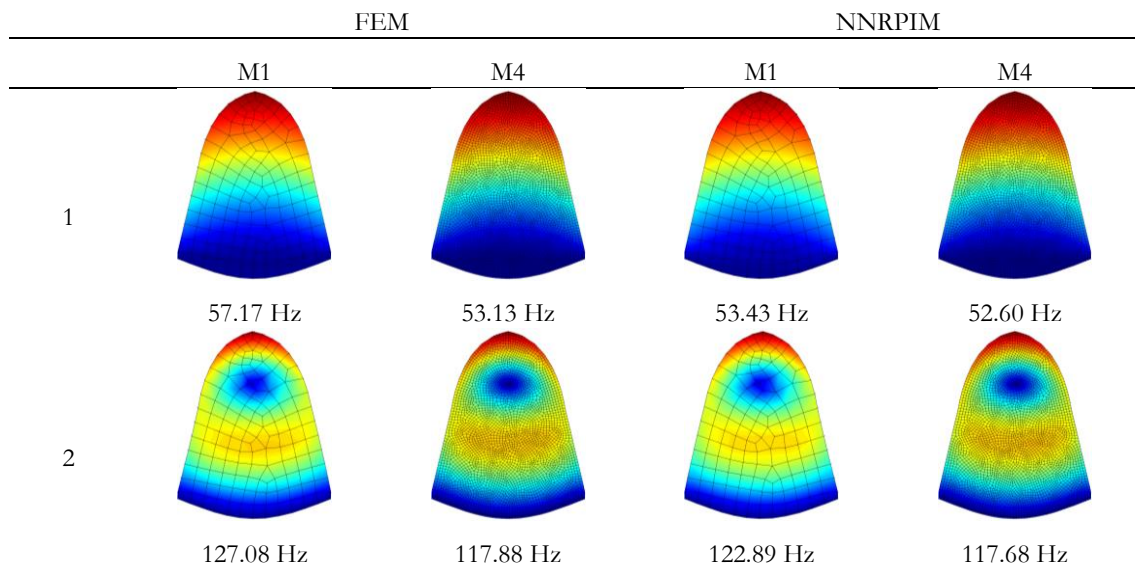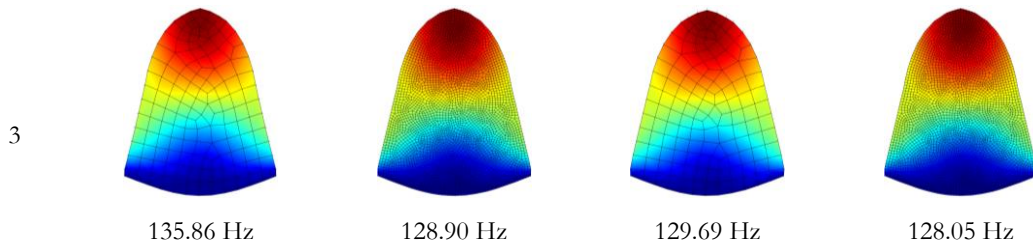
**Figure 1.8** – Three first modes and natural frequencies of the two-dimensional cupula with FEM and NNRPIM using two different meshes.

This vibration modes visualization option corresponds to a fictitious displacement field, where the red color corresponds of the potential maximum displacement value and the blue color to potential lower displacement values. In the manuscript its shown that NNRPIM formulation possesses a faster convergence than FEM. However, the final converged results are all very close in the three first natural frequencies, regardless of the used numerical formulation.

V.  Evaluation of the influence of fluid surrounding the cupula in the natural frequencies values, resembling a situation close to the cupula environment in the vestibular system;

VI.  Analysis of the natural frequencies in a pathological cupula scenario:

Cupulolithiasis occurs when the otoconia get attached to the cupula, inducing vertigo. Figure 1.9 presents the models built to simulate this pathology, in three distinct situations, with a different number of otoconia debris placed in different locations. All border nodes of the model are constrained in all its degrees of freedom.
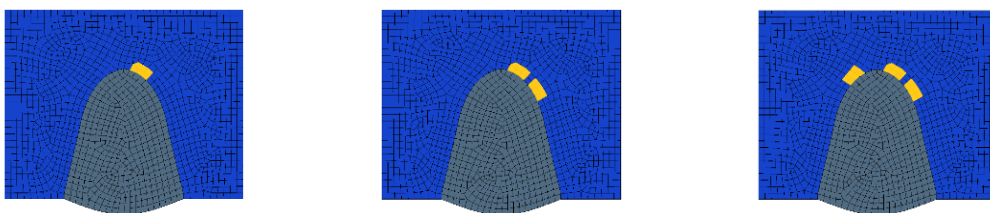


**Figure 1.9** – Two dimensional cupula model surrounded with endolymph and otoconia placed in different location.

The vibration modes obtained in the pathological models are very close to each other. Furthermore, the values of the natural frequencies of the cupula obtained in the pathological and fluid cases are very close to the ones observed in Figure 1.8, indicating that the otoconia debris and the endoymph has a reduced influence in the magnitude of the cupula's natural frequency.

VII. A cross-comparison on both methods was performed using the average differences between the results obtained;

VIII. Conclusions about the efficiency of the used numerical methodologies and the obtained natural frequency values:

The FEM and NNRPIM are capable of achieving similar results regarding the dynamic response of the cupula. Since the obtained natural frequencies of the cupula are in the human auditory range, theoretically, the resonance phenomena could be induced with some melody in order to reduce the vertigo symptoms, by detaching the otoconia from the cupula.

The complete document can be found in the next sub-chapter.

## 2.5.1.    Contribution IV

### <u>The free vibrations analysis of the cupula in the inner ear using a natural neighbor meshless method</u>

Contents lists available at ScienceDirect

# Engineering Analysis with Boundary Elements

journal homepage: www.elsevier.com/locate/enganabound
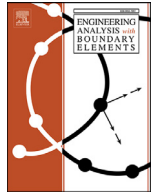
# The free vibrations analysis of the cupula in the inner ear using a natural neighbor meshless method

Carla F. Santos [a],*, J. Belinha [a,b],**, Fernanda Gentil [c], Marco Parente [a,b], Renato Natal Jorge [a,b]

[a] INEGI, Institute of Mechanical Engineering and Industrial Management, Rua Dr. Roberto Frias, 400, 4200-465 Porto, Portugal
[b] Faculty of Engineering of the University of Porto, FEUP, Rua Dr. Roberto Frias, 4200-465 Porto, Portugal
[c] Clínica ORL-Dr. Eurico Almeida, Widex, Escola Superior de Saúde–I.P. Porto, Porto, Portugal

## ARTICLE INFO

## ABSTRACT

The cupula is a part of the inner ear semi-circular canals that plays an important role in the maintenance of the human balance. In order to understand the dynamic response of the cupula, first it is necessary to obtain its vibration frequencies. A two-dimensional and three-dimensional geometrical model of the cupula was built. Then, a free vibration analysis was performed using two distinct numerical techniques, the finite element method (FEM) and the natural neighbor radial point interpolation method (NNRPIM). Besides the fundamental analysis, other scenarios were studied, aiming to analyze the environment of the cupula (in healthy and pathologic scenarios). The results obtained with the geometrical models show that NNRPIM is capable to deliver results very close with the FEM. Additionally, the NNRPIM formulation possesses a high convergence and acceptable computational costs.

This work presents for the first time a computational study on the free vibration analysis of the cupula and shows an alternative numerical technique to calculate with precision the natural frequency of the cupula. The outcomes of this work will allow the development of alternative therapies for cupulolithiasis, which causes severe dizziness.

## 1. Introduction

The vestibular system of the inner ear is the least studied part of the human ear; however, this is the main responsible for the balance function of the human body. When this system fails, the symptoms lead to intense dizziness most of the times. Several mathematical models have been made through the years to represent some parts of the vestibular system [1–5]. The computational simulation of such distinct structures is performed using numerical methods. Today, the preferential numerical method used is the FEM [6] and the most commonly used finite elements are the linear formulation elements, which assume triangle or quadrilaterals shapes for 2D analyses and tetrahedron or hexahedron shapes for 3D analyses [6].

Nowadays, using the computed axial tomography (CAT) imaging technique, it is virtually possible to construct the geometric model of any bio-structure of the human body. Afterward, in order to create a finite element mesh, this geometrical model can be discretized using triangles or quadrilateral elements (2D analyses) or using tetrahedrons or hexahedrons elements (3D analyses). However, this discretization technique could represent a heavy pre-processing cost, especially if a uniform mesh

is intended. Additionally, the model's mesh quality strongly affects the FEM performance, and any mesh refinement during the analysis represents an additional computational cost.

Fortunately, in the last decades, meshless methods [7] have been under strong development and are continuously extending their application field. Today, these more flexible discretization techniques are a competitive and alternative numerical method in computational mechanical analysis, due to the efficiency and accuracy of their discretization formulation [8].

The meshless methods discretize the domain based in a cloud of nodes [7–11], instead of the rigid element concept used in FEM. In the early years, the solution of partial differential equations was the main focus of interest [8]. However, today, meshless methods are applied to a wide-range of applications [10].

Meshless methods can be divided into many classes or even subclasses; one of the most common classification used is the "not-truly meshless methods" or "truly meshless methods" classification [10].

A meshless method is labeled "not-truly" when a background mesh is required to perform the numerical integration of the integro-differential equations ruling the studied physical phenomenon.

---

* Corresponding author.
** Corresponding author at: INEGI, Institute of Mechanical Engineering and Industrial Management, Rua Dr. Roberto Frias, 400, 4200-465 Porto, Portugal.
*E-mail address:* jorge.belinha@fe.up.pt (J. Belinha).

On the other hand, "truly" meshless methods only require an unstructured cloud of nodes to discretize the problem domain. Because the influence domain, integration points, shape functions and other necessary mathematical constructions are obtained directly from the spatial coordinates of the nodes.

Thus, truly meshless methods [10,12–16] are capable to obtain the cloud of nodes using just CAT scan or the MRI images by considering the pixels (or voxels) position. Afterward, using only the nodal spatial information, these truly meshless methods are able to obtain directly the nodal connectivity, the integration points and the shape functions [10]. Furthermore, using the gray range of medical images, truly meshless methods are even capable of recognizing distinct biological structures and then attribute to each node the corresponding material properties [10].

The meshless methods already proved to possess clear advantages over other numerical techniques and to be a reliable option in biomechanics computational applications [17], particularly when combined with medical imaging techniques (CAT scan and MRI) [18,19].

In the literature it is possible to find several research works showing the efficiency of meshless methods in several demanding fields, such as the prediction of crack propagation [20], the analysis of plates assuming functionally graded materials [21] or piezoelectric materials [22] or plate materials damaged by cracks [23]. Regarding the solution requiring the determination of eigen-values and eigen-vectors, meshless methods were efficiently extended to buckling studies [24,25,26] and free vibrations analysis [27,28,29]. Additionally, the literature shows that the structural dynamic analysis assuming truly meshless methods was successfully performed [30].

One of the advantage of meshless methods over FEM are the remeshing efficiency, which in biomechanics structures could be crucial to the final result [31,32].

Thus, due to their formulation, meshless methods allow to introduce or remove nodes from the problem domain without disturbing significantly the final solution. In biomechanics this feature reveals itself to be an advantage because soft tissues (such as muscles, tendons, extra cellular matrix, etc.) and bio-fluids present very large deformations. Therefore, external actions applied to the solid will lead to highly distorted final configurations. If the problem domain is discretized with elements, possibly the final geometry of the elements will be incompatible, leading to the loss of accuracy. In this case, the solution is to create a new element mesh discretizing the geometry of the final configuration. This is an inefficient and time consuming step. Alternatively, in meshless methods there is no pre-established nodal connectivity. Thus, using the concept of influence-domain and the final nodal distribution configuration (naturally adapted to the geometry of the final configuration) a new nodal connectivity will be established, without requiring a new domain remeshing. Additionally, if the nodal discretization is highly distorted, new nodes can be added to the domain to improve the discretization and then the influence-domain concept will allow to enforce the nodal connectivity [10].

Meshless methods have been used to simulate body fluids with low velocities, such as the vestibular system [33,34]. These works apply the smoothed particle hydrodynamics (SPH) technique to capture the fluid/solid interaction occurring between the endolymph and the cupula and otoconia (a highly demanding topic in computational mechanics).

Nevertheless, the main topic of this work is not the study of those fluid/solid interactions but the pioneer analysis of the free vibration of the cupula – a fundamental part of the vestibular system.

At the author's best knowledge, this is the first research work studying the free vibration analysis of the cupula. The main objective of this manuscript is to obtain the natural frequencies of the cupula (both in 2D and 3D) with and without attached otoconia particles. The obtained results will allow to understand the magnitude of the natural frequency of the cupula, allowing to design in the future new therapies to minimize the effects of vertigo.

The numerical analysis is performed using an improved meshless method [12,35],—the NNRPIM—and the FEM (for comparison purposes). Notice that the FEM formulations is well described in the literature, in which several handbooks can be found [6]. The NNRPIM is a truly meshless method [10], which means that it is capable to fully and accurately discretize the problem domain using as information only a micro-CT scan. This is an advantage, since NNRPIM allows to discretize the problem domain using only the nodal cloud coming from the voxel position of the micro-CT scan (no other information is required). Then, using the natural neighbor concept, the Voronoï diagram discretizing the problem domain can be constructed. From the Voronoï diagram it is possible to establish directly the nodal connectivity and define the position and weight of background integration points. The NNRPIM formulation and its extension to free vibration analysis will be described with detailed in the next sections. Afterward, the results obtained from the cupula model will be presented and discussed.

## 2. Nodal connectivity and shape function of natural neighbors

The natural neighbors concept was used for the first time by Sibson for data fitting and smoothing [36,37]. There are two dual mathematical tools used in the determination of the natural neighbors: the Voronoï diagrams [38] and the Delaunay triangulation [39].

Generally, in meshless methods, the nodal connectivity is enforced by the influence-domain concept, in which nodes are searched within a fixed area (in the case of a 2D problem) or a fixed volume (in the 3D problems). Due to its simplicity, several meshless methods use this concept [40–43].

Alternatively, the connectivity between nodes in the NNRPIM is imposed by the "influence-cells" created by the Voronoï diagram [12]. The influence domain formed by $n$ nodes, contribute to the interpolation of the interest point $x_I$ (Fig. 1a) belonging to the problem domain, $\Omega \in \mathbb{R}^3$. There are two types of influence domains, the "First degree influence-cell" and the "Second degree influence-cell". In the first case, an interest point $x_I \in \Omega$ searches for its natural neighbor nodes following the natural neighbors from the Voronoï construction, the second one goes further and add to the cell also the natural neighbor nodes of the first ones. More details can be found in [10].

Regarding the distribution of the background integration points, the NNRPIM uses the Voronoï diagram to define the background distribution of integration points required to integrate the integro-differential equations governing the physical phenomenon. As Fig. 1b shows, following the Delaunay triangulation [10], each Voronoï cell can be divided into quadrilaterals. Then, each quadrilateral sub-cell (Fig. 1c) can be filled with integration points using the Gauss–Legendre quadrature scheme. Previous studies showed that the NNRPIM integration scheme allows to obtain better results than other integration schemes [44].

Notice that the NNRPIM integration scheme is in fact a nodal integration scheme. In the literature it is possible to find several other efficient nodal integration schemes, such as the one combined with the boundary element method [45], or the adaptative integration scheme presented in [46], or the conforming nodal integration scheme proposed in [47].

The NNRPIM uses the radial point interpolators to construct its shape functions. Thus, consider a function $f(x_I)$ defined in the domain $\Omega_I$, which is discretized by a set of $n$ nodes. Notice that $\Omega_I \subset \Omega$ and represent the physical domain of the influence-cell. The interpolation function $f(x_I)$, using the NNRPIM, passes through all nodes in the domain $\Omega_I$, using a radial basis function (RBF) and a polynomial basis function. Assuming that $f(x_I)$ is just affected by the $n$ nodes within the influence-cell of the point of interest $x_I = \{x_I, y_I\}^T$. The value of function $f(x_I)$ at the point of interest $x_I$ is obtained by,

$$f(x_I) = \sum_{i=1}^{n} R_i(x_I) a_i(x_I) + \sum_{j=1}^{m} p_j(x_I) b_j(x_I), = \left\{ \mathbf{R}^T(x_I), \mathbf{p}^T(x_I) \right\} \begin{Bmatrix} a \\ b \end{Bmatrix},$$
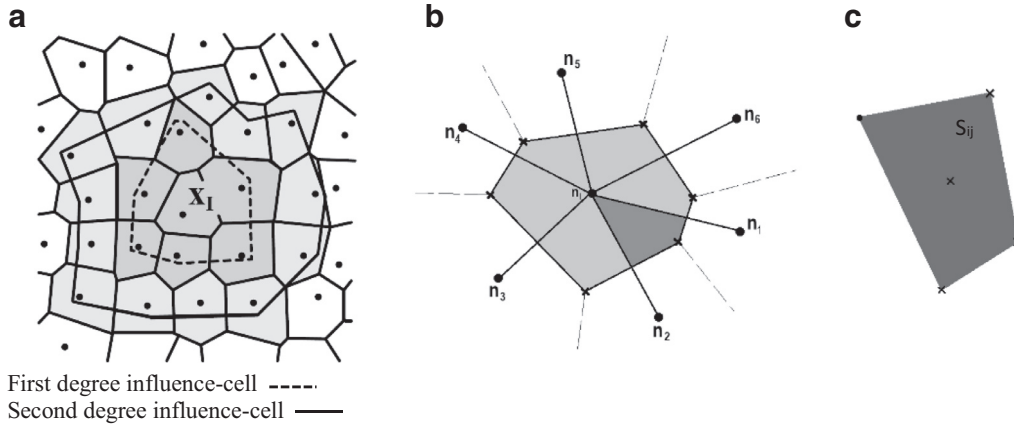
(1)

**Fig. 1.** (a) Influence-cells representation; (b) Voronoï cells; (c) generated quadrilateral.

where $R_i(x_I)$ is the RBF, $n$ is the number of nodes in the influence-cell of $x_I$. The coefficients $a_i(x_I)$ and $b_j(x_I)$ are the non-constant coefficients of $R_i(x_I)$ and $p_j(x_I)$, respectively. The monomials of the polynomial basis are defined by $p_j(x_I)$ and $m$ is the basis monomial number. The variable $r_{ij}$ is the distance between the relevant node $x_i = \{x_i, y_i\}^T$ and the neighbor node $x_j = \{x_j, y_j\}^T$, $r_{ij} = \sqrt{(x_j - x_i)^2 + (y_j - y_i)^2}$. Several known RBFs are well studied and developed in [48,49]. This work uses the Multiquadric (MQ) function $R(r_{ij}) = (r_{ij}^2 + c^2)^p$, proposed initially by Hardy [50], where $c$ and $p$ are two parameters that need to be optimized, since they affect the performance of the RBFs.

Notice that each integration weight should possesses its own $c$ parameter. Thus, for integration point $I$ with an integration weight $\hat{\omega}_I$, the shape parameter $c$ is obtained with: $c_I \cong \gamma \hat{\omega}_I$. This spatial dependence of the RBF's shape parameter is demonstrated in research works available in the literature [10,12]. Previous works on the NNRPIM found that parameter $\gamma$ should be close to zero, $\gamma \cong 0$, and $p$ should be close to one, $p \cong 1$ [10]. However, these values cannot be $\gamma = 0$ and $p = 1$. The use of the exact integer value for $p$ leads to a singular moment matrix and assuming a null $\gamma$ leads to singular moment matrix [10]. Furthermore, previous works [10,12] have shown that values of $p$ very close to the unit allow to obtain the most accurate solutions (regardless the analyzed problem). Thus, the authors have decided to use $p = 1.0001$ or $p = 0.9999$. Additionally, as shown in [10], the parameter $\gamma$ should be very close to zero, because as its value grows, the RPI shape functions lose its interpolation properties. Thus, the authors have selected $\gamma = 0.0001$ in order to "maximize" the RPI interpolation properties. Nevertheless, optimizing the RBF shape parameters is a never-ending research topic [10].

Commonly, the polynomial basis has to possess a low degree to guarantee that the interpolation matrix of RBF is invertible [10]. Thus, in this work the constant polynomial basis is used. Nevertheless, it is possible to include in the formulation several distinct (complete) polynomial basis,

Absence of Basis $\mathbf{x}^T = \{x, y\}$; $\boldsymbol{p}^T(\boldsymbol{x}) = \{0\}$; $m = 0$, (2)

Constant Basis $\boldsymbol{x}^T = \{x, y\}$; $\boldsymbol{p}^T(\boldsymbol{x}) = \{1\}$; $m = 1$, (3)

Linear Basis $\boldsymbol{x}^T = \{x, y\}$; $\boldsymbol{p}^T(\boldsymbol{x}) = \{1, x, y\}$; $m = 3$, (4)

Quadratic Basis $\mathbf{x}^T = \{x, y\}$; $\boldsymbol{p}^T(\boldsymbol{x}) = \{1, x, y, x^2, xy, y^2\}$; $m = 6$, (5)

The polynomial basis has to satisfy an extra requirement in order to obtain an unique solution [51]:

$$\sum_{i=1}^n p_j(x_i) a_i(x_i) = 0, \ j = 1, 2, \ldots, m. \quad (6)$$

in which $n$ represents the number of nodes inside the influence-cell of interest point $x_I$. Therefore, applying Eqs. (1) and (6) to every node forming the influence-cell of interest point $x_I$, a new equation system can be written,

$$\left\{ \begin{array}{c} u_s \\ 0 \end{array} \right\} = \begin{bmatrix} R_Q & P_m \\ P_m^T & 0 \end{bmatrix} \left\{ \begin{array}{c} a \\ b \end{array} \right\} = G \left\{ \begin{array}{c} a \\ b \end{array} \right\} \quad (7)$$

where $u_s$ are the variable values at the nodes inside the influence-cell of interest point $x_I$. It must be noted that the geometric matrix $G$ is a symmetric matrix because the distance is directional independent, i.e., $R(r_{ij}) = R(r_{ji})$. By solving Eq. (7) and substituting its solution into Eq. (1), the shape function $\phi(x_I)$ is obtained,

$$\left\{ \boldsymbol{\varphi}(x_I), \boldsymbol{\psi}(x_I) \right\} = \left\{ \boldsymbol{R}^T(x_I), \boldsymbol{p}^T(x_I) \right\} \boldsymbol{G}^{-1} = \{ \{ \varphi_1(x_1), \varphi_2(x_2), \ldots,$$
$$\varphi_n(x_1) \}, \{ \psi_1(x_1), \psi_2(x_2), \ldots, \psi_m(x_1) \} \} \quad (8)$$

Notice, that the shape function $\phi(x_I)$ is only formed by the first $n$ terms, $\{\phi_1(x_1), \phi_2(x_2), \ldots, \phi_n(x_1)\}$. The last $m$ terms $\{\psi_1(x_1), \psi_2(x_2), \ldots, \psi_m(x_1)\}$ are not included in the shape function vector because they are a by-product of Eq. (8), with no relevant physical meaning associated [10].

Previous works on the RPI [48,49] ensured that the unity partition is verified and, moreover, that these shape functions possess the delta Kronecker property, which simplify the imposition of the essential and natural boundary conditions. The NNRPIM formulation is described with detail in [10].

In this work, both the NNRPIM formulation considering first degree influence cells (NNRPIMv1) and second degree influence cells (NNRPIMv2) were used to solve the numerical examples.

## 3. Free vibration analysis and matrix formulation

Consider a solid with a domain $\Omega$ bounded by $\Gamma$. In the absence damping effects, the dynamic equilibrium based on the principle of virtual work can be written as

$$\int_\Omega \delta \boldsymbol{\varepsilon}^T \boldsymbol{\sigma} d\Omega + \int_\Omega \delta \boldsymbol{u}^T \rho \ddot{\boldsymbol{u}} d\Omega + \int_\Omega \delta \boldsymbol{u}^T \boldsymbol{b} d\Omega - \int_{\Gamma_t} \delta \boldsymbol{u}^T \boldsymbol{t} d\Gamma = 0 \quad (9)$$

where $\boldsymbol{u}$ and $\ddot{\boldsymbol{u}}$ are, respectively, the displacement and the acceleration field, $\boldsymbol{b}$ is the body force vector and $\boldsymbol{t}$ the traction on the natural boundary, $\Gamma_t$. The strain vector $\boldsymbol{\varepsilon}$ is defined as

$$\boldsymbol{\varepsilon} = \boldsymbol{L} \boldsymbol{u} \quad (10)$$

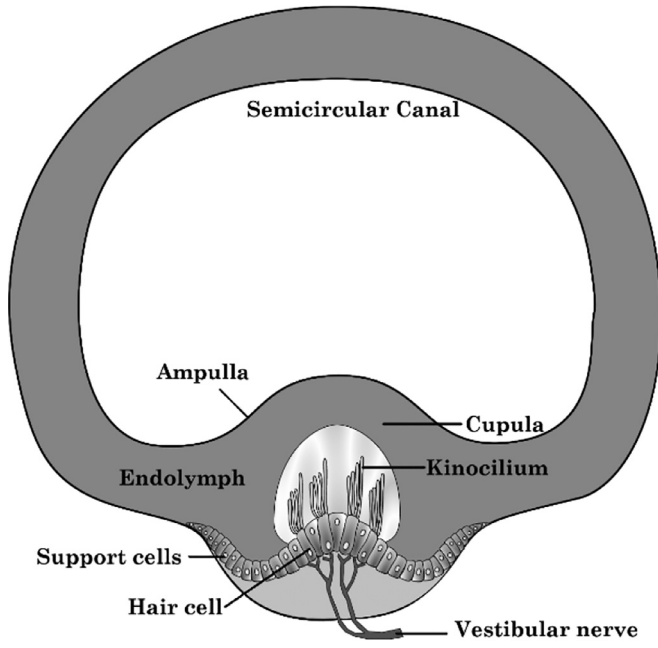where $L$ is the differential operator defined in Eq. (11):

69

**Fig. 2.** Scheme of one SCC of the inner ear with the cupula.

$$L = \begin{bmatrix} \frac{\partial}{\partial x} & 0 & 0 & \frac{\partial}{\partial y} & 0 & \frac{\partial}{\partial z} \\ 0 & \frac{\partial}{\partial y} & 0 & \frac{\partial}{\partial x} & \frac{\partial}{\partial z} & 0 \\ 0 & 0 & \frac{\partial}{\partial z} & 0 & \frac{\partial}{\partial y} & \frac{\partial}{\partial x} \end{bmatrix}^T \tag{11}$$

The linear constitutive relations can be given by

$$\sigma = c\varepsilon \tag{12}$$

Being $\sigma$ the stress tensor and $c$ the material matrix defined as

$$c = \mu_1 \begin{bmatrix} 1 & v & v & 0 & 0 & 0 \\ v & 1 & v & 0 & 0 & 0 \\ v & v & 1 & 0 & 0 & 0 \\ 0 & 0 & 0 & \mu_2 & 0 & 0 \\ 0 & 0 & 0 & 0 & \mu_2 & 0 \\ 0 & 0 & 0 & 0 & 0 & \mu_2 \end{bmatrix} \tag{13}$$

being $\mu_1 = E/(1 - v^2)$ and $\mu_2 = E/(2 + 2v)$, where $E$ is the Young's modulus and $v$ is the Poisson's ratio. In general, the first term of Eq. (9) can be presented as

$$\int_\Omega \delta\varepsilon^T \sigma d\Omega = \delta u \left[ \left[ \int_\Omega B^T c B d\Omega \right] u \right. \tag{14}$$

The second term of Eq. (9) can be developed as

$$\int_\Omega \delta \mathbf{u}^T \rho \, \ddot{u} d\Omega = \int_\Omega \delta(Hu)^T \rho(H\ddot{u}) d\Omega = \delta u \left[ \left[ \int_\Omega H^T \rho H d\Omega \right] \ddot{u} \right. \tag{15}$$

where $B$ is the deformation matrix, defined in Eq. (16), $H$ is the interpolation function diagonal matrix, $H_I = \phi(x_I)I$, and $\rho$ is defined with $\rho = \rho I$, being $\rho$ the mass density of the material and $I$ the identity

matrix with size $3 \times 3$. Thus, the stiffness matrix can be defined as: $K = \int_\Omega B^T c B d\Omega$, and the mass matrix as: $M = \int_\Omega H^T \rho H d\Omega$.

$$B(x_I)_i^T = \begin{bmatrix} \frac{\partial \varphi_i}{\partial x} & 0 & 0 & \frac{\partial \varphi_i}{\partial y} & 0 & \frac{\partial \varphi_i}{\partial z} \\ 0 & \frac{\partial \varphi_i}{\partial y} & 0 & \frac{\partial \varphi_i}{\partial x} & \frac{\partial \varphi_i}{\partial z} & 0 \\ 0 & 0 & \frac{\partial \varphi_i}{\partial z} & 0 & \frac{\partial \varphi_i}{\partial y} & \frac{\partial \varphi_i}{\partial x} \end{bmatrix} \tag{16}$$

The force vectors are defined by developing the third and fourth terms of Eq. (9),

$$F_t = \int_{\Gamma_t} H^T t d\Gamma_t \text{ and } F_b = \int_\Omega H^T b d\Omega \tag{17}$$

Both vectors can be combined, $F = F_t + F_b$. The essential boundary conditions can be directly imposed in the mass matrix and in the stiffness matrix as in the FEM, since the NNRPIM interpolation function possesses the delta Kronecker property. Thus, the equilibrium equations governing the linear dynamic response, neglecting the damping effect, can be represented in the matrix form

$$M\ddot{U} + KU = F \tag{18}$$

where $U = u$ and $\ddot{U} = \ddot{u}$. The fundamental mathematical method used to solve Eq. (18) is the separation of variables. This approach [52] assumes that the solution can be expressed in the following form:

$$U(t) = \Phi X(t) \tag{19}$$

where $\Phi$ is an $n_{3D} \times n_{3D}$ square matrix containing $m$ spatial vectors independent of the time variable $t$, $X(t)$ is a time dependent vector, and $n_{3D} = 3N$ for the 3D formulation, being $N$ the total number of nodes in the problem domain. The components of $X(t)$ are called generalized displacements. From Eq. (19) it follows that $\ddot{U}(t) = \Phi \ddot{X}(t)$. It is required that the space functions satisfy the following stiffness and mass orthogonality conditions:

$$\Phi^T K \Phi = \Omega \quad \text{and} \quad \Phi^T M \Phi = I \tag{20}$$

where $\Omega$ is the diagonal matrix which contains the free vibration frequencies, $\omega_i^2$. After substituting Eq. (20) and its derivatives in order to time into Eq. (18) and pre-multiplying it by $\Phi^T$, the equilibrium equation that corresponds to the modal generalized displacement is obtained. The solution can be presented in the form,

$$u(t) = \phi \sin(\omega(t - t_0)) \tag{21}$$

being $\phi$ the vector of order $n_{3D}$, $t$ the time variable, the constant initial time is defined by $t_0$ and $\omega$ is the vibration frequency vector. Substituting the former solution into Eq. (22) the generalized eigenproblem is obtain, from which $\phi$ and $\omega$ must be determined,

$$K\phi = \omega^2 M \phi \tag{22}$$

Eq. (22) yields the $n_{3D}$ eigensolutions:

$$\begin{bmatrix} K\phi_1 = \omega_1{}^2 M \phi_1 \\ K\phi_2 = \omega_2{}^2 M \phi_2 \\ \vdots \\ K\phi_{n_{3D}} = \omega_{n_{3D}}{}^2 M \phi_{n_{3D}} \end{bmatrix} \tag{23}$$
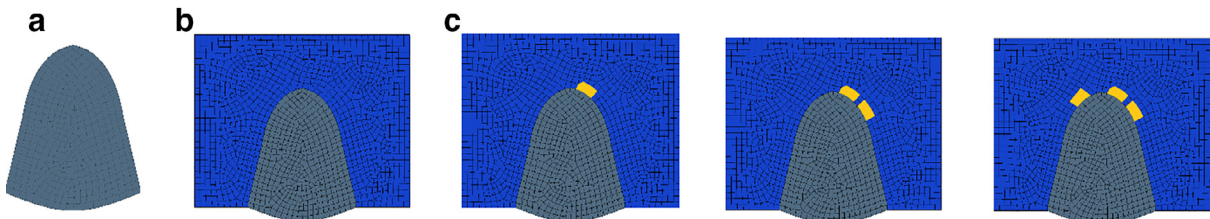


**Fig. 3.** Two dimensional model; (a) Cupula; (b) Cupula with endolymph; (c) Cupula with endolymph and otoconia placed in different location.

70
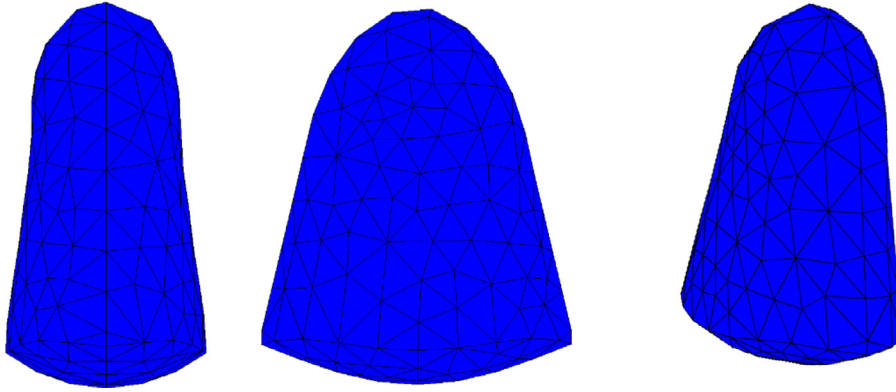
**Fig. 4.** Three-dimensional finite element model of the cupula, front, lateral and three-dimensional views.
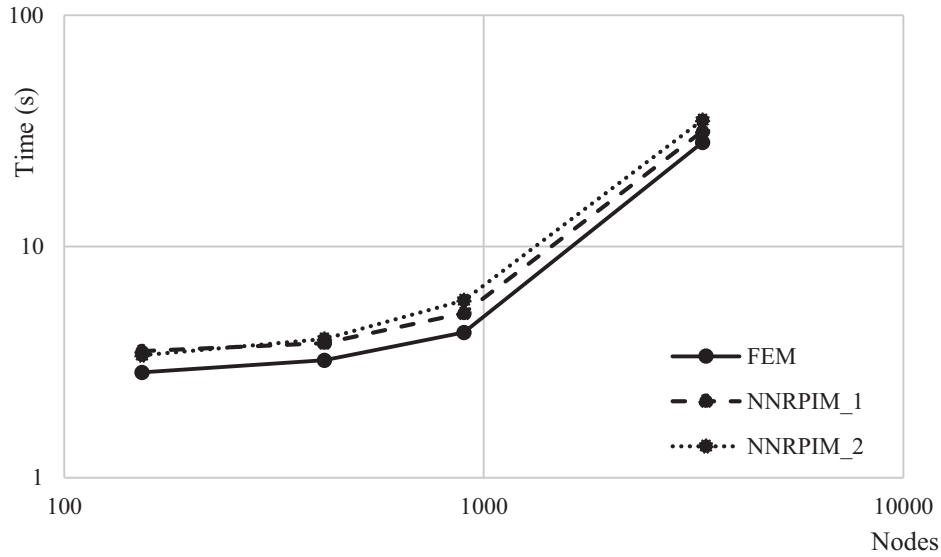


**Fig. 5.** Computational cost for the three methodologies used.

The vector $\phi_i$ is called the $i$th mode shape vector and $\omega_i$ is the corresponding vibration frequency. Defining a matrix $\boldsymbol{\Phi}$ whose columns are the eigenvectors $\phi_i$,

$$\boldsymbol{\Phi} = \begin{bmatrix} \phi_1 & \phi_2 & \cdots & \phi_{n_{3D}} \end{bmatrix} \tag{24}$$

and a diagonal matrix $\mathbf{W}$ which stores the eigenvalues $\omega_i$,

$$\mathbf{W} = \begin{bmatrix} \omega_1{}^2 & 0 & \cdots & 0 \\ 0 & \omega_2{}^2 & \cdots & 0 \\ \vdots & \vdots & \ddots & \vdots \\ 0 & 0 & \cdots & \omega_{n_{3D}}{}^2 \end{bmatrix} \tag{25}$$

the $n_{3D}$ solutions can be written as:

$$K\boldsymbol{\Phi} = \mathbf{M}\,\boldsymbol{\Phi}\,\mathbf{W} \tag{26}$$

It is required that the space functions satisfy the following stiffness and mass orthogonality conditions:

$$\boldsymbol{\Phi}^T K \boldsymbol{\Phi} = \mathbf{W} \tag{27}$$

and

$$\boldsymbol{\Phi}^T \mathbf{M} \boldsymbol{\Phi} = \boldsymbol{I} \tag{28}$$

After substituting Eq. (19) and its time derivatives into Eq. (18) and pre-multiplying by $\boldsymbol{\Phi}^T$, the equilibrium equation that corresponds to the modal generalized displacement is obtained.

## 4. Numerical application

There are two sensory parts of the vestibular system of the inner ear that promote the body balance: the sacs, where particles called otoconia originally located, and the three semicircular canals (SCC), containing the cupula (Fig. 2).

The cupula is a gelatinous hydromechanical sensor that transforms mechanical movement into electrical signals, which are then sent to the brain. The movement of the cupula is induced by the endolymph during the body motion [53,54]. There are many diseases affecting the vestibular system, most of them lead to vertigo, which is the most common symptom in older people. Since vertigo episodes lead to a false sense of rotation (which can cause nausea and vomiting), it is important to avoid that kind of symptoms, which in a severe case could cause a fall [55].

Benign paroxysmal positional vertigo (BPPV) is one of the most common diseases causing vertigo [56]. One particular case of BPPV is cupulolithiasis, which occurs when the otoconia get lost in the SCC and attach to the cupula, inducing a false sensation of movement and leading to vertigo [57]. In this work, the modal generalized displacements of the cupula will be calculated in order to obtain the natural frequency of the cupula and understand the mechanical implications of the attachment otoconia to the cupula.

In order to obtain numerically the free vibration modes of the cupula, 2D and 3D discrete models were built using the standard dimensions and the approximated mechanical properties found in the literature [58].

71
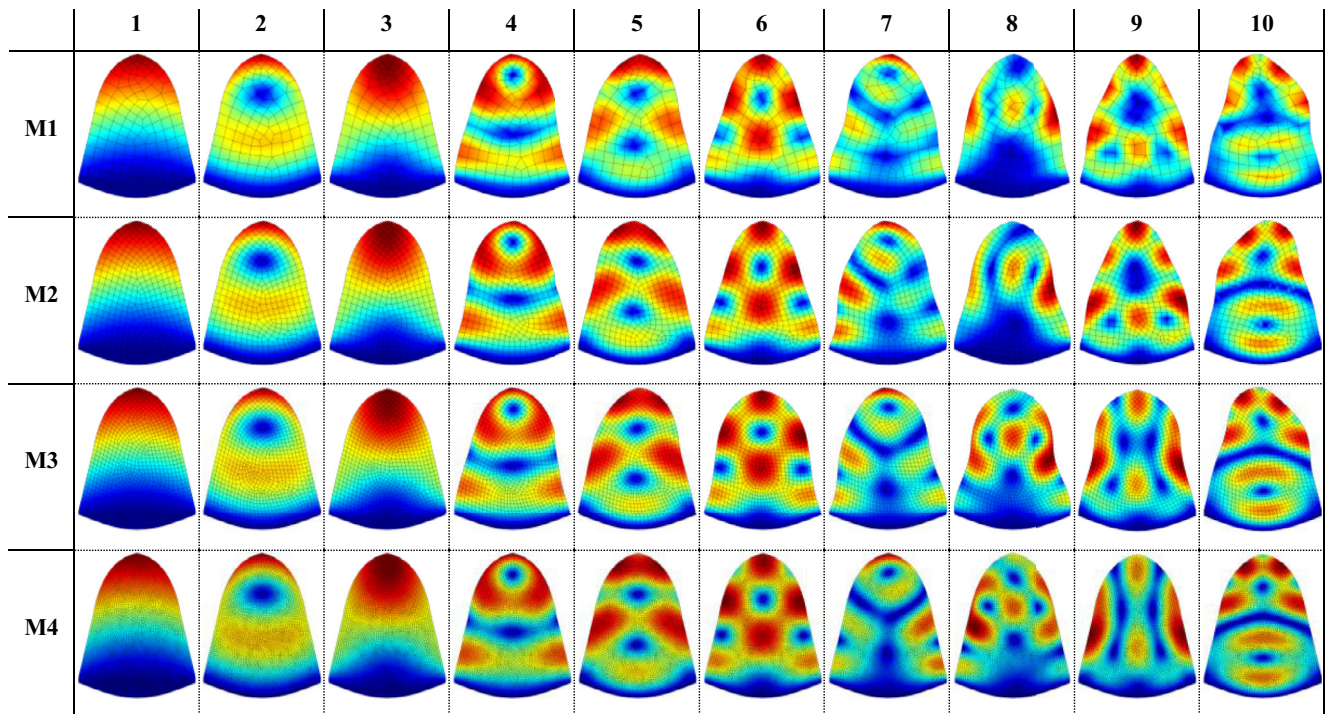
**Fig. 6.** Ten first modes of the two-dimensional cupula with FEM, four meshes. (For interpretation of the references to colour in the text, the reader is referred to the web version of this article.)

### 4.1. Numerical model

First it is presented the 2D model of the cupula (Fig. 3a) that was constructed using quadratic elements. Four different meshes were built: M1 (153 nodes, 131 elements), M2 (417 nodes, 382 elements), M3 (897 nodes, 846 elements) and M4 (3320 nodes, 3221 elements). The endolymph around the cupula was also simulated (Fig. 3b). Regarding the cupulolithiasis, three different simulations were performed with otoconia placed in different location around the cupula (Fig. 3c).

Moreover, a 3D model of the cupula was built using tetrahedral elements (Fig. 4). Thus, four different meshes were built: M1 (350 nodes, 1461 elements), M2 (692 nodes, 3156 elements), M3 (1151 nodes, 5453 elements) and M4 (2128 nodes, 10,704 elements).

Regarding the material properties for the cupula, it was considered the following: $E = 5 \times 10^{-6}$ MPa, $\upsilon = 0.49$ and $\rho = 1 \times 10^{-9}$ ton/mm$^3$ for all simulations. In the case of the otoconia material (calcium carbonate crystals), the properties used are $E = 6.6$ MPa, $\upsilon = 0.45$ and $\rho = 2.4 \times 10^{-9}$ ton/mm$^3$ [58]. To simulate the endolymph, the properties considered are $\rho = 1 \times 10^{-9}$ ton/mm$^3$ $\upsilon = 0.49$ and $E = 1.27 \times 10^{-7}$ MPa. Notice that the endolymph is an incompressible highly viscous fluid, with a dynamic viscosity, $\mu = 0.000852$ Pa s. It was verified (in this work) that the natural frequency of the cupula is around 50 Hz, which means that its period of vibration is $T = 1/50$ s. Thus, knowing that $\dot{\tau} = \mu\dot{\gamma}$ and $\tau = G\gamma$, it is possible to instantaneously approximate the distortion modulus $G$ with $G \cong \mu/T \cong 0.0426$ Pa (valid for the first vibration mode). Thus, since $G = E/(2 + 2\upsilon)$, then $E = 0.127$ Pa.

Regarding the essential boundary conditions, in the 2D and 3D models of the cupula without surrounding fluid, the nodes at the cupula's base are constrained in all its degrees of freedom (no movement is allowed on those nodes). For the 2D models considering the surrounding endolymph, all the boundaries of the model are fully constrained.

### 5. Results

In this section, the results obtained with the simulations performed with FEM and NNRPIM formulations are presented. The results include

the vibration modes and frequencies of the cupula (2D and 3D), the cupula surrounded by the endolymph and also with attached otoconias. The 2D analysis was performed considering the plane strain assumptions and the 3D analysis was performed assuming the formulation presented in Section 3. In this work, the 2D finite element analyses are performed using the standard 2D four nodes quadrilateral element, and the 3D finite element studies are executed considering the standard 3D four nodes constant strain tetrahedron elements [6].

### 5.1. Computational cost

In order to understand the computational efficiency of the NNRPIM, the 2D four nodal meshes previously mentioned (M1, M2, M3 and M4) were analyzed using the FEM and the first degree influence cell NNRPIM formulation (NNRPIMv1) and the second degree influence-cell NNRPIM formulation (NNRPIMv2). It is important to mention that the authors have programed their own NNRPIM and FEM codes, and that all theirs routines were written and analyzed within Matlab© environment. Additionally, the computer used to analyze the problem is an Intel i7 Quad-Core processor, running at 3.6 GHz with 16 GB RAM.

The computational cost of each analysis is plotted in Fig. 5. It is possible to visualize that although the three numerical methods show a similar computational cost, the FEM shows slightly lower computational cost when compared with the NNRPIMv1 and NNRPIMv2. This result was expected, since the FEM obtains the shape-functions using less nodes than the NNRPIM formulation leading, as a consequence, to narrower banded stiffness matrices. Notice that constructing shape functions with a lower number of nodes reduces the computational cost (but decreases also the accuracy of the approximation) and inverting narrower banded stiffness matrices is less time consuming that inverting sparse or broader banded stiffness matrices [10].

### 5.2. Cupula (2D)

The first ten vibration modes of the cupula obtained with the FEM using the four different meshes (M1 to M4) are presented in Fig. 6. In order to visualize automatically both the shape of the vibration mode and
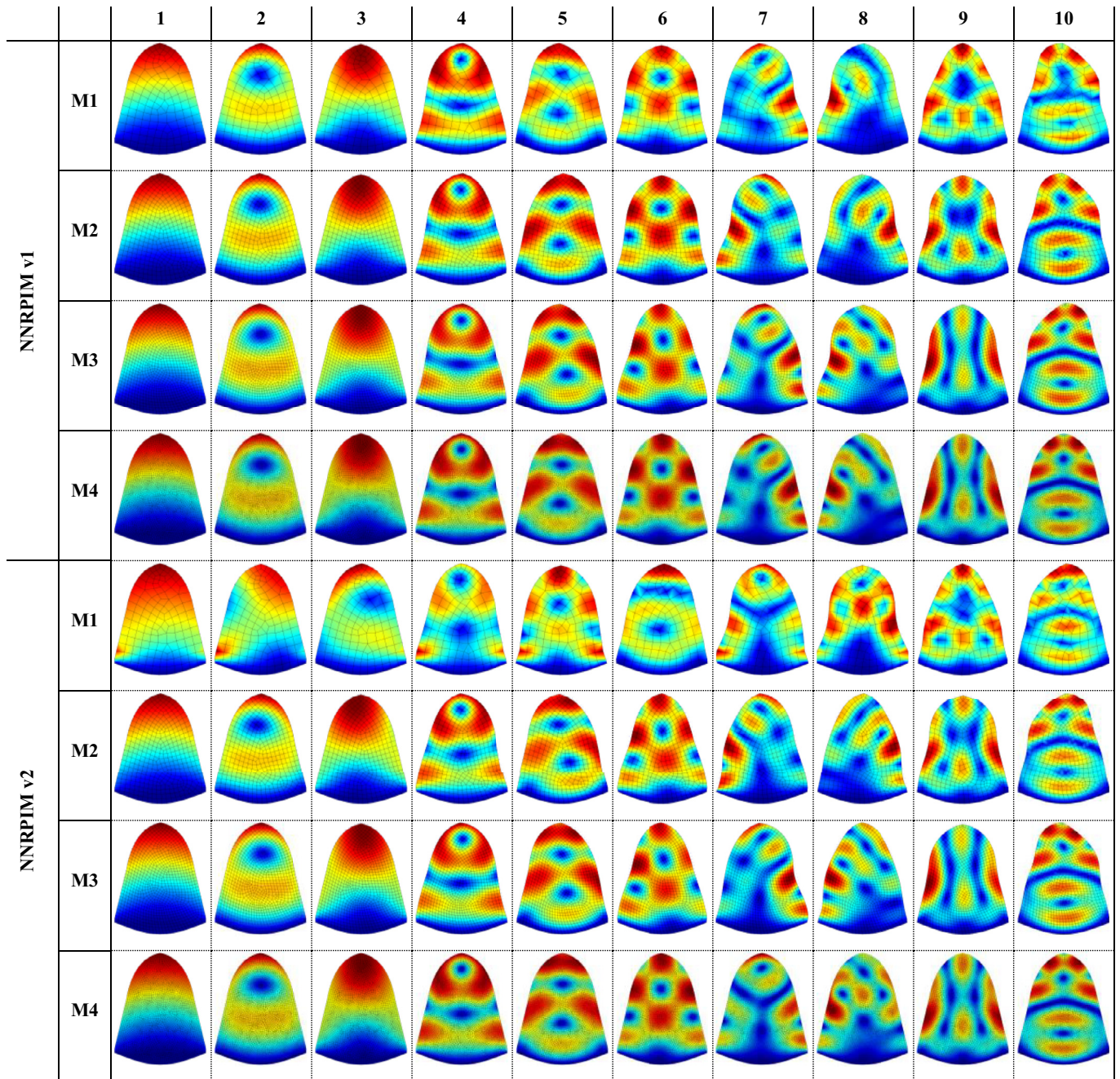
**Fig. 7.** Ten first modes of the two-dimensional cupula with NNRPIM, four meshes.

the vibration frequency, the results of the figures correspond to a fictitious displacement field obtained with: $U_i = \omega_i \varphi_i$. With this visualization technique, it is possible to visualize in each figure the corresponding magnitude of the vibration frequency by observing the maximum value of the displacement, designated by the red color; since the blue color corresponds to the lower displacement values.

Concerning the NNRPIMv1 and NNRPIMv2 analyses, the results of the four different meshes of the cupula are shown in Fig. 7. Additionally, in Table 1 the magnitudes of the first ten vibration frequencies of the analyzed model of the cupula are presented.

In the first and fifth lines of the Fig. 7, corresponding to mesh M1, it is possible to observe that the solution obtained has not yet stabilized. This effect is confirmed analyzing the vibration frequencies of the same modes in Table 1, which are the lower values compared with the natural frequencies of the other meshes. This result is expected, since at this

stage (for mesh M1) the solution has not yet converged. All the other meshes (M2, M3 and M4) and modes (1–10) in the NNRPIM analyses show similar values compared with the equivalent results obtained with FEM (Fig. 6).

As Table 1 shows, the FEM and NNRPIMv1 formulations possess a monotonic convergence path. Notice that the values obtained for the less discretized meshes are monotonically evolving to the ones obtained with the most discretized meshes. In opposition, the NNRPIMv2 formulation appears to achieve the convergence very fast. Although the NNRPIMv2 results obtained with M1 are always very different from the ones obtain with M4, it is possible to visualize that the solution obtained with M2 has already converged, being the results obtained with M2, M3 and M4 almost identical. Furthermore, the final converged results are all very close, regardless the used numerical formulation. The results indicate that first vibration frequency is between 51.71 Hz and 53.43 Hz.

73

| | Resembling Mode 1 | | Resembling Mode 2 | | |
|---|---|---|---|---|---|
| **FEM** | 59.47 Hz | 75.62 Hz | 103.76 Hz | 104.77 Hz | 121.32 Hz |
| **NNRPIMv1** | 61.43 Hz | 78.23 Hz | 111.99 Hz | 120.23 Hz | 122.24 Hz |
| **NNRPIMv2** | 60.15 Hz | 63.50 Hz | 75.81 Hz | 115.86 Hz | 120.03 Hz |



**Fig. 8.** Two first modes of the two-dimensional cupula with endolymph using FEM and NNRPIMv1 and NNRPIMv2.

**Table 1**
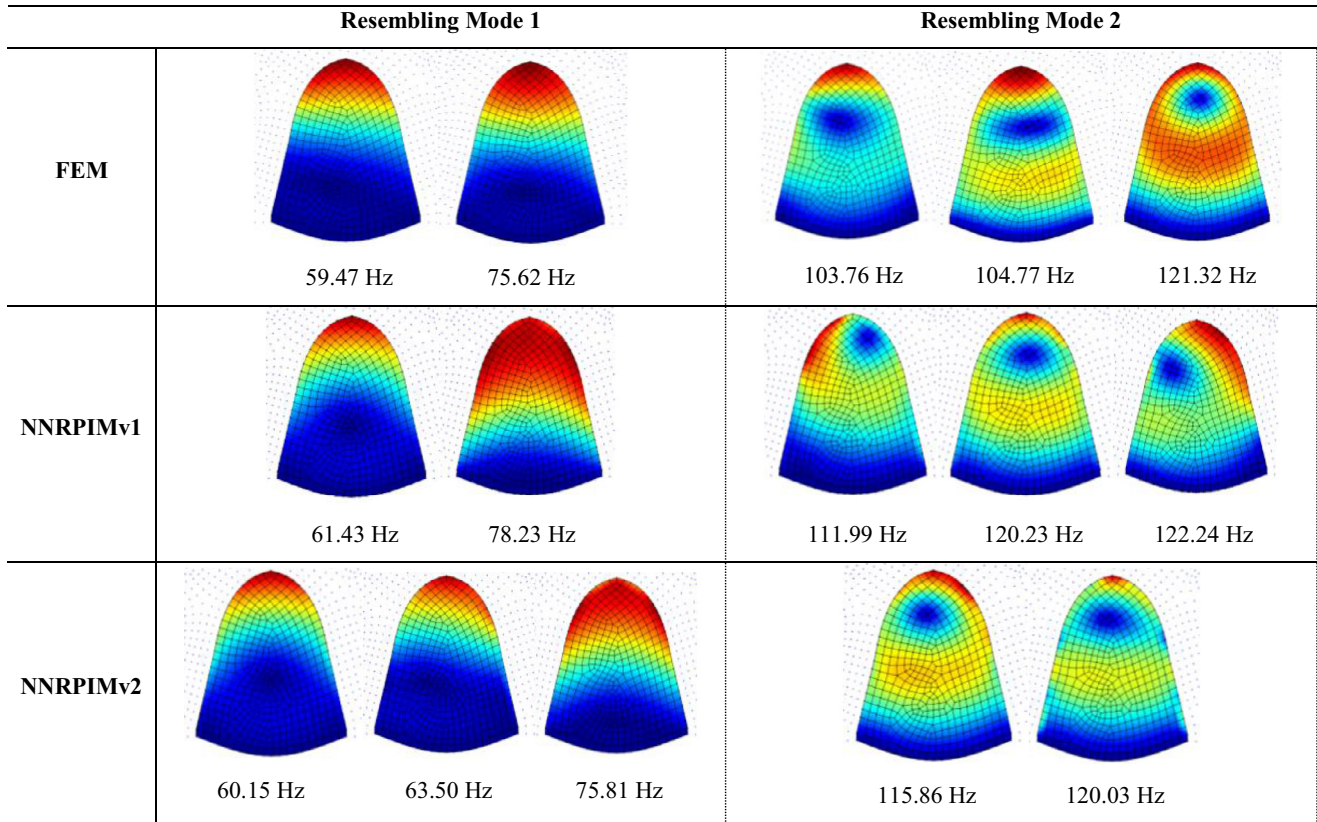Natural frequency of ten first modes of the two-dimensional cupula with FEM and NNRPIM (four meshes).

| | Natural Frequency (Hz) | | | | | | | | | | | |
|---|---|---|---|---|---|---|---|---|---|---|---|---|
| | FEM | | | | NNRPIMv1 | | | | NNRPIMv2 | | | |
| | M1 | M2 | M3 | M4 | M1 | M2 | M3 | M4 | M1 | M2 | M3 | M4 |
| 1 | 57.17 | 54.70 | 54.84 | 53.13 | 53.43 | 54.31 | 53.00 | 52.60 | 23.39 | 51.48 | 51.87 | 51.71 |
| 2 | 127.08 | 121.32 | 119.84 | 117.88 | 122.89 | 119.47 | 117.19 | 117.68 | 103.06 | 117.36 | 116.21 | 117.16 |
| 3 | 135.86 | 131.62 | 131.39 | 128.90 | 129.69 | 130.33 | 128.50 | 128.05 | 111.82 | 126.35 | 126.80 | 126.68 |
| 4 | 239.55 | 226.17 | 222.55 | 217.48 | 223.77 | 219.22 | 216.13 | 215.97 | 187.38 | 213.64 | 213.61 | 214.17 |
| 5 | 277.15 | 259.80 | 254.56 | 248.80 | 262.23 | 254.47 | 249.71 | 247.98 | 234.57 | 249.12 | 247.89 | 247.21 |
| 6 | 283.32 | 265.13 | 259.03 | 253.34 | 265.31 | 257.03 | 254.11 | 251.25 | 252.32 | 251.08 | 251.63 | 249.60 |
| 7 | 369.27 | 345.26 | 337.34 | 328.04 | 336.22 | 331.44 | 329.11 | 325.23 | 301.68 | 321.02 | 323.82 | 322.11 |
| 8 | 382.59 | 350.33 | 340.87 | 331.17 | 343.12 | 336.73 | 331.48 | 327.71 | 316.98 | 330.41 | 329.03 | 324.83 |
| 9 | 404.24 | 362.51 | 350.08 | 340.07 | 373.02 | 346.85 | 340.13 | 337.80 | 344.12 | 338.08 | 337.23 | 336.35 |
| 10 | 428.11 | 386.60 | 372.53 | 360.07 | 390.57 | 371.30 | 360.63 | 357.57 | 367.15 | 361.29 | 357.06 | 356.37 |

Additionally, notice that the following vibration frequencies are much higher, which allow to identify with enough precision the magnitude of frequency of the first mode.

All the natural frequencies obtained are contained in the human hearing range, since it goes from 20 Hz to 20,000 Hz. In general, the natural frequencies obtained with NNRPIM are lower than the ones obtained with FEM.

*5.3. Cupula with endolymph (2D)*

In this subsection, the endolymph is included in the model (Fig. 3b). The objective is to understand the influence of the endolymph in the natural frequency (the first vibration frequency) of the cupula.

Since in the previous section it was verified that the mesh density of mesh M2 is sufficient to obtain accurate results, in this section a similar mesh density is used to discretize the problem domain.

Thus, in order to observe the effect of the endolymph around the cupula, the first five vibration modes of the cupula are presented in the Fig. 8, for the FEM and both NNRPIM analyses, respectively.

Notice that the first two vibration modes obtained with the FEM resemble the first vibration mode obtained in Section 5.2. Furthermore, the third, fourth and fifth vibration modes obtained now are very similar with the second vibration mode obtained in the analysis of the cupula without surrounding fluid (Section 5.2).

The same effect is verified for the NNRPIM, the first three vibration modes of the present analysis resemble the first vibration mode obtained in Section 5.2 and the fourth and fifth vibration modes of the present analysis are very similar with the second vibration mode obtained in Section 5.2.

Regarding the first vibration modes (resembling the natural frequency of the isolated cupula), in this study the following vibration frequencies were obtained: 59 Hz and 75 Hz in FEM, 61 Hz and 78 Hz

74

| | One otoconia | | Two otoconia | | Three otoconia | |
|---|---|---|---|---|---|---|
| | Resembling Mode 1 | Resembling Mode 2 | Resembling Mode 1 | Resembling Mode 2 | Resembling Mode 1 | Resembling Mode 2 |
| **FEM** | 63.90 Hz | 120.39 Hz | 63.07 Hz / 63.97 Hz | 120.74 Hz | 63.14 Hz / 63.85 Hz | 120.39 Hz |
| **NNRPIMv1** | 61.42 Hz | 115.02 Hz | 61.72 Hz | 112.12 Hz | 61.80 Hz | 113.06 Hz |
| **NNRPIMv2** | 60.32 Hz / 68.63 Hz | 114.80 Hz | 61.45 Hz / 63.86 Hz | 118.27 Hz | 61.80 Hz / 64.38 Hz | 118.35 Hz |
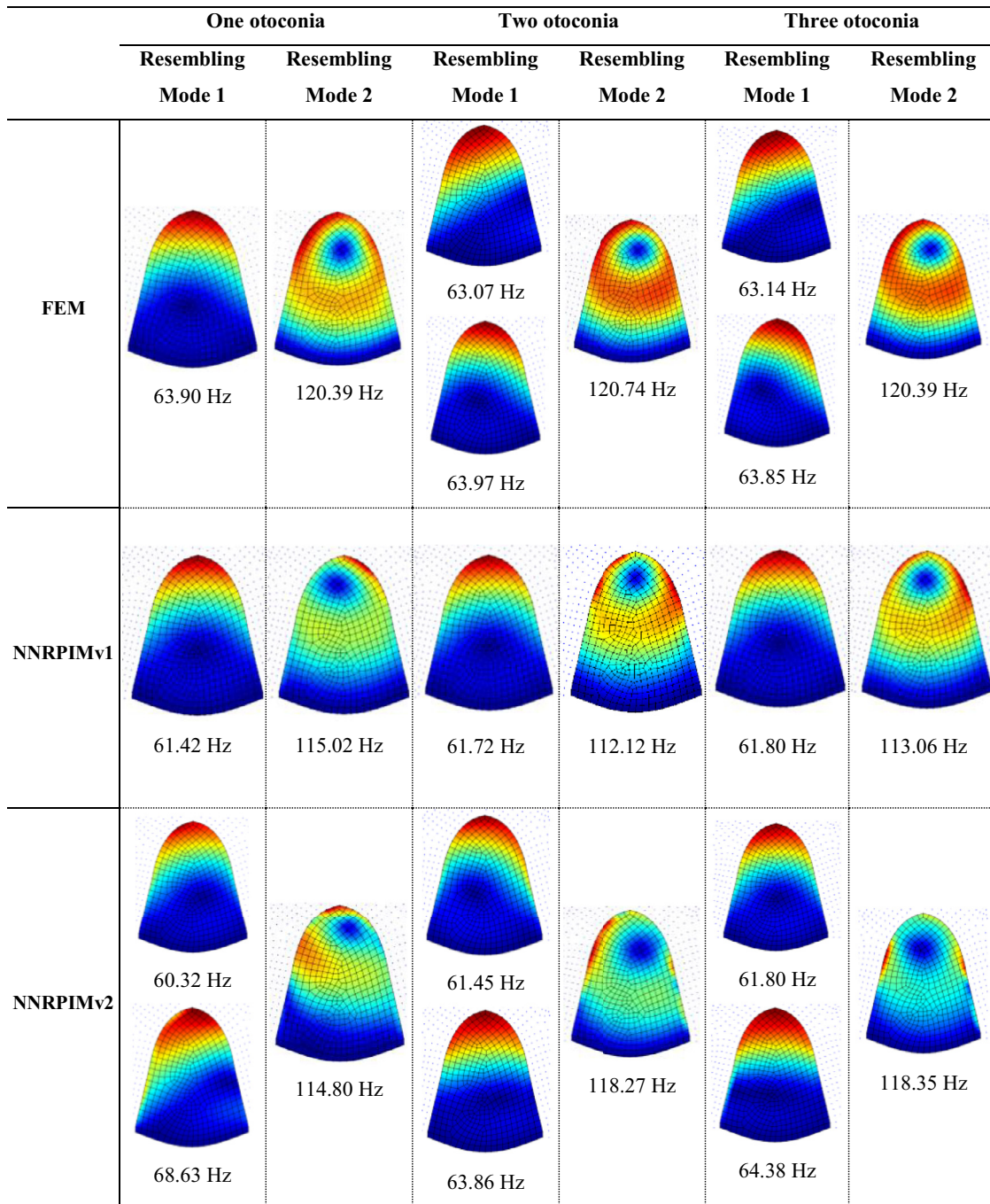
**Fig. 9.** Two first modes of the two-dimensional cupula with endolymph and otoconia using FEM and NNRPIM.

for the NNRPIMv1 analysis and 60 Hz, 63 Hz, and 76 Hz in NNRPIMv2 analysis. Notice that these values are very close with the ones observed in Section 5.2, indicating that the fluid has a reduced influence in the magnitude of the cupula's natural frequency.

*5.4. Cupula with endolymph and otoconia (2D)*

Next, the 2D problem shown in Fig. 3c is analyzed with both FEM and NNRPIM formulations. Here, groups of otoconia are attached to the cupula in different locations (the three locations shown in Fig. 3c), simulating a possible cause for vertigo. With this study it is intended to understand if the inclusion of the otoconia changes significantly the natural frequency of the cupula. In this study, in addition to the otoco-nia, the surrounding fluid is also considered. Again, the density of the discretization used in this study follows the mesh density of mesh M2 presented in Section 4.

The relevant vibration modes obtained, and the corresponding vibration frequencies are presented in Fig. 9.

Fig. 9 shows that the FEM and the NNRPIM produce always very similar vibration modes. It is possible to visualize that vibration modes resembling the first vibration mode found in Section 5.2 present a vibration frequency very close with the one found in Section 5.2.

When one otoconia (or one otoconia group) is considered, the frequencies of the cupula resembling its natural frequency (observed in Section 5.2) are 63.90 Hz in the FEM, 61.42 Hz for the NNRPIMv1, and 60.32 Hz or 68.63 Hz in the NNRPIMv2.

75

| | Vibration Mode 1 | Vibration Mode 2 | Vibration Mode 3 | Vibration Mode 4 | Vibration Mode 5 |
|---|---|---|---|---|---|
| **FEM** | | | | | |
| **NNRPIM v1** | | | | | |
| **NNRPIM v2** | | | | | |



**Fig. 10.** Five first modes of the three-dimensional cupula with FEM, NNRPIMv1 and NNRPIMv2.

Alternatively, if two otoconia (or two otoconia groups) are considered, the frequencies of the cupula resembling its natural frequency (Section 5.2) are 63.07 Hz or 63.97 Hz for the FEM. 61.72 Hz for the NNRPIMv1, and 61.45 Hz or 63.86 Hz for the NNRPIMv2.

If three otoconia (or three otoconia groups) are attached to the cupula, the frequencies resembling its natural frequency, documented in Section 5.2, are 63.14 Hz or 63.85 Hz for the FEM, 61.80 Hz for the NNRPIMv1, and 61.80 Hz or 64.38 Hz for the NNRPIMv2.
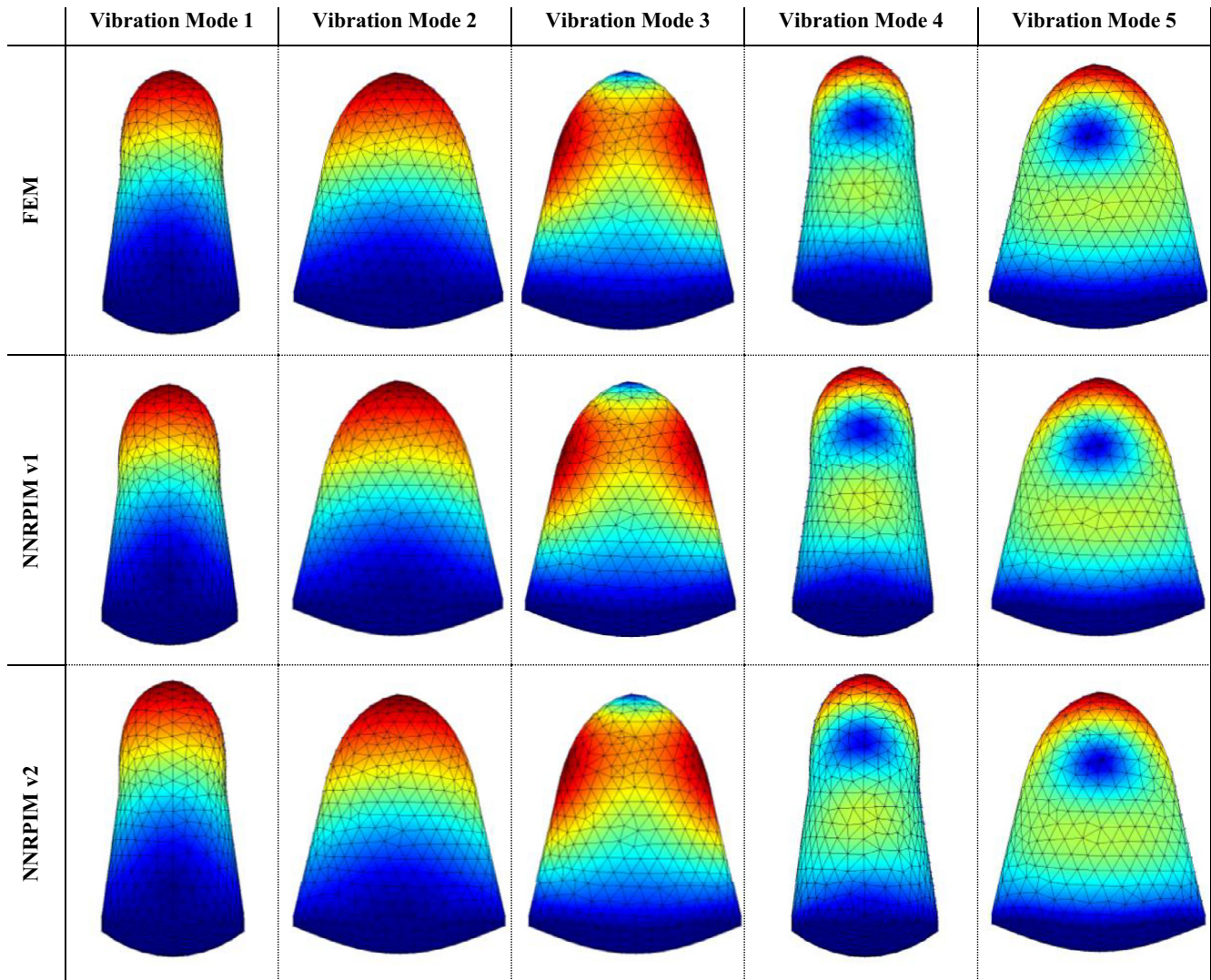
Regarding the apparent second vibration mode obtained with the models with one and two otoconia, from both methods (FEM and NNR-PIM), is it possible to observe a small fictitious displacement of the cupula to the right side comparing with the model with three otoconia, resembling more with the model without otoconia. This trend behavior could be justified with the placement of the otoconia in the right side of the cupula in the two first examples. This result is more evident in the NNRPIM.

On the other hand, the first vibration frequencies obtained from the models with the different number of otoconia are very close between each other. This may indicate that the size of the otoconia particles is not enough to change significantly the vibration frequency of the cupula. Although the FEM and NNRPIM formulations show similar results, the natural frequencies obtained with FEM continue to be higher than the ones obtained with the NNRPIMv1 and NNRPIMv2 formulations.

### 5.5. Cupula (3D)

Expectably, the analysis of the free vibration modes of the 3D cupula will allow to understand in a more realistic way the behavior of the cupula. The free vibration analysis of the 3D cupula is performed with the four meshes shown in Section 4. Nevertheless, in the Fig. 10 are presented only the results obtained with mesh M4 for the first five vibration modes of the cupula with FEM and NNRPIM. The first and fourth modes are represented with the lateral view, the other ones with the front view.

Since the second mode of vibration in the three-dimensional analysis shows a fictitious displacement aligned with the tangent direction of the canal, this second mode of vibration should be the most suitable to induce the necessary movement to restore the otoconia back to the right place.

Table 2 shows the first vibration frequencies obtained for the cupula using the distinct four meshes and the FEM and NNRPIM analysis. It is possible to visualize that both the NNRPIM formulations present high convergence rates. Notice that the solution obtained for meshes M2, M3 and M4 is almost identical. On the other hand, the FEM presents a lower convergence rate. This was expected, since the literature shows that the tetrahedral element possesses lower convergence rates [6].

As already mentioned, the 3D second vibration mode corresponds to the vibration configuration aligned with the tangent direction of the canal. Thus, the 3D second vibration mode corresponds to the 2D first

76

| Numerical technique | | | 2D analysis vibration modes | | | 3D analysis vibration mode | | |
|---|---|---|---|---|---|---|---|---|
| a | b | | $i = 1$ | $i = 2$ | $i = 3$ | $i = 1$ | $i = 2$ | $i = 3$ |
| FEM | NNRPIM v1 | $\xi_i^{a/b} \times 100$ | | | | | | |
| | | $\bar{\xi}_i^{a/b} \times 100$ | 3.10% | 1.57% | 2.82% | 12.26% | 9.91% | 7.60% |
| FEM | NNRPIM v2 | $\xi_i^{a/b} \times 100$ | | | | | | |
| | | $\bar{\xi}_i^{a/b} \times 100$ | 11.4% | 2.11% | 3.60% | 22.03% | 20.97% | 9.95% |
| NNRPIM v1 | FEM | $\xi_i^{a/b} \times 100$ | | | | | | |
| | | $\bar{\xi}_i^{a/b} \times 100$ | 2.7% | 1.57% | 2.78% | 11.48% | 8.21% | 8.87% |
| NNRPIM v1 | NNRPIM v2 | $\xi_i^{a/b} \times 100$ | | | | | | |
| | | $\bar{\xi}_i^{a/b} \times 100$ | 7.5% | 1.68% | 2.38% | 11.70% | 13. 30% | 5.42% |
| NNRPIM v2 | FEM | $\xi_i^{a/b} \times 100$ | | | | | | |
| | | $\bar{\xi}_i^{a/b} \times 100$ | 9.6% | 2.05% | 3.20% | 15.48% | 13.29% | 10.55% |
| NNRPIM v2 | NNRPIM v1 | $\xi_i^{a/b} \times 100$ | | | | | | |
| | | $\bar{\xi}_i^{a/b} \times 100$ | 7.1% | 1.62% | 2.19% | 8.98% | 9.27% | 4.71% |

0%  >10%

**Fig. 11.** Distribution maps $\xi(\boldsymbol{x})_i^{a/b}$ and corresponding average differences $\bar{\xi}_i^{a/b}$.

**Table 2**
Natural frequency of five first modes of the three-dimensional cupula with FEM and NNRPIM (four meshes).

| | Natural Frequency (Hz) | | | | | | | | | | | |
|---|---|---|---|---|---|---|---|---|---|---|---|---|
| | FEM | | | | NNRPIMv1 | | | | NNRPIMv2 | | | |
| | M1 | M2 | M3 | M4 | M1 | M2 | M3 | M4 | M1 | M2 | M3 | M4 |
| 1 | 52.33 | 47.04 | 46.23 | 43.97 | 43.69 | 41.07 | 40.91 | 39.94 | 35.48 | 40.17 | 40.02 | 39.21 |
| 2 | 62.75 | 58.62 | 57.40 | 56.14 | 56.29 | 54.11 | 54.06 | 53.09 | 41.97 | 52.18 | 52.77 | 51.91 |
| 3 | 108.99 | 99.83 | 95.30 | 90.77 | 87.86 | 85.07 | 84.29 | 82.98 | 86.30 | 84.04 | 83.32 | 82.11 |
| 4 | 144.55 | 133.47 | 130.67 | 124.58 | 122.64 | 117.02 | 116.52 | 114.49 | 111.42 | 114.78 | 114.55 | 112.07 |
| 5 | 146.43 | 136.42 | 134.26 | 130.85 | 129.19 | 126.18 | 126.37 | 124.99 | 118.75 | 124.55 | 125.09 | 123.41 |

vibration mode. From Table 2 it is possible to visualize that for the densest mesh (M4), the FEM predicts a second vibration frequency of 56.14 Hz, the NNRPIMv1 predicts 53.09 Hz and the NNRPIMv2 indicates 51.91 Hz. These values are in accordance with the one obtained in the 2D analysis.

### 5.6. Cross-comparison

In order to compare the several formulations, a cross-comparison was performed. Thus, for the 2D analysis, the first three vibration modes obtained in Section 5.2 with the FEM and NNRPIM formulations, using mesh M4, were compared with each other. The cross-comparison was performed with the following described procedure. In the end of each analysis the first three vibration frequencies and corresponding vibration modes are obtained. The vibration mode of a solid represents the typical final configuration charactering how the solid vibrates when excited with the corresponding vibration frequency. Therefore, as already mentioned in Section 3, the vector representing the $i$th vibration mode is defined as $\varphi_i$. Notice that $\varphi_i$ is the $[2N \times 1]$ array defining the typical final configuration characterizing how the solid vibrates when excited with the $i$th vibration frequency (recall that $N$ is the total number of nodes discretizing the problem domain). In order to perform a cross-comparison, the following expression is applied to each node discretizing the problem domain. For instances, for node $\boldsymbol{x}_j$:

$$\xi(\boldsymbol{x}_j)_i^{a/b} = \frac{\phi(\boldsymbol{x}_j)_i^a - \phi(\boldsymbol{x}_j)_i^b}{\phi(\boldsymbol{x}_j)_i^b} \tag{29}$$

being $a$ a numerical formulation (for example, FEM) and $b$ another numerical formulation (for example, NNRPIMv1). In the end, a new distribution map representing the relative differences between technique $a$ and $b$, will be obtained, $\xi(\boldsymbol{x})_i^{a/b}$, for each $i$th vibration frequency.

In the end, after obtaining all the three $\xi(\boldsymbol{x})_1^{a/b}$, $\xi(\boldsymbol{x})_2^{a/b}$ and $\xi(\boldsymbol{x})_3^{a/b}$ distributing maps (corresponding to the first, second and third vibration frequencies, respectively), a global average difference between techniques $a$ and $b$ was calculated:

$$\bar{\xi}_i^{a/b} = \frac{1}{N} \sum_{j=1}^{N} \xi(\boldsymbol{x}_j)_i^{a/b} \tag{30}$$

The same technique was applied to the 3D analysis. Thus, once again, the first three vibration modes obtained in Section 5.5 with the FEM and NNRPIM formulations, using mesh M4, were used to perform the comparisons.

Following this technique, several difference distribution maps $\xi(\boldsymbol{x})_i^{a/b}$ were obtained and several average differences $\bar{\xi}_i^{a/b}$ were calculated.

Fig. 11 shows the difference distribution maps, $\xi(\boldsymbol{x})_i^{a/b}$, and corresponding average differences, $\bar{\xi}_i^{a/b}$, obtained for the three first vibration modes of the 2D and 3D cupula with the FEM and NNRPIM analysis using the mesh M4. In Fig. 11 only differences below 10% are shown. This will allow to understand clearly the extent of domain in which the differences are higher than 10%.

In the 2D analysis, it is possible to visualize that the FEM and the NNRPIMv1 formulation allow to obtain close results. Alternatively, the NNRPIMv2 solution presents higher differences when compared with the FEM solutions. However, the NNRPIMv1 and the NNRPIMv2 produce very close results.

Notice that the NNRPIMv1 formulation only uses first degree influence cells. Therefore, commonly, each influence cell is formed with 3–9 nodes. On the other hand, the NNRPIMv2 uses the second degree influence cells, which means that each influence cell could be formed with 9–27 nodes (commonly). Regarding the FEM, the quadratic element used in the 2D analysis possesses 4 nodes in each element. As it is possible to understand, the quadratic element formulation is much closer to the NNRPIMv1 formulation than to the NNRPIMv2 formulation. Thus, it is natural that the difference between the FEM solution

and the NNRPIMv1 solution is smaller than the difference between the FEM and the NNRPIMv2. These results do not conclude about the best numerical formulation, they only permit to understand the magnitude of their differences.

The same observations can be found for the 3D analysis. Nevertheless, in the 3D analysis the difference between the formulations are much higher. For the 3D analyses, only the comparison between the NNRPIMv2 and NNRPIMv1 allows to obtain global average differences below 10%. Once again, the differences between the NNRPIMv1 and the FEM solutions are smaller than the ones found between the NNRPIMv2 and the FEM results.

Another relevant observation from Fig. 11 is the fact that differences for the first vibration mode are higher in almost cases comparing with the differences found for the second and third vibration modes.

## 6. Conclusion

In this work, the FEM and the NNRPIM were used to analyze numerically the dynamic response of the cupula. The results show that both techniques are capable to achieve similar results. However, most importantly, this work opens a new research branch in the computational analysis of the vestibular system.

As Table 1 shows, for the 2D analysis, the FEM and NNRPIMv1 formulations possess a solid convergence. The values obtained for the less discretized mesh (M1) are monotonically evolving to the ones obtained with the most discretized mesh (M4). On the other hand, the NNRPIMv2 formulation appears to achieve the convergence extremely soon. Notice that for M2 the solution has already converged, being the results obtained with M2, M3 and M4 almost identical.

Concerning the results of the 3D analysis, both the NNRPIM formulations present high convergence rates (Table 2). The solution obtained for meshes M2, M3 and M4 is almost identical. In opposition, the FEM appears to present lower convergence rates. This can be explained with the kind of element used in the finite element analysis—tetrahedral element, which possesses a low convergence rate.

Furthermore, the final converged results are all very close, regardless the used numerical formulation. The 2D results indicate that first vibration frequency is between 51.71 Hz and 53.43 Hz for the 2D analysis. Additionally, the 3D results for the same vibration mode (which in 3D is the second vibration mode) indicate a similar vibration frequency between 51.91 Hz and 56.14 Hz. Furthermore, if only the NNRPIMv2 results are considered, the resemblance is much closer: 51.71 Hz (2D) and 51.91 Hz (3D).

The results from Tables 1 and 2 show that the target vibration frequency of the cupula (corresponding the first vibration mode in 2D and the second vibration mode in 3D) present a very distinct value (around 52–56 Hz) when compared with the vibration frequencies of other vibration modes. This is an advantage, it means that it will be possible to easily identify the target vibration frequency of the cupula.

The dynamic response of a structure strongly depends on its geometric shape, material properties and environment, as confirmed by the results obtained in this work. The response of the cupula when it is surrounded by endolymph (and also with attached otoconia particles) present different natural frequencies, as Fig. 8 shows. Nevertheless, the first vibration frequencies are between 59.47 Hz and 61.43 Hz. These magnitudes are close to the ones obtained without the surrounding endolymph (51.71 Hz and 53.43 Hz).

This result is relevant. It means that a simulation in which the surrounding endolymph is disregard will allow to obtain a satisfactory approximated solution.

Another very important conclusion concerns the inclusion (or not) of otoconia in the model. As Fig. 9 shows, it was found that the inclusion of otoconia do not modify (significantly) the vibration frequency of the cupula. Notice that the first vibration frequency of the cupula with surrounding endolymph and without otoconia is between 59.47 Hz and 61.43 Hz (Fig. 8) and the same first vibration frequency of the cupula

78

with surrounding endolymph and with otoconia is between 60.32 Hz and 63.90 Hz (Fig. 9-1 otoconia); 61.45 Hz and 63.07 Hz (Fig. 9-2 otoconia); and 61.80 Hz and 63.85 Hz (Fig. 9-3 otoconia).

In this work, the distinct formulations are directly compared by means of a computational cost study and a cross-comparison study. It was found that the FEM formulation presents a slightly lower computational cost when compared with the NNRPIM formulations. However, notice that the NNRPIMv2 formulation converges very fast. Actually, in 2D, for mesh M2, the NNRPIMv2 formulation is already capable to produce results very close with its final converged solution (M4). On the other hand, the FEM presents a more slow convergence rate. Thus, comparing the computational cost of a 2D analysis using NNRPIMv2 and mesh M2 and the computational cost of a 2D analysis using FEM and mesh M4, it is visible that FEM will present a higher computational cost.

Regarding the cross-comparison study, it was possible to observe that both NNRPIM formulations allow to obtain very similar results, regardless the spatial dimension of the analysis (2D or 3D). Additionally, it was found that the FEM solution is closer with the NNRPIMv1 solutions rather the NNRPIMv2 solution. This observation (more evident in the 2D analysis) can be explained with the number of nodes used to construct the shape functions.

Since one particular case of BPPV is cupulolithiasis, (the attachment of otoconia to the cupula), this research work will allow in the future some new therapeutic solutions based on the induction of the cupula vibration by means of a sound source. With this work, it was possible to understand that the natural frequency of the cupula ranges between 51 Hz or 61 Hz and all the other vibration frequencies possess very distinct values. Since theoretically, the resonance phenomena will force the cupula to vibrate, the induced vibration will allow to detach the otoconia particles from the cupula, reducing the vertigo symptoms. This could be achieve with non-invasive way, such as listening to music with a predominant set of bass sounds.

## Acknowledgments

## References

[1] Jaeger R, Takagi A, Haslwanter T. Modeling the relation between head orientations and otolith responses in humans. Hear. Res. Nov. 2002;173(1–2):29–42.

[2] Duncan RK, Grant JW. A finite-element model of inner ear hair bundle micromechanics. Hear. Res. Feb. 1997;104(1–2):15–26.

[3] Grieser B, Obrist D. "Validation of assumptions on the endolymph motion inside the semicircular canals of the inner ear," Internal reports of the Institute of Fluid Dynamics. ETH Zurich, pp. 1–16, 2012.

[4] Kassemi M, Deserranno D, Oas JG. Fluid–structural interactions in the inner ear. Comput. Struct. Jan. 2005;83(2–3):181–9.

[5] Kondrachuk A. Finite element modeling of the 3D otolith structure. J. Vestib. Res. Jan. 2001;11(1):13–32.

[6] Liu G-R, Quek SS. The finite element method : a practical course. 2nd ed. Butterworth-Heinemann; 2013.

[7] Nguyen VP, Rabczuk T, Bordas S, Duflot M. Meshless methods: a review and computer implementation aspects. Math. Comput. Simul. Dec. 2008;79(3):763–813.

[8] Belytschko PKT, Krongauz Y, Organ D, Fleming M. Meshless methods: an overview and recent developments. Comput. Methods Appl. Mech. Eng. Dec. 1996;139(1–4):3–47.

[9] Gu YT. Meshfree methods and their comparisons. Int. J. Comput. Methods Dec. 2005;2(4):477–515.

[10] Belinha J. Meshless methods in biomechanics—bone tissue remodelling analysis. Tavares JMRS, Natal Jorge RM, editors. Switzerland: Springer International Publishing; 2014.

[11] Belinha J, Araújo AL, Ferreira AJM, Dinis LMJS, Natal Jorge RM. The analysis of laminated plates using distinct advanced discretization meshless techniques. Compos. Struct. May 2016;143:165–79.

[12] Dinis LMJS, Natal Jorge R, Belinha J. Analysis of 3D solids using the natural neighbour radial point interpolation method. Comput. Methods Appl. Mech. Eng. Mar. 2007;196(13–16):2009–28.

[13] Belinha J, Dinis LMJS, Natal Jorge RM. The natural radial element method. Int. J. Numer. Methods Eng. Mar. 2013;93(12):1286–313.

[14] Sukumar N, Moran B, Belytschko T. The natural element method in solid mechanics. Int. J. Numer. Methods Eng. Nov. 1998;43(5):839–87.

[15] Sukumar N, Moran B, Yu Semenov A, Belikov VV. Natural neighbour Galerkin methods. Int. J. Numer. Methods Eng. Jan. 2001;50(1):1–27.

[16] Ferreira AJM. A formulation of the multiquadric radial basis function method for the analysis of laminated composite plates. Compos. Struct. Feb. 2003;59(3):385–92.

[17] Doblaré M, Cueto E, Calvo B, Martínez MA, Garcia JM, Cegoñino J. On the employ of meshless methods in biomechanics. Comput. Methods Appl. Mech. Eng. Feb. 2005;194(6–8):801–21.

[18] Wong KCL, Wang L, Zhang H, Liu H, Shi P. Meshfree implementation of individualized active cardiac dynamics. Comput. Med. Imaging Graph. Jan. 2010;34(1):91–103.

[19] Chen G, et al. A new approach for assigning bone material properties from CT images into finite element models. J. Biomech. Mar. 2010;43(5):1011–15.

[20] Do T, Khosravifard A, Hematiyan MR, Bui TQ. Accurate and efficient analysis of stationary and propagating crack problems by meshless methods. Theor. Appl. Fract. Mech. Feb. 2017;87:21–34.

[21] Bui TQ, Vu T-V, Nguyen N-H, Khosravifard A, Hematiyan MR, Tanaka S. A simple FSDT-based meshfree method for analysis of functionally graded plates. Eng. Anal. Bound. Elem. Jun. 2017;79:1–12.

[22] Bui TQ, Nguyen MN, Zhang C, Pham DAK. An efficient meshfree method for analysis of two-dimensional piezoelectric structures. Smart Mater. Struct. Jun. 2011;20(6):65016.

[23] Bui TQ, Tanaka S, Suzuki H, Sadamoto S, Imachi M. Analysis of cracked shear deformable plates by an effective meshfree plate formulation. Eng. Fract. Mech. Aug. 2015;144:142–57.

[24] Zhang C, Bui TQ, Nguyen MN. Buckling analysis of Reissner–Mindlin plates subjected to in-plane edge loads using a shear-locking-free and meshfree method. Eng. Anal. Bound. Elem. Sep. 2011;35(9):1038–53.

[25] Sadamoto S, Ozdemir M, Tanaka S, Taniguchi K, Yu TT, Bui TQ. An effective meshfree reproducing kernel method for buckling analysis of cylindrical shells with and without cutouts. Comput. Mech. Jun. 2017;59(6):919–32.

[26] Yanagihara D, Sadamoto S, Tanaka S, Taniguchi K, Ozdemir M, Bui TQ, Murakami C. Buckling analysis of stiffened plate structures by an improved meshfree flat shell formulation. Thin Walled Struct. Aug. 2017;117:303–13.

[27] Nguyen MN, Bui TQ. A moving Kriging interpolation-based meshfree method for free vibration analysis of Kirchhoff plates. Comput. Struct. Feb. 2011;89(3–4):380–94.

[28] Bui TQ, Nguyen MN, Zhang C. An efficient meshfree method for vibration analysis of laminated composite plates. Comput. Mech. Aug. 2011;48(2):175–93.

[29] Zhang C, Bui TQ, Nguyen MN. A meshfree model without shear-locking for free vibration analysis of first-order shear deformable plates. Eng. Struct. Dec. 2011;33(12):3364–80.

[30] Golub M, Bui TQ, Khosravifard A, Zhang C, Hematiyan MR. Dynamic analysis of sandwich beams with functionally graded core using a truly meshfree radial point interpolation method. Eng. Struct. Feb. 2013;47:90–104.

[31] ElZahab AJKZ, Divo E. A localized collocation meshless method (LCMM) for incompressible flows CFD modeling with applications to transient hemodynamics. Eng. Anal. Bound. Elem. Aug. 2009;33(8–9):1045–61.

[32] Ho AK, Tsou L, Green S, Fels S. A 3D swallowing simulation using smoothed particle hydrodynamics. Comput. Methods Biomech. Biomed. Eng. Imaging Vis. Oct. 2014;2(4):237–44.

[33] Gámiz MJ, Lopez-Escamez JA. Health-related quality of life in patients over sixty years old with benign paroxysmal positional vertigo. Gerontology Feb. 2004;50(2):82–6.

[34] Santos CF, Belinha J, Gentil F, Parente M, Jorge RN. An alternative 3D numerical method to study the biomechanical behaviour of the human inner ear semicircular canal. Acta Bioeng. Biomech. 2017;19(1):3–15.

[35] Dinis LMJS, Natal Jorge RM, Belinha J. A natural neighbour meshless method with a 3D shell-like approach in the dynamic analysis of thin 3D structures. Thin Walled Struct Jan. 2011;49(1):185–96.

[36] Sibson R. A brief description of natural neighbor interpolation, vol. 4. Chichester, New York: Wiley; 1981.

[37] Sibson R. A vector identity for the Dirichlet tessellation. Math. Proc. Camb. Phil. Soc. 1980;87:151–5.

[38] Voronoi GM. Nouvelles applications des paramè'tres continus a' la the´orie des formes quadratiques. Deuxiè'me Me´moire: Recherches sur les paralle´lloe'dres primitifs. Reine Angew. Math 1908;134:198–287.

[39] Delaunay B. Sur la sphe´re vide. A la memoire de Georges Voronoı. Izv. Akad. Nauk SSSR, Otd. Mat. i Estestv. Nauk. 1934(6):793–800.

[40] Belytschko T, Lu YY, Gu L. Element-free Galerkin methods. Int. J. Numer. Methods Eng. Jan. 1994;37(2):229–56.

[41] Liu WK, Jun S, Li S, Adee J, Belytschko T. Reproducing kernel particle methods for structural dynamics. Int. J. Numer. Methods Eng. May 1995;38(10):1655–79.

79

[42] Atluri SN, Zhu T. A new meshless local Petrov–Galerkin (MLPG) approach in computational mechanics. Comput. Mech. Aug. 1998;22(2):117–27.

[43] Liu GR, Gu YT. A point interpolation method for two-dimensional solids. Int. J. Numer. Methods Eng. Feb. 2001;50(4):937–51.

[44] Li Y, Dai KY, Liu GR, Han X. Inelastic analysis of 2D solids using a weak–form RPIM based on deformation theory. Comput. Methods Appl. Mech. Eng. Jul. 2006;195(33–36):4179–93.

[45] Hematiyan MR, Khosravifard A, Bui TQ. Efficient evaluation of weakly/strongly singular domain integrals in the BEM using a singular nodal integration method. Eng. Anal. Bound. Elem. Apr. 2013;37(4):691–8.

[46] Racz D, Bui TQ. Novel adaptive meshfree integration techniques in meshless methods. Int. J. Numer. Methods Eng. Jun. 2012;90(11):1414–34.

[47] Tanaka S, Suzuki H, Sadamoto S, Sannomaru S, Yu T, Bui TQ. J-integral evaluation for 2D mixed-mode crack problems employing a meshfree stabilized conforming nodal integration method. Comput. Mech. Aug. 2016;58(2):185–98.

[48] Wang JG, Liu GR. A point interpolation meshless method based on radial basis functions. Int. J. Numer. Methods Eng. Aug. 2002;54(11):1623–48.

[49] Liu GR, Wang JG. On the optimal shape parameters of radial basis functions used for 2-D meshless methods. Comput. Methods Appl. Mech. Eng. Mar. 2002;191(23–24):2611–30.

[50] Hardy RL. Theory and applications of the multiquadric-biharmonic method 20 years of discovery 1968–1988. Comput. Math. Appl. Jan. 1990;19(8–9):163–208.

[51] Bowman H, Golberg MA, Chen CS. Some recent results and proposals for the use of radial basis functions in the BEM. Eng. Anal. Bound. Elem. Apr. 1999;23(4):285–96.

[52] Bathe K-J. Finite element procedures. 2nd ed. Englewood Cliffs: Prentice-Hall; 1996.

[53] Winter DA. Human balance and posture control during standing and walking. Gait & Posture 1995;3(4):193–214.

[54] Diener HC, Dichgans J. On the role of vestibular, visual and somatosensory information for dynamic postural control in humans. Prog. Brain Res. 1988;76:253–62.

[55] Taylor J, Goodkin HP. Dizziness and vertigo in the adolescent. Otolaryngol. Clin. North Am. Apr. 2011;44(2):309–21 vii–viii.

[56] Karatas M. Central vertigo and dizziness. Neurologist Nov. 2008;14(6):355–64.

[57] Squires TM, Weidman MS, Hain TC, Stone HA. A mathematical model for top-shelf vertigo: the role of sedimenting otoconia in BPPV. J. Biomech. Aug. 2004;37(8):1137–46.

[58] Davis JL, Xue J, Peterson EH, Grant JW. Layer thickness and curvature effects on otoconial membrane deformation in the utricle of the red-ear slider turtle: static and modal analysis. J. Vestib. Res. 2007;17(4):145–62.

80

## 2.6. Highlights of Contribution V

This contribution focused on evaluating the free vibration analysis of the cupula extending for the first time one of the most popular meshless methods (RPIM) to the biomechanical analysis of a vestibular disorder.

Therefore, the main contents of this publication include:

I.      Brief description of meshless methods with a detailed formulation for the RPIM;

II.     Free vibration analysis of the cupula using RPIM including FEM comparison, with two models (2D and 3D), and also using four different meshes discretization for each model;

III.    Acquisition of the natural frequencies of the cupula using FEM and RPIM methodologies:

The three first vibration modes and natural frequencies of the three dimensional cupula using the FEM and RPIM, using the constant polynomial basis formulation, are presented in Figure 1.10 using the mesh M2, with 3156 tetrahedral elements.
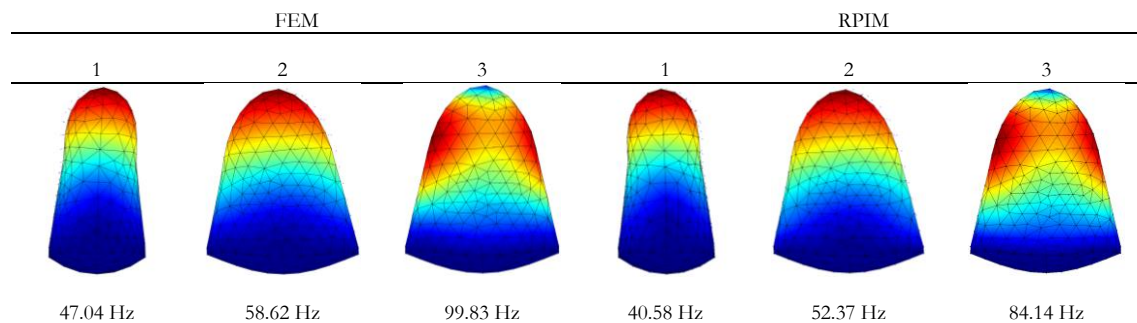


| FEM | | | RPIM | | |
|---|---|---|---|---|---|
| 1 | 2 | 3 | 1 | 2 | 3 |
| 47.04 Hz | 58.62 Hz | 99.83 Hz | 40.58 Hz | 52.37 Hz | 84.14 Hz |

**Figure 1.10** – Three first modes and natural frequencies of the three-dimensional cupula with FEM and RPIM using the mesh M2; front and side view.

The three dimensional dynamic response analysis of the cupula allows for a more realistically understanding of the overall behavior of the cupula. Moreover, the results shown that the natural frequencies of the second vibration mode in the 3D model are very close to the natural frequencies obtained with the first vibration mode in the 2D model with both formulations.

IV.     A convergence study with both methodologies was performed:

The results of the 3D convergence study of the isolated cupula are shown in Figure 1.11. These values are obtained for the natural frequency 2 for FEM and the three RPIM formulations using

distinct polynomial basis: the constant polynomial basis is the 'RPIM 1', the linear polynomial basis is the 'RPIM 2', and the quadratic polynomial basis is the 'RPIM 3'.
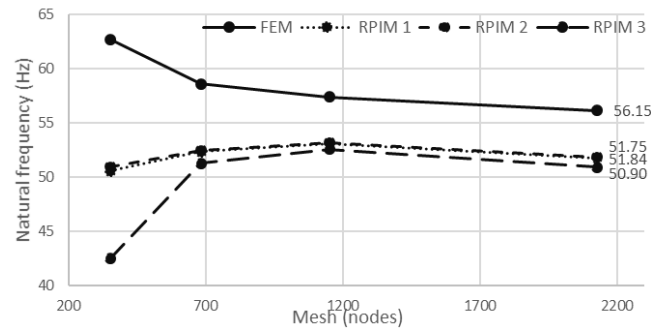


**Figure 1.11** – Convergence FEM and RPIM different polynomial basis for 3D model - natural frequency 2.

The results show that solutions from both methodologies are close and the results converged, as expected, as the mesh density increased. A similar behavior occurs for the two-dimensional cupula model and, also, the natural frequency 1.

V. Simulate the cupula environment in the vestibular system with the endolymph in order to evaluate their influence in the natural frequencies values of cupula;

VI. Consider the influence of the otoconia attached to the cupula, in order to obtain the natural frequencies of the pathological scenario of cupulolithiasis:

The cupulolithiasis cases considered in the present manuscript were three different sizes of otoconia particles, placed above and laterally to the cupula, as shown in Figure 1.12.
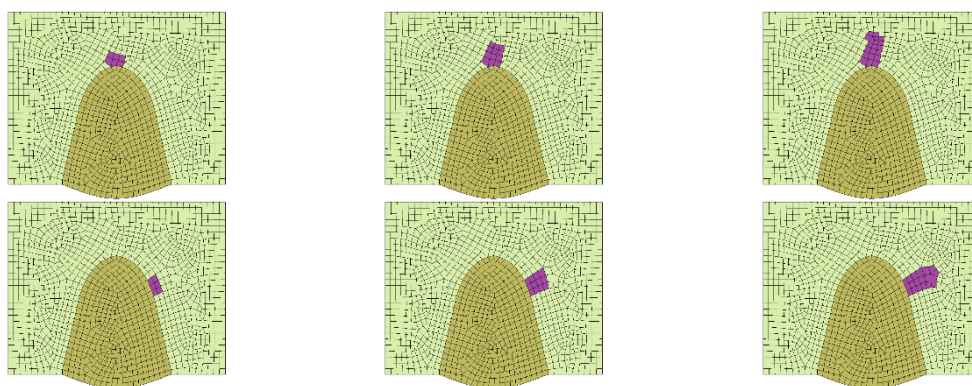


**Figure 1.12** – Two dimensional cupula model surrounded with endolymph and otoconia.

The results presented for the cupulolithiasis cases show, mainly in the study with the medium and large otoconia and with the RPIM formulation, that higher potential displacements occur in the side of the cupula side where the otoconia are placed. This indicates that RPIM is capable of

accurately capture the vibration mode of the structure and that the size of the otoconia influences the vibration mode of the cupula.

VII. Closing remarks about the effectiveness of the used numerical methodologies and obtained natural frequency values.

The complete document can be found in the next sub-chapter.

## 2.6.1.  Contribution V

**<u>Analyses of Free Vibrations of the Cupula in the Human
Vestibular System during Cupulolithiasis: a Meshless approach</u>**

# Analyses of Free Vibrations of the Cupula in the Human Vestibular System during Cupulolithiasis: a Meshless approach

Carla F. Santos [a], J. Belinha [a,b], Fernanda Gentil[c], Marco Parente [a,d] and Renato Natal Jorge [a,d]

a INEGI, Institute of Mechanical Engineering and Industrial Management, Rua Dr. Roberto Frias, Porto, Portugal.
b School of Engineering, Polytechnic of Porto, (ISEP), Porto, Portugal
c Clínica ORL-Dr. Eurico Almeida, Widex, Escola Superior de Saúde – I.P.Porto, Porto,Portugal
d FEUP, Faculty of Engineering of the University of Porto, Rua Dr. Roberto Frias, Porto, Portugal.

**Abstract**

The inner ear is one of the most important sensorial structures in the human body, allowing to maintain the balance by sensing movements and accelerations. One of the micro-structures responsible for such subtle task is the cupula, a gelatinous structure surrounded by endolymph and localized inside the semicircular canals.

The main focus of this work is to understand how the cupula vibrates. Thus, a free vibration analysis of this micro-structure is performed using an advanced discretization meshless technique. Hence, two-dimensional and three-dimensional geometric models of the cupula were built and then discretized. The models were analysed using the Radial Point Interpolation Method (RPIM) - a popular and accurate meshless method – and all the obtained results are compared with the Finite Element Method (FEM) solutions. Several scenarios were studied, aiming to analyze the environment of the cupula in healthy and pathologic states.

The results show that the RPIM is a reliable, efficient and robust numerical technique, delivering results very close with the ones obtained with the FEM and showing a higher convergence rate. Regardless the dimensional analysis (2D or 3D) or the discretization technique used (RPIM or FEM), it was found the natural frequency of the cupula is always between 51.75 Hz and 56.14 Hz. These narrow that it is possible to induce the resonance of the cupula by a sound source, which will allow to solve cupulolithiasis – a disorder causing severe dizziness.

# 1.Introduction

Vestibular system is a microscopic part of the inner ear in charge of the balance function of the human body. Commonly, dizziness is a symptom revealing its failure. The most common disorder associated with this kind of symptoms is benign paroxysmal positional vertigo (BPPV), which occurs mainly in elders. It affects about 1.6% of the population each year [1]. Additionally, a study reported a cost of 2.000 US dollars per individual in BPPV inappropriate diagnostic procedures and ineffective therapies [2]. Cupulolithiasis is a particular case of BPPV that will be analysed in the present work.

Mathematical models have been developed through the years to study parts of the vestibular system [3]–[7].

It is possible to study the biomechanics of such biological structure with discrete numerical methods. Nowadays, the most popular numerical method is the finite element method (FEM)[8], mainly its linear formulation, which assume the triangle and quadrilaterals shapes for 2D analyses and tetrahedron and hexahedron shapes for 3D.

Presently, using the computed axial tomography (CAT) imaging technique, it is possible to construct realistic and accurate discrete geometrical models.

However, there are some disadvantages in the finite element technique. Being a mesh dependent numerical method, the FEM requires well balanced meshes. For instances, it is computational challenging to efficiently discretize highly irregular domains (as the biological structures) with uniform and high quality meshes. This process represents a high computational cost. Additionally, the mesh refinement requirement in large deformation problems is also computationally heavy.

In the last decades, the computational mechanics community has been developing other discrete numerical techniques, such as meshless methods [9]. These methodologies are competitive and alternative advanced discretization techniques capable to obtain efficiently the solution of several fundamental problems [10].

The discretization step is the main difference between meshless methods and FEM: meshless methods discretize the domain using just an unstructured cloud of nodes [9]–[13] and FEM discretizes the problem domain with a rigid element mesh.

In meshless' seminal works, surface fitting or the solution of the partial differential equations (PDE) were the main focus [10]. Today, these techniques are used to solve a wide-range of linear and non-linear numerical problems [10] [12].

Meshless methods comprise several similar advanced discretization techniques [12]. Thus, several categorizations are possible for meshless methods [10] [12]. One of the main labels for meshless

methods is the categorization into approximating meshless methods or interpolating meshless methods [12].

Approximating meshless methods construct their shape functions using approximation functions. Their main disadvantage is the lack of the delta Kronecker property, which hinders the imposition of essential and natural boundary conditions [12]. Interpolating meshless methods are capable to construct shape functions possessing the Kronecker delta property (as the ones produced with the FEM). In this case, it is possible to impose the essential and natural boundary conditions using the same FEM techniques [12]. In the literature it is possible to find research works comparing both meshless approaches [9]–[13]. Generally, approximating meshless methods are capable to deliver smoother and accurate results. However, interpolating meshless methods allow to easily impose essential and natural boundary conditions, easing the computational effort.

In biomechanics meshless methods are particularly attractive. The complex geometry of the bio-structure can be obtained directly from a medical imaging (CAT scan or the MRI images), associating the nodal position with the voxel position.

The most attractive feature of meshless methods it their capability to discretize the problem domain using directly the pixels (or voxels) spatial information from CAT scans or MRI images [12], [14]–[18]. Furthermore, using the grey scale of medical images, meshless methods are capable to identify several biological structures and then attribute to each node the corresponding material properties [12].

The literature shows that meshless methods have clear advantages over other numerical techniques and are a reliable option in biomechanics computational applications [19], mainly using medical imaging techniques (CAT scan and MRI) [20], [21]. Moreover, the remeshing efficiency is one of the advantages of meshless methods over FEM, which could be relevant in the structural analysis biological models [22], [23], as the recent Smoothed Particle Hydrodynamics (SPH) applications have demonstrated [24], [25].

In this work, for the first time, the 2D/3D structural analysis of the cupula of the vestibular system is performed. Thus, the free-vibration analysis of the cupula is performed assuming both the FEM and an interpolating meshless method – the Radial Point Interpolation Method (RPIM) [12], [26].

This manuscript is organized as follows. In section 2 the RPIM formulation is described with detail. Then, in section 3, the system of equations and the corresponding matrix formulation are presented. In section 4, the 2D/3D numerical models of the cupula are presented and in section 5 the obtained results are shown and discussed. The manuscript ends with section 6 in which the main conclusions and final remarks are presented.

# 2. Meshless Method

The meshless method applied in this work is the RPIM [12], [27], [28]. The RPIM is an interpolator meshless method which enforces nodal connectivity using the influence-domain concept. To solve the integro-differential equations governing the physical phenomenon, the RPIM uses a background cloud of integration points, constructed using integration cells and the Gauss-Legendre quadrature rule.

## 2.1. Nodal Connectivity and Numerical Integration

Several meshless methods use the concept of influence domain due to its simplicity. As FEM, meshless methods are discrete numerical methods. However, instead of discretizing the problem domain in elements and nodes, meshless methods discretize the problem domain using just nodes. The nodal connectivity in FEM is predefined by a finite element mesh defined in the pre-processing phase. Thus, the nodes of each element interact directly with each other and the nodes belonging to the element boundary interact with the nodes of neighbour finite elements.

In meshless methods, after the nodal discretization, the nodal connectivity is established with the "influence-domain" concept. The nodal connectivity in meshless methods is not a pre-established information (as in FEM) and it is assured by the overlap of the influence-domains [12]. Since this technique is very simple to implement, it has been used to support the development of several meshless techniques [9], [12], [27], [29]–[31]. Generally, the influence-domains are obtained by searching radially enough nodes inside a defined area (2D problems) or a defined volume (3D problems). Nevertheless, it has been observed that the size or shape variation of these influence-domains affects the performance of the meshless method along the problem domain [12]. Thus, regardless the used meshless technique, the literature proposes that each 2D influence-domain should possess approximately n = [9, 16] nodes [9], [12], [27], [29]–[31]. In Figure 1(a) is presented an example of an influence domain of an interest point $x_I$ (which could be a node or an integration point). In this work, for the 2D analysis each influence domain contains 16 nodes. For all 3D analyses, each influence domain contains 27 nodes.

In order to solve the integro-differential equations governing the discrete numerical methods - the Galerkin weak formulation - a background integration mesh is required. This numerical integration process represents a significant percentage of the total computational cost of the analysis.

In the FEM, the construction of the integration mesh is simplified by the existence of the element mesh, since each element is geometrically coincident with each integration cell. Additionally, the

FEM shape functions are known polynomial functions. Therefore, accurate well-known relations [32], [33] can be used to predefine the number of integration points per each integration cell.

In the case of meshless methods, the accurate definition of the background integration mesh is a more challenging task. In meshless methods it is not possible to accurately define a priori the background integration mesh because the shape function degree is generally unknown. In this work it is used the numerical integration scheme suggested in previous RPIM works [27], [28]. Generally, in the RPIM formulation, as Figure 1 (b) represents, the entire domain is divided in a regular grid creating quadrilateral integration cells and then, respecting the Gauss-Legendre quadrature rule [12] (Figure 1), each cell is filled with integration points.

In this work, since every analysis is performed using the FEM and the RPIM, for the 2D analyses, the background integration cell lattice is assumed coincident with the FEM mesh. Then, inside each quadrilateral 3x3 Gauss points are inserted, as Figure 1 (b) shows. For the 3D analyses, since the 3D FEM meshes are built with tetrahedrons, inside each tetrahedron is considered one integration point, whose spatial position is coincident with the volume centre of the tetrahedron and whose integration weight is coincident with the tetrahedron volume. The literature shows that both these integration schemes allow to integrate accurately the Galerkin weak form [12].
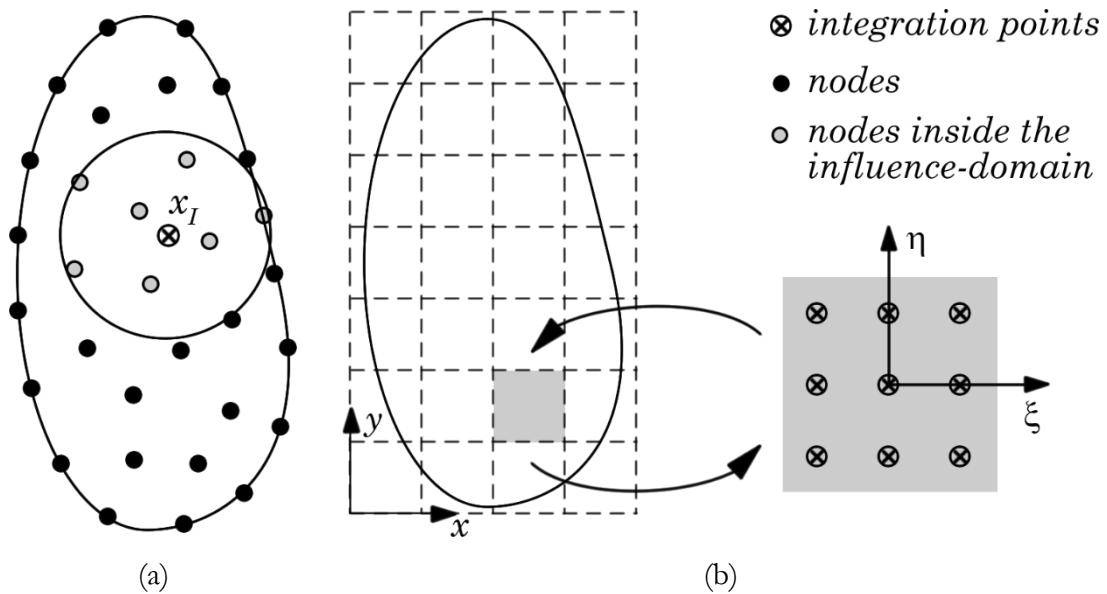


**Figure 1**. (a) Influence domain generic representation. (b) background integration cells and corresponding Gauss-Legendre integration scheme.

## 2.2. Radial Point Interpolators

Radial Point Interpolators (RPI) are used to obtain the RPIM shape functions, combining radial and polynomial basis functions. Thus, consider a function space $T$ defined in the domain $\Omega$. The

finite dimensional space $T_h \subset T$ discretises the domain $\Omega$ and it is defined by: $T_h :=$ $\langle r(x - x_i) : i \in \mathbb{N} \wedge i \leq N \rangle + p_m(x)$, where $r : \mathbb{R}^d \mapsto \mathbb{R}$ is at least a $C^{-1}$ function and $p_m : \mathbb{R}^d \mapsto \mathbb{R}$ is defined in the space of polynomials of degree less than $m$. In this section only simplified two-dimensional domains $\Omega \subset \mathbb{R}^2$ are shown. Therefore, it is consider an interpolation function $u^h(x)$ defined in an influence-domain $\Omega_I \subset \Omega$ of an interest point $x_I \in \mathbb{R}^2$ and discretized by a set of nodes: $X_I = \{ x_1, x_2, \dots, x_n \} \wedge x_i \in \mathbb{R}^2$, being $n$ the number of nodes inside the influence-domain of $x_I$. Notice that the domain $\Omega \subset \mathbb{R}^2$ is discretised by a nodal set defined by $X = \{ x_1, x_2, \dots, x_N \} \wedge x_i \in \mathbb{R}^2$. The density of $X$ is identified by $h$,

$$h = min\|x_j - x_i\|, \forall\{i,j\} \in \mathbb{N} : \{i,j\} \leq N \wedge i \neq j \tag{1}$$

Being $\| . \|$ the Euclidean norm.

The RPI constructs an interpolation function $u^h(x) \in T$ capable to pass through all nodes within the influence-domain, meaning that since the nodal function value is assumed to be $u_i$ at the node $x_i$, $u_i = u(x_i)$, consequently, $u^h(x_i) = u(x_i)$. Using a radial basis function $r(x)$ and a polynomial basis function $p(x)$, the interpolation function $u^h(x) \in T$ can be defined at the interest point $x_I \in \mathbb{R}^d$ (not necessarily coincident with any $x_i \in X$) by,

$$u^h(x_I) = \sum_{i=1}^{n} r_i(x_I) a_i + \sum_{j=1}^{m} p_j(x_I) b_j = r(x_I)^T a + p(x_I)^T b = u(x_I) \tag{2}$$

where $a_i$ and $b_j$ are the non-constant coefficient of $r_i(x_I)$ and $p_j(x_I)$ respectively. The integer $n$ is the number of nodes inside the influence-domain of the interest point $x_I$. The vectors are defined as,

$$a^T = \{a_1, a_2, \dots, a_n\} \tag{3}$$

$$b^T = \{b_1, b_2, \dots, b_m\} \tag{4}$$

$$r(x)^T = \{r_1(x), r_2(x), \dots, r_n(x)\} \tag{5}$$

$$p(x)^T = \{p_1(x), p_2(x), \dots, p_m(x)\} \tag{6}$$

Being $x_i = \{x_i, y_i\}$. This work uses the Multiquadrics Radial Basis Function (MQ-RBF) [12], [27], [28], which can be defined as $r_i(x_I) = s(d_{iI}) = (d_{iI}^2 + c^2)^p$ , where $d_{iI}$ is the distance between the interest point $x_I = \{x_I, y_I\}$ and the node $x_i = \{x_i, y_i\}$, being $d_{iI} = \sqrt{(x_i - x_I)^2 + (y_i - y_I)^2}$. The $c$ and $p$ variables are the MQ-RBF shape parameters, which are fixed values determined in previous works [27], [28]. The variation of these parameters can affect the performance of the MQ-RBFs. In the work of Wang and Liu [27] [28] it was shown that the optimal values are $c = 1.42$ and $p = 1.03$, which are the values used in this work. The original

RPI formulation requires a complete polynomial basis function. For the two-dimensional space the following constant, linear and quadratic polynomial basis can be defined, respectively, as,

$$p(x_i)^T = \{1\}, \qquad m = 1 \tag{7}$$
$$p(x_i)^T = \{1, x_i, y_i\}, \; m = 3$$
$$p(x_i)^T = \{1, x_i, y_i, x_i^2, x_i y_i, y_i^2\}, \; m = 6$$

Nevertheless, it was shown in previous RPI research works [12], [14], [34] that using a constant basis increases the RPI formulation efficiency.

The coefficients $a_i$ and $b_j$ in equation (1) are determined by enforcing the interpolation to pass through all $n$ nodes within the influence-domain [12]. The interpolation at the $k^{th}$ node is defined by,

$$u^h(x_k, y_k) = \sum_{i=1}^{n} r_i(x_k, y_k) a_i + \sum_{i=1}^{m} p_j(x_k, y_k) b_j = u_k, \quad k = 1,2,\dots,n \tag{8}$$

The inclusion of the following polynomial term is an extra-requirement that guarantees unique approximation [12], [34],

$$\sum_{i=1}^{n} p_j(x_i, y_i) a_i = 0, \quad j = 1,2,\dots,m \tag{9}$$

The computation of the shape functions is written in a matrix form as

$$\begin{bmatrix} R & P \\ P^T & Z \end{bmatrix} \begin{Bmatrix} a \\ b \end{Bmatrix} = \begin{Bmatrix} u \\ z \end{Bmatrix} \Leftrightarrow G \begin{Bmatrix} a \\ b \end{Bmatrix} = \begin{Bmatrix} u \\ z \end{Bmatrix} \tag{10}$$

where $G$ is the complete moment matrix, $Z$ is a null matrix defined by $Z_{ij} = 0, \forall \{\{i,j\} \in \mathbb{N}: \{i,j\} \le m\}$ and the null vector $z$ can be represented by $z_i = 0, \forall \{i \in \mathbb{N}: i \le m\}$. The vector for function values is defined as $u_i = u(x_i), \forall \{i \in \mathbb{N}: i \le n\}$. The radial moment matrix $R$ is represented as,

$$\underset{[nxn]}{R} = \begin{bmatrix} r_1(x_1, y_1) & r_1(x_2, y_2) & \cdots & r_1(x_n, y_n) \\ r_2(x_1, y_1) & r_2(x_2, y_2) & \cdots & r_2(x_n, y_n) \\ \vdots & \vdots & \ddots & \vdots \\ r_n(x_1, y_1) & r_n(x_2, y_2) & \cdots & r_n(x_n, y_n) \end{bmatrix} \tag{11}$$

and polynomial moment matrix $P$ is defined as,

$$\underset{[nxm]}{P} = \begin{bmatrix} p_1(x_1, y_1) & p_2(x_1, y_1) & \cdots & p_m(x_1, y_1) \\ p_1(x_2, y_2) & p_2(x_2, y_2) & \cdots & p_m(x_2, y_2) \\ \vdots & \vdots & \ddots & \vdots \\ p_1(x_n, y_n) & p_2(x_n, y_n) & \cdots & p_m(x_n, y_n) \end{bmatrix} \tag{12}$$

Since the distance is directionless, $r_i(x_j, y_j) = r_j(x_i, y_i)$, i.e. $R_{ij} = R_{ji}$, matrix $R$ is symmetric. A single solution is obtained if the inverse of the radial moment matrix $R$ exists,

$$\begin{Bmatrix} a \\ b \end{Bmatrix} = G^{-1} \begin{Bmatrix} u \\ z \end{Bmatrix} \tag{13}$$

The solvability of this system is usually guaranteed by the requirements $rank(p) = m \leq n$ [35]. In this work, the influence-domain will always possess enough nodes to largely satisfy the previously mentioned condition. It is possible to obtain the interpolation with

$$u^h(x_I) = \{r(x_I)^T; p(x_I)^T\}G^{-1} \begin{Bmatrix} u \\ z \end{Bmatrix} = \{\Phi(x_I)^T; \Psi(x_I)^T\} \begin{Bmatrix} u \\ z \end{Bmatrix} \tag{14}$$

where the interpolation function vector $\Phi(x_I)$ is defined by

$$\Phi(x_I) = \{\varphi_1(x_I) \quad \varphi_2(x_I) \quad ... \quad \varphi_n(x_I)\} \tag{15}$$

and the residual vector $\Psi(x_I)$, with no relevant physical meaning, is expressed as follows,

$$\Psi(x_I) = \{\Psi_1(x_I) \quad \Psi_2(x_I) \quad ... \quad \Psi_m(x_I)\} \tag{16}$$

Since

$$u^h(x_I) = \Phi(x_I)^T u = \{\Phi(x_I)^T; \Psi(x_I)^T\} \begin{Bmatrix} u \\ z \end{Bmatrix}, \tag{17}$$

it is possible to obtain the partial derivatives of the interpolated field variable, with respect to a generic variable $\xi$, which can be $\xi = x$ or $\xi = y$, with the following expression,

$$\frac{\partial u^h(x_I)}{\partial \xi} = \frac{\partial \Phi(x_I)^T}{\partial \xi} u = \left\{ \frac{\partial \Phi(x_I)^T}{\partial \xi}; \frac{\partial \Psi(x_I)^T}{\partial \xi} \right\} \begin{Bmatrix} u \\ z \end{Bmatrix} \tag{18}$$

From equation (14) it is possible to write

$$\left\{ \frac{\partial \Phi(x_I)^T}{\partial \xi}; \frac{\partial \Psi(x_I)^T}{\partial \xi} \right\} = \frac{\partial(\{r(x_I)^T; p(x_I)^T\}G^{-1})}{\partial \xi} \tag{19}$$

Since the moment matrix $G$ does not depend on the variable $x_I$, equation (19) can be rewritten as,

$$\left\{ \frac{\partial \Phi(x_I)^T}{\partial \xi}; \frac{\partial \Psi(x_I)^T}{\partial \xi} \right\} = \{ \frac{\partial r(x_I)^T}{\partial \xi}; \frac{\partial p(x_I)^T}{\partial \xi} \}G^{-1} \tag{20}$$

The partial derivatives of the MQ-RBF vector $r(x_I)$, with respect to a generic variable $\xi$, can be obtained for each component $\partial r_i(x_I)/\partial \xi$ with the expression,

$$\frac{\partial r_i(x_I)}{\partial \xi} = 2p(\xi_i - \xi_I)(d_{iI}^2 + c^2)^{p-1} \tag{21}$$

The RPI test functions $\Phi(x_I)$ depend exclusively on the distribution of scattered nodes [12]. Previous works [12], [14], [27] show that RPI test functions possess the Kronecker delta property, facilitating the imposition of essential and natural boundary conditions. Since the obtained RPI test functions have a local compact support, it is possible to construct and assemble well-

conditioned and banded stiffness matrix. If a polynomial basis is included, the RPI test functions have reproducing properties and possess the partition of unity property [12].

# 3. Free vibration analysis and matrix formulation

Considering the solid with a domain $\Omega \subset \mathbb{R}^3$ bounded by $\Gamma$. The dynamic equilibrium based on the principle of virtual work can be written as the following, in absence of damping effects

$$\int_\Omega \delta\boldsymbol{\varepsilon}^T \boldsymbol{\sigma}\, d\Omega + \int_\Omega \delta\boldsymbol{u}^T \rho\, \ddot{\boldsymbol{u}}\, d\Omega \int_\Omega \delta\boldsymbol{u}^T \boldsymbol{b}\, d\Omega - \int_{\Gamma_t} \delta\boldsymbol{u}^T \boldsymbol{t}\, d\Gamma = 0 \tag{22}$$

being $\boldsymbol{u}$ and $\ddot{\boldsymbol{u}}$, respectively, the displacement and the acceleration field, $\boldsymbol{b}$ is the body force vector and $\boldsymbol{t}$ the traction on the natural boundary $\Gamma_t$. The strain vector $\boldsymbol{\varepsilon}$ is defined as

$$\boldsymbol{\varepsilon} = \boldsymbol{L}\,\boldsymbol{u} \tag{23}$$

where $\boldsymbol{L}$ is the differential operator in the following matrix, Eq. (24):

$$\boldsymbol{L} = \begin{bmatrix} \dfrac{\partial}{\partial x} & 0 & 0 & \dfrac{\partial}{\partial y} & 0 & \dfrac{\partial}{\partial z} \\[2mm] 0 & \dfrac{\partial}{\partial y} & 0 & \dfrac{\partial}{\partial x} & \dfrac{\partial}{\partial z} & 0 \\[2mm] 0 & 0 & \dfrac{\partial}{\partial z} & 0 & \dfrac{\partial}{\partial y} & \dfrac{\partial}{\partial x} \end{bmatrix}^T \tag{24}$$

The linear constitutive relations can be given by

$$\boldsymbol{\sigma} = \boldsymbol{c}\boldsymbol{\varepsilon} \tag{25}$$

Where $\boldsymbol{\sigma}$ is the stress tensor and $\boldsymbol{c}$ is the material matrix defined as

$$\boldsymbol{c} = \mu_1 \begin{bmatrix} 1 & \nu & \nu & 0 & 0 & 0 \\ \nu & 1 & \nu & 0 & 0 & 0 \\ \nu & \nu & 1 & 0 & 0 & 0 \\ 0 & 0 & 0 & \mu_2 & 0 & 0 \\ 0 & 0 & 0 & 0 & \mu_2 & 0 \\ 0 & 0 & 0 & 0 & 0 & \mu_2 \end{bmatrix} \tag{26}$$

where $\mu_1 = E/(1 - \nu^2)$ and $\mu_2 = E/(2 + 2\nu)$, where $E$ is the Young's modulus and $\nu$ is the Poisson's ratio. In conclusion, the first term of Eq. (22) can be presented as

$$\int_\Omega \delta\boldsymbol{\varepsilon}^T \boldsymbol{\sigma}\, d\Omega = \delta\boldsymbol{u} \left[ \int_\Omega \boldsymbol{B}^T \boldsymbol{c}\boldsymbol{B}\, d\Omega \right] \boldsymbol{u} \tag{27}$$

The second term of Eq. (22) can be written as

$$\int_\Omega \delta \mathbf{u}^T \rho \, \ddot{\mathbf{u}} \, d\Omega = \int_\Omega \delta(\mathbf{H}\mathbf{u})^T \boldsymbol{\rho}(\mathbf{H}\ddot{\mathbf{u}}) d\Omega = \delta \mathbf{u} \left[ \int_\Omega \mathbf{H}^T \boldsymbol{\rho}\mathbf{H} d\Omega \right] \ddot{\mathbf{u}} \tag{28}$$

where $\boldsymbol{B}$ is the deformation matrix, defined in Eq. (29), $\boldsymbol{H}$ is the interpolation function (defined for each integration point $\boldsymbol{x}_I$ as: $\boldsymbol{H}_I = \boldsymbol{\varphi}(\boldsymbol{x}_I)\boldsymbol{I}$) and $\boldsymbol{\rho} = \rho\boldsymbol{I}$, being $\rho$ the mass density of the material and $\boldsymbol{I}$ the identity matrix with size $3 \times 3$. Thus, the stiffness matrix can be defined as: $\boldsymbol{K} = \int_\Omega \boldsymbol{B}^T \boldsymbol{c}\boldsymbol{B} d\Omega$, and the mass matrix as: $\boldsymbol{M} = \int_\Omega \boldsymbol{H}^T \boldsymbol{\rho}\boldsymbol{H} d\Omega$.

$$\boldsymbol{B}(\boldsymbol{x}_I)_i^T = \begin{bmatrix} \dfrac{\partial \varphi_i}{\partial x} & 0 & 0 & \dfrac{\partial \varphi_i}{\partial y} & 0 & \dfrac{\partial \varphi_i}{\partial z} \\[2mm] 0 & \dfrac{\partial \varphi_i}{\partial y} & 0 & \dfrac{\partial \varphi_i}{\partial x} & \dfrac{\partial \varphi_i}{\partial z} & 0 \\[2mm] 0 & 0 & \dfrac{\partial \varphi_i}{\partial z} & 0 & \dfrac{\partial \varphi_i}{\partial y} & \dfrac{\partial \varphi_i}{\partial x} \end{bmatrix} \tag{29}$$

The force vectors are defined by the third and fourth terms of Eq. (22),

$$\boldsymbol{F}_t = \int_{\Gamma_t} \boldsymbol{H}^T \boldsymbol{t} d\Gamma_t \qquad and \qquad \boldsymbol{F}_b = \int_\Omega \boldsymbol{H}^T \boldsymbol{b} d\Omega \tag{30}$$

Both vectors can be summed in order to obtain, $\boldsymbol{F} = \boldsymbol{F}_t + \boldsymbol{F}_b$. Since the RPIM interpolation function possesses the delta Kronecker property, the essential boundary conditions can be directly imposed in the mass matrix and in the stiffness matrix using the same impositions techniques used in FEM. In this work, the direct imposition method is applied [12].

Thus, the equilibrium equations governing the linear dynamic response, neglecting the damping effect, can be represented in the following matrix form, Eq. (31)

$$\boldsymbol{M}\ddot{\boldsymbol{U}} + \boldsymbol{K}\boldsymbol{U} = \boldsymbol{F} \tag{31}$$

where $\boldsymbol{U} = \boldsymbol{u}$ and $\ddot{\boldsymbol{U}} = \ddot{\boldsymbol{u}}$. The fundamental mathematical method used to solve Eq. (31) is the separation of variables. This approach [36] assumes that the solution can be expressed in the following form:

$$\boldsymbol{U}(t) = \Phi \boldsymbol{X}(t) \tag{32}$$

where $\Phi$ is an $n_{3D} \times n_{3D}$ square matrix containing $m$ spatial vectors independent of the time variable $t$, $\boldsymbol{X}(t)$ is a time dependent vector, and $n_{3D} = 3N$ for the 3D formulation, being $N$ the total number of nodes in the problem domain. The components of $\boldsymbol{X}(t)$ are called generalized displacements. From Eq. (32) it follows that $\ddot{\boldsymbol{U}}(t) = \Phi \ddot{\boldsymbol{X}}(t)$ . It is required that the space functions satisfy the following stiffness and mass orthogonality conditions:

$$\Phi^T K \Phi = W \quad \text{and} \quad \Phi^T M \Phi = I \tag{33}$$

where $W$ is the diagonal matrix which contains the free vibration frequencies, represented as $\omega_i^2$. After substituting Eq. (33) and its derivatives in order to time into Eq. (31) and pre-multiplying it by $\Phi^T$, the equilibrium equation that corresponds to the modal generalized displacement is obtained. The solution can be presented in the following form,

$$\boldsymbol{u}(t) = \boldsymbol{\phi}\sin(\omega(t - t_0)) \tag{34}$$

where $\boldsymbol{\phi}$ is the vector or order $n_{3D}$, $t$ is the time variable, $t_0$ is the constant initial time and $\omega$ is the vibration frequency vector. Substituting the former solution into Eq. (35) the generalized eigenproblem is obtain, from which $\boldsymbol{\phi}$ and $\omega$ must be determined,

$$K\boldsymbol{\phi} = \omega^2 M\boldsymbol{\phi} \tag{35}$$

Eq. (35) yields the $n_{3D}$ eigensolutions:

$$\begin{bmatrix} K\boldsymbol{\phi}_1 = \omega_1{}^2 M\boldsymbol{\phi}_1 \\ K\boldsymbol{\phi}_2 = \omega_2{}^2 M\boldsymbol{\phi}_2 \\ \vdots \\ K\boldsymbol{\phi}_{n_{3D}} = \omega_{n_{3D}}{}^2 M\boldsymbol{\phi}_{n_{3D}} \end{bmatrix} \tag{36}$$

The vector $\boldsymbol{\phi}_i$ is called the ith mode shape vector and $\omega_i$ is the corresponding vibration frequency. Defining a matrix $\Phi$ whose columns are the eigenvectors $\boldsymbol{\phi}_i$,

$$\Phi = [\boldsymbol{\phi}_1 \ \boldsymbol{\phi}_2 \ \dots \ \boldsymbol{\phi}_{n_{3D}}] \tag{37}$$

and a diagonal matrix $W$ which stores the eigenvalues $\omega_i$,

$$W = \begin{bmatrix} \omega_1{}^2 & 0 & \cdots & 0 \\ 0 & \omega_2{}^2 & \cdots & 0 \\ \vdots & \vdots & \ddots & \vdots \\ 0 & 0 & \cdots & \omega_{n_{3D}}{}^2 \end{bmatrix} \tag{38}$$

the $n_{3D}$ solutions can be written as:

$$K\Phi = M \ \Phi \ W \tag{39}$$

After substituting Eq. (32) and its time derivatives into Eq. (31) and pre-multiplying by $\Phi^T$, the equilibrium equation that corresponds to the modal generalized displacement is obtained.

## 4. Numerical applications

The vestibular system has two main components to promote the body balance: the semicircular canals (SCC) containing a sensory section called cupula (Figure 2) and two adjacent places with

otoconia crystals. This system is fulfilled with endolymph which through cupula interaction turn the mechanical movement into electric signals sent to the brain stating the body movement [37], [38].
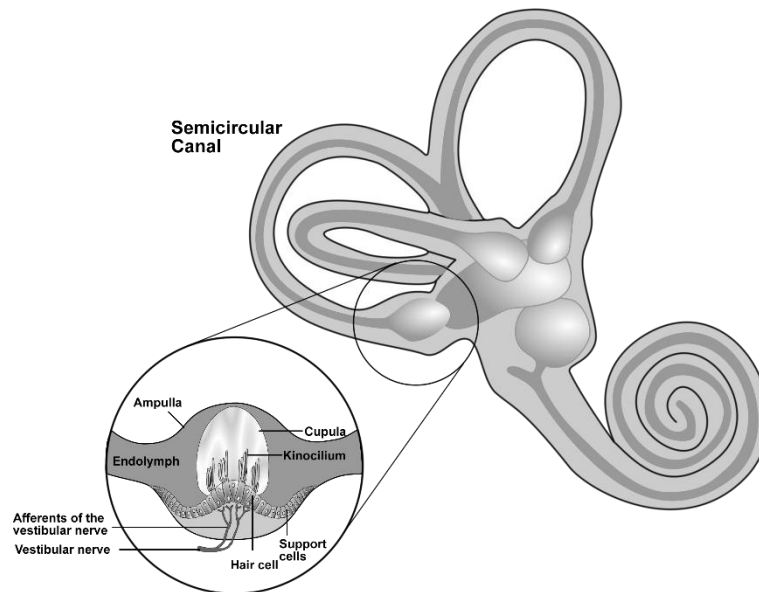


**Figure 2**- Vestibular system and cupula scheme.

Benign paroxysmal positional vertigo (BPPV) is one of the most common diseases affecting the vestibular system that causes vertigo [39]. Since vertigo episodes leads to sense of rotation that can cause nausea and vomiting, it is important to avoid that kind of symptoms which in a severe case could lead to falls, mainly in elders [40].

The main treatment implemented nowadays to avoid these symptoms is a set of some empirical maneuvers, knows as repositioning maneuvers, which shows high recurrence rates.

Cupulolithiasis is a particular case of BPPV, that happens when the otoconia get lost in the SCC and attached to the cupula inducing a false sensation of movement leading to vertigo [41]. The attachment of otoconia to the cupula will change material and mass distribution on the cupula and its shape and stiffness. The variation of these variables will have a relevant effect in the natural frequency of the cupula. One of the objectives of the present work is to understand the main structural differences between a healthy cupula and one with attached otoconia. The output of this study will allow to comprehend in what extent the attached otoconia amplify the cupula movement, inducing the previously mentioned false sensation of movement. Thus, in this work, for each studied model, the modal generalized displacements of the cupula will be obtained and analysed.

In order to numerically obtain the free vibration modes of the cupula, several 2D and 3D discrete models of the cupula (with and without attached otoconia) were built and analysed using the real dimensions and properties found in the literature [42].

98

### 4.1. Numerical model

First, four 2D discrete models of the cupula, without surrounding media, were constructed. The models respect the discretization pattern shown in Figure 3a). Since in this first stage the objective is to study (and compare) the convergence of the numerical approach, four 2D discrete models possess increasing number of nodes and quadrilateral elements. Thus, the first mesh (M1) possesses 153 nodes and 131 elements, the second mesh (M2) possesses 417 nodes and 382 elements, the third mesh (M3) possesses 897 nodes and 846 elements and the fourth mesh (M4) possesses 3320 nodes and 3221 elements.

In a second phase, the endolymph around the cupula was also included in the discretization, Figure 3b). To analyse its effect one mesh comprising 1417 nodes and 1350 elements was constructed using quadrilateral elements.

Regarding the cupulolithiasis simulation, six different models were constructed. The models consider the existent of otoconia particles (large individual otoconia or clusters) randomly placed above (Figure 3c)) and laterally (Figure 3d)) to the cupula. The objective of this last 2D study is to analyse the structural influence of the location and size of the otoconia in the complete system. In the end, a final 3D study was performed. Thus, four 3D discrete models of the cupula were built using tetrahedral elements (Figure 4). Regarding the level of the discretization, the four tetrahedral meshes possess the following discretization: M1 (350 nodes, 1461 elements), M2 (692 nodes, 3156 elements), M3 (1151 nodes, 5453 elements) and M4 (2128 nodes, 10704 elements).
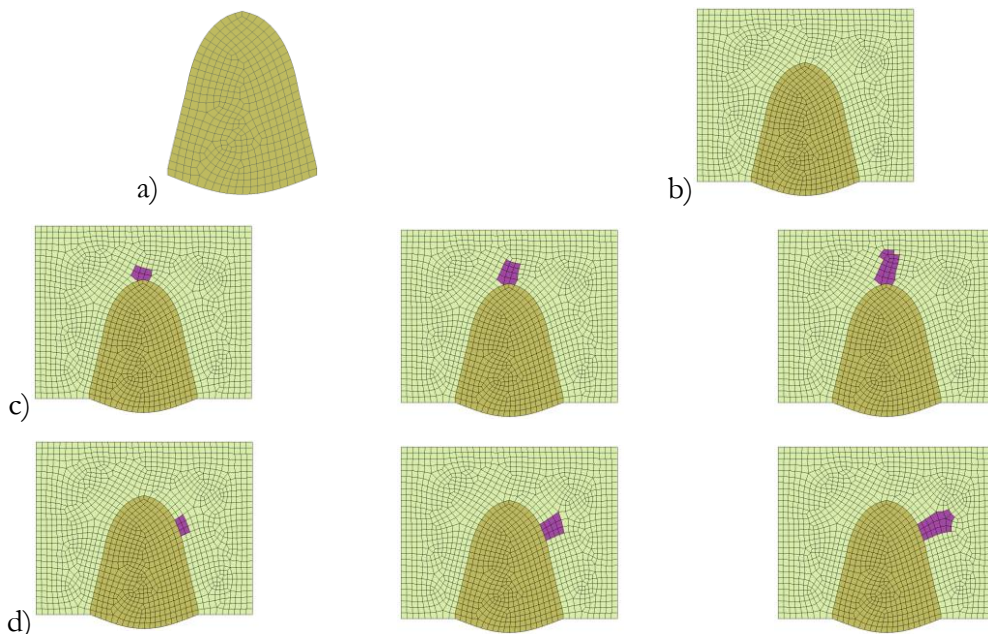


**Figure 3**- Two dimensional model; (a)Cupula; (b)Cupula with endolymph; (c)Cupula with endolymph and otoconia placed above with different sizes; (d) Cupula with endolymph and otoconia placed laterally with different size.

Regarding the material properties for the cupula, the following material properties are considered: $E = 5 \times 10^{-6}$MPa, $\upsilon = 0.49$ and $\rho = 1 \times 10^{-9}$ton/mm$^3$ for all simulations. In the case of the otoconia material, which are considered calcium carbonate crystals, the properties used are: $E = 6.6$MPa, $\upsilon = 0.45$ and $\rho = 2.4 \times 10^{-9}$ton/mm$^3$ [42]. To simulate the endolymph, the properties assumed are $\rho = 1 \times 10^{-9}$ton/mm$^3$ , $\upsilon = 0.49$ and $E = 1.27 \times 10^{-7}$MPa. Notice that the endolymph is an incompressible highly viscous fluid, with a dynamic viscosity, $\mu = 0.000852 \, Pa \cdot s$. It was verified (in this work) that the natural frequency of the cupula is around 50Hz, corresponding to a period of vibration of $T = 1/50$ s. Thus, knowing that $\dot{\tau} = \mu \dot{\gamma}$ and $\tau = G\gamma$, it is possible to instantaneously approximate the distortion modulus $G$ with $G \cong \mu/T \cong 0.0426 Pa$ (valid for the first vibration mode). Thus, since $G = E/(2 + 2v)$, then $E = 0.127$ Pa.
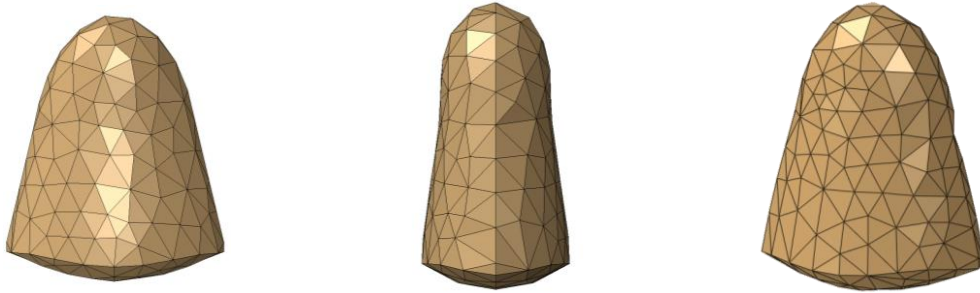


**Figure 4-**Three-dimensional finite element model of the cupula, front, lateral and three-dimensional views.

Regarding the essential boundary conditions, in the 2D and 3D models of the cupula without surrounding fluid, the nodes of the cupula's base are constrained in its degrees of freedom (no movement is allowed on those nodes). For the 2D models considering the surrounding endolymph, all the boundaries of the model are fully constrained.

## 5. Results

In this section are shown the results obtained from the several 2D and 3D analysis performed. Thus, the results regarding the convergence study are shown in Figure 5 respectively for FEM and three RPIM formulation varying the polynomial basis used to construct the shape function. "RPIM 1" represents the constant polynomial basis, "RPIM 2" signifies the linear polynomial basis and "RPIM 3" indicates the quadratic polynomial basis. The results show that the RPIM and the FEM solutions are very close for the two first natural frequencies and the results converged as the mesh density increased.

a)



b)

**Figure 5**- Convergence FEM and RPIM different polynomial basis for 2D model - natural frequency 1 (a) and 2 (b).
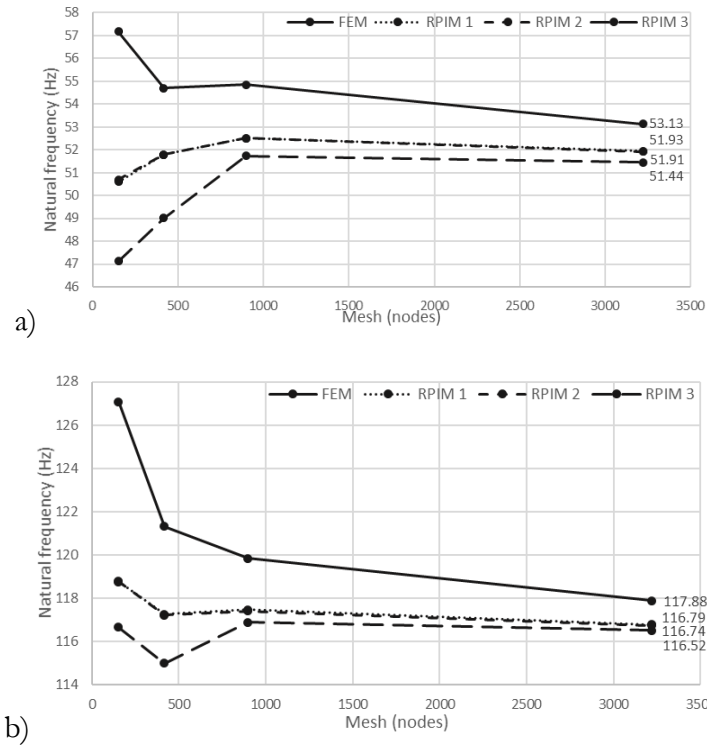
For meshes M1 and M4, the first ten vibration modes of the 2D cupula (Figure 3a) obtained with the FEM and RPIM are presented in Figure 6. Since from Figure 5 it is possible to visualize that the "RPIM 1" formulation is the one showing the best performance, only the results obtained with the RPIM formulation using the constant polynomial basis are shown in Figure 6.

In order to visualize automatically both the shape of the vibration mode and the vibration frequency, the results of the figures correspond to a fictitious displacement field obtained with: $U_i = \omega_i \phi_i$. This visualization method allows to observe in each figure the corresponding magnitude of the vibration frequency by observing to the maximum value of the displacement, designated by the red color; since the blue color corresponds to the lower displacement values.

The table 1 shows the natural frequencies obtained to the four meshes (M1 to M4) and it is possible to observe that both formulations (FEM and RPIM) possess a monotonic convergence path. Notice that, the RPIM formulation appears to achieve the convergence very fast. Although the solutions obtained with M1 are always very different from the ones obtain with M4 (regardless the numerical method used), it is possible to visualize that the solution obtained with M2 has already converged, being the results obtained with M2, M3 and M4 very similar, especially the ones obtained with the RPIM. The results indicate that first vibration frequency is between 51.91Hz and 53.13Hz. The first vibration frequency is easier to identify with precision due to the higher values of the following natural frequencies.

As table 1 shows, it is possible to visualize that the natural frequencies obtained with RPIM are lower than the ones obtained with FEM.
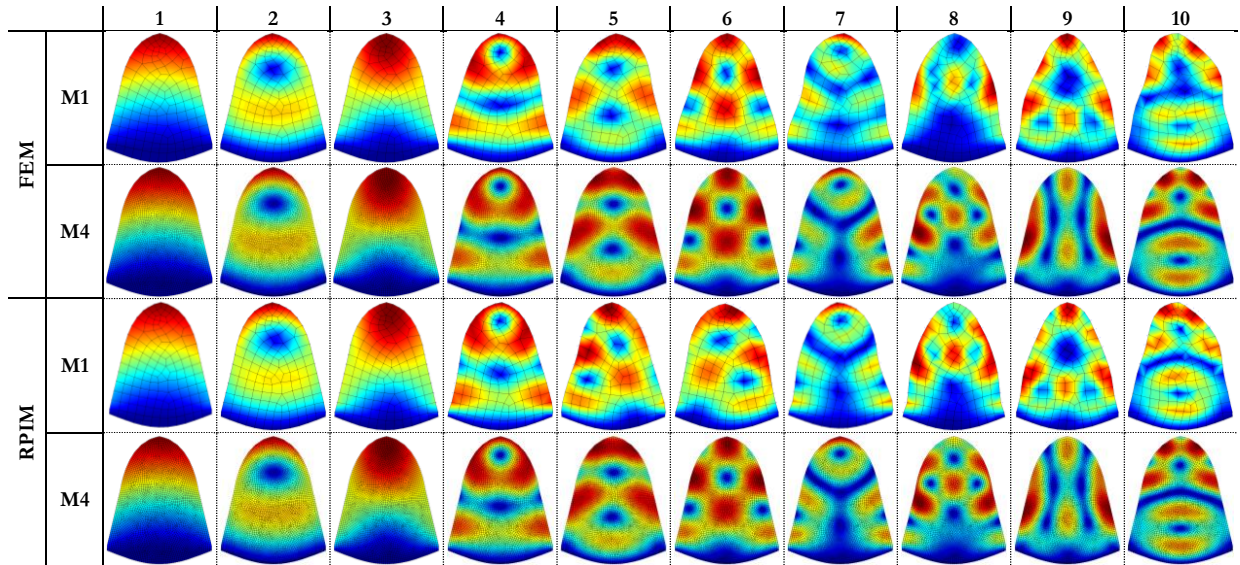


**Figure 6**-Ten first modes of the two-dimensional cupula with FEM and RPIM.

Next, the endolymph is included in the model (Figure 3b). The objective is to understand the influence of the endolymph in the natural frequency of the cupula. Since it was verified in the convergence study that the mesh density of mesh M2 is suitable to obtain a solution very close with the final converged solution, in this section a similar mesh density is used to discretize the problem domain. Thus, in order to observe the effect of the endolymph around the cupula, the first two vibration modes of the cupula are presented in the Figure 7 for the FEM and RPIM analysis.

**Table 1**- Natural frequency of ten first modes of the two-dimensional cupula with FEM and RPIM.

| | | Natural Frequency (Hz) | | | | | | | | | |
|---|---|---|---|---|---|---|---|---|---|---|---|
| | | 1 | 2 | 3 | 4 | 5 | 6 | 7 | 8 | 9 | 10 |
| FEM | M1 | 57.17 | 127.08 | 135.86 | 239.55 | 277.15 | 283.32 | 369.27 | 382.59 | 404.24 | 428.11 |
| | M2 | 54.70 | 121.32 | 131.62 | 226.17 | 259.80 | 265.13 | 345.26 | 350.33 | 362.51 | 386.60 |
| | M3 | 54.84 | 119.84 | 131.39 | 222.55 | 254.56 | 259.03 | 337.34 | 340.87 | 350.08 | 372.53 |
| | M4 | 53.13 | 117.88 | 128.90 | 217.48 | 248.80 | 253.34 | 328.04 | 331.17 | 340.07 | 360.07 |
| RPIM | M1 | 50.60 | 118.78 | 125.33 | 215.37 | 251.65 | 253.20 | 324.64 | 329.57 | 346.23 | 368.22 |
| | M2 | 51.78 | 117.27 | 126.98 | 216.15 | 249.26 | 251.89 | 324.66 | 329.32 | 340.28 | 359.79 |
| | M3 | 52.51 | 117.47 | 127.72 | 215.46 | 249.01 | 251.44 | 324.12 | 328.55 | 338.89 | 358.90 |
| | M4 | 51.91 | 116.79 | 127.01 | 214.75 | 246.32 | 249.71 | 321.81 | 326.11 | 336.47 | 356.47 |

Since now the surrounding endolymph is being considered, the obtained vibration modes are the vibration modes of the complete system (endolymph-cupula). However, since the cupula is much more rigid than the endolymph (and both possess a similar mass density), the first vibration modes of the system correspond to a direct excitation of the cupula structure. Notice that the first two vibration modes obtained with the FEM resemble the first vibration mode presented in the first column in Figure 6. Furthermore, the next three vibration modes obtained in this analysis are very similar with the second vibration mode obtained in the analysis of the cupula without surrounding fluid, as shown in the second column in Figure 6.

The same effect is verified for the RPIM formulation, since the first vibration mode of the present analysis resemble the first vibration mode obtained in the previous analysis, and the second and third vibration modes are very similar with the second vibration mode also obtained in the analysis of the cupula without surrounding elements.

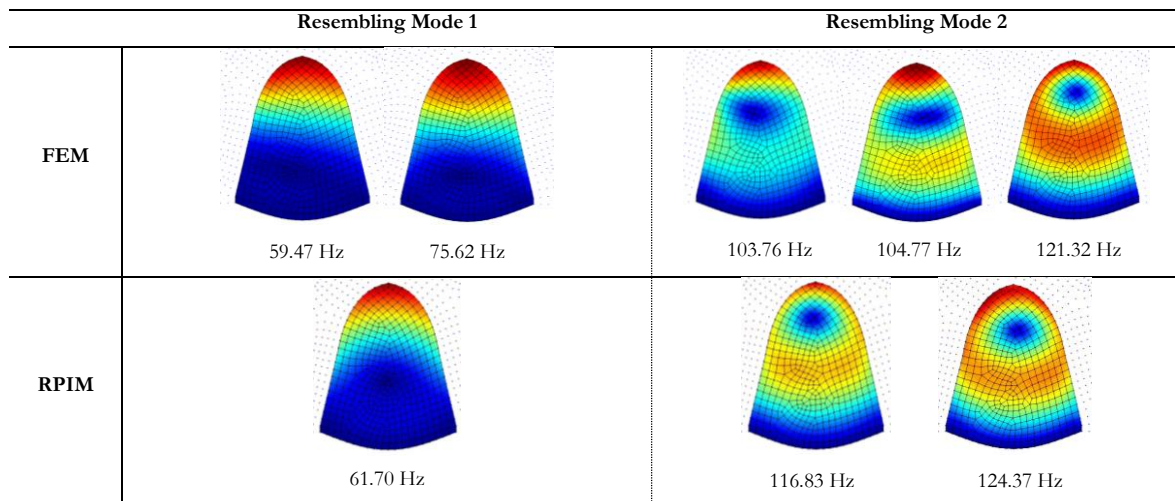| | Resembling Mode 1 | Resembling Mode 2 |
|---|---|---|
| FEM | 59.47 Hz  75.62 Hz | 103.76 Hz  104.77 Hz  121.32 Hz |
| RPIM | 61.70 Hz | 116.83 Hz  124.37 Hz |

**Figure 7-** Two first modes of the two-dimensional cupula with endolymph using FEM and RPIM (M2).

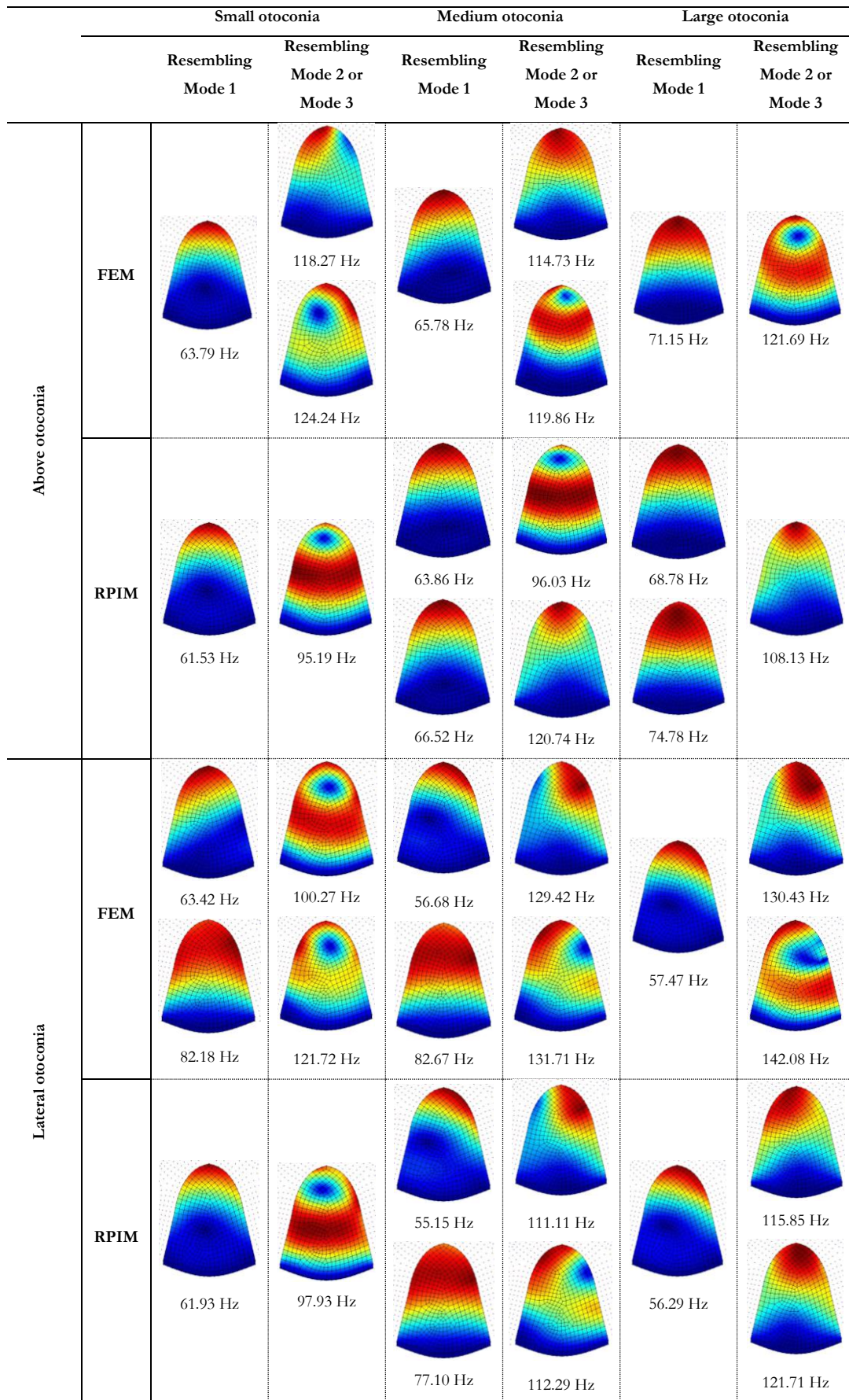|  |  | Small otoconia | | Medium otoconia | | Large otoconia | |
|  |  | Resembling Mode 1 | Resembling Mode 2 or Mode 3 | Resembling Mode 1 | Resembling Mode 2 or Mode 3 | Resembling Mode 1 | Resembling Mode 2 or Mode 3 |
| --- | --- | --- | --- | --- | --- | --- | --- |
| Above otoconia | FEM | 63.79 Hz | 118.27 Hz / 124.24 Hz | 65.78 Hz | 114.73 Hz / 119.86 Hz | 71.15 Hz | 121.69 Hz |
| | RPIM | 61.53 Hz | 95.19 Hz | 63.86 Hz / 66.52 Hz | 96.03 Hz / 120.74 Hz | 68.78 Hz / 74.78 Hz | 108.13 Hz |
| Lateral otoconia | FEM | 63.42 Hz / 82.18 Hz | 100.27 Hz / 121.72 Hz | 56.68 Hz / 82.67 Hz | 129.42 Hz / 131.71 Hz | 57.47 Hz | 130.43 Hz / 142.08 Hz |
| | RPIM | 61.93 Hz | 97.93 Hz | 55.15 Hz / 77.10 Hz | 111.11 Hz / 112.29 Hz | 56.29 Hz | 115.85 Hz / 121.71 Hz |

**Figure 8**- Two first modes of the two-dimensional cupula with endolymph and otoconia using FEM and RPIM.

104

The natural frequencies obtained for the cupula with endolymph to the first resembling mode are 59.47 Hz and 75.62 Hz using FEM and 61.70 Hz using RPIM analysis, which are close to values obtained with the isolated cupula, indicating that the endolymph fluid has a reduced influence in the magnitude of the cupula's natural frequency. The same observation was made analysing the results obtained to the natural frequencies corresponding to the second resembling mode: 103.76 Hz, 104.77 Hz and 121.32 Hz corresponding to FEM results and 116.83 Hz and 124.37 Hz obtained with RPIM.

After understanding the effects of including endolymph in the model, it was studied how the inclusion of attached otoconia affects the first natural frequencies of the system. As in the previous example, the results here presented only show the cupula because the complete representation of the complete model (cupula-endolymph-otoconia) difficult the identification/observation of the vibration mode of the cupula.

Thus, in Figure 8 are presented vibration modes resembling mode 1 of the cupula and the obtained vibration modes resembling mode 2 or mode 3 of the cupula.

The results in Figure 8 show the vibration modes obtained with the conditions represented in the Figure 3(c) and (d), corresponding, respectively, to the otoconia placed above and laterally to the cupula.

Comparing with the natural frequency obtained using the model with otoconia placed in the top of the cupula, it was expected a lower natural frequency than the one found when the otoconia is placed laterally to the cupula. This effect was not consistently observed in Figure 8 for all vibration frequencies, indicating that the inclusion of otoconia in the model does not significantly influences the natural frequency of the system cupula/otoconia. Notice that in these examples the otoconia particles/cluster have a very reduced dimension (in comparison with the cupula), which explains the observed lack of influence.

Regarding the vibration modes of the cupula is it possible to observe, mainly in the study with the medium and large otoconia using the RPIM formulation, that there are higher fictional displacements of the cupula's side where the otoconia are placed. This indicates that RPIM is capable to capture accurately the vibration mode of the structure and that the size of the otoconia influence the vibration mode of the cupula.

Regarding the 3D study, the results of the 3D convergence study of the isolated cupula are shown in Figure 9 respectively natural frequency 1 and 2 for FEM and the three RPIM formulations using distinct polynomial basis: the constant polynomial basis is the 'RPIM 1'; the linear polynomial basis is the 'RPIM 2'; and the quadratic polynomial basis is the 'RPIM 3'. The results show that the RPIM and the FEM solutions are close for both natural frequencies and the results converged, as expected, as the mesh density increased (similarly with the 2D model).
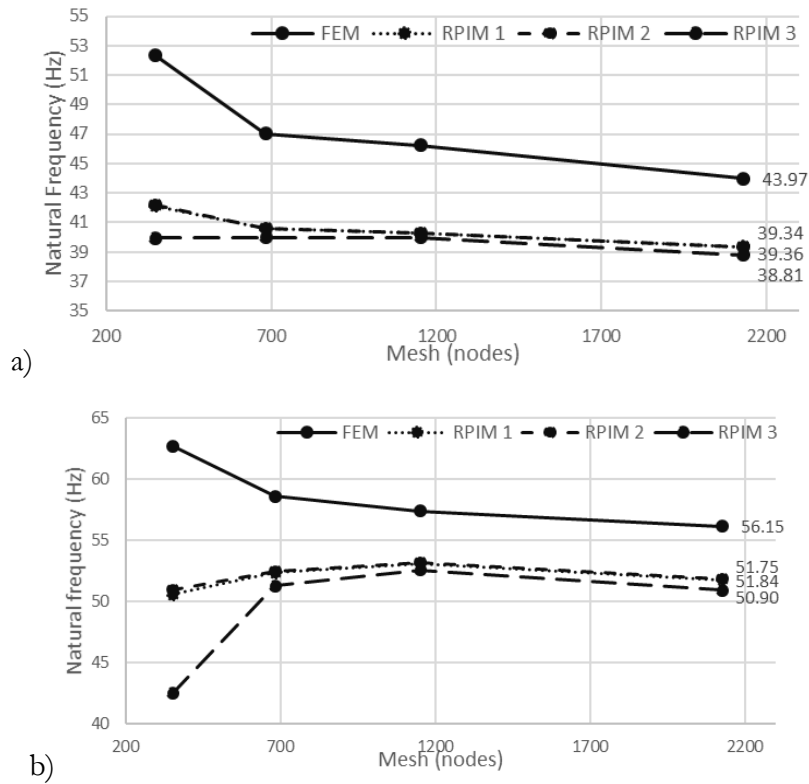
a)



b)

**Figure 9**- Convergence FEM and RPIM different polynomial basis for 3D model - natural frequency 1 (a) and 2 (b).

The analysis of the free vibration modes of the 3D cupula will allow to understand more realistically the overall behaviour of the cupula. The first five vibration modes of the 3D cupula obtained with FEM (using the four meshes mentioned before) are shown in Figure 10.

The vibration modes obtained with the 3D cupula using RPIM formulation using a constant polynomial basis, with the same four meshes, are presented in Figure 11. In both figures, the first and fifth modes are represented with the lateral view, the other ones with the front view. Notice that the second vibration mode shows a fictitious displacement aligned with the tangent direction of the canal. If this vibration mode is induced by resonance, expectably, it would be capable to detach the otoconia particles/clusters.
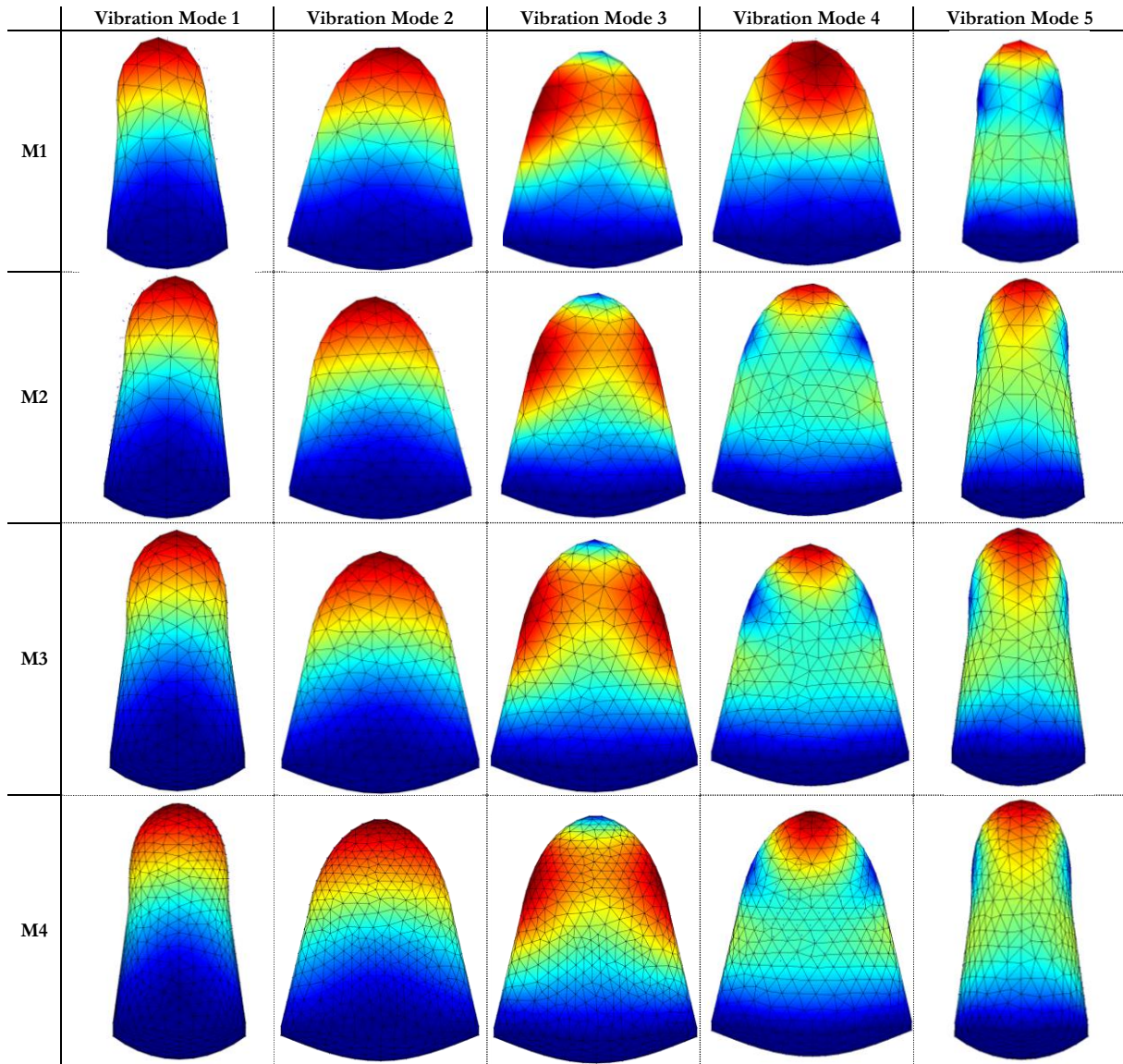
**Figure 10-** Five first modes of the three-dimensional cupula with FEM, four meshes.

Table 2 shows the first five vibration frequencies obtained for the cupula using the four meshes with FEM and RPIM analysis. It is possible to visualize that the RPIM formulations present high convergence rates. Notice that the solution obtained for meshes M2, M3 and M4 is almost identical. On the other hand, the FEM presents a lower convergence rate.

The 3D second vibration mode corresponds to the vibration configuration aligned with the tangent direction of the canal (Figure 10 and Figure 11). Thus, this vibration mode corresponds to the observed 2D first vibration mode. In the 3D RPIM solution, the natural frequencies of the second mode vibration (51.75 Hz) is also similar to the natural frequencies obtained to the first vibration mode in the 2D cupula (51.91 Hz) with mesh M4. This similarity is observed in the four meshes.
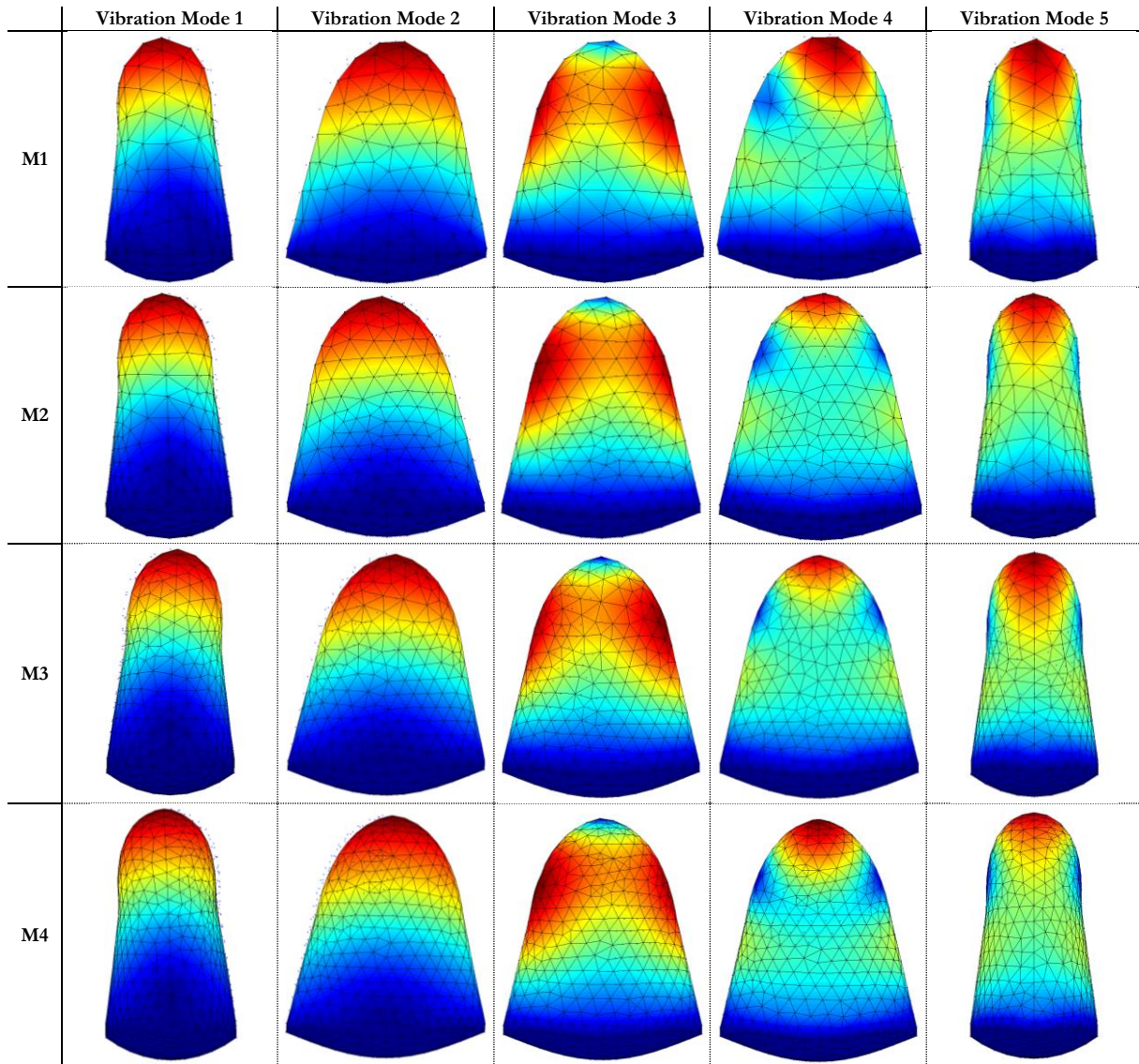
**Figure 11**- Five first modes of the three-dimensional cupula with RPIM, four meshes.

In table 2 is possible to visualize that for the densest mesh (M4), the FEM predicts a second vibration frequency of 56.14 Hz, and the RPIM indicates 51.71 Hz, which are very close.

**Table 2**- Natural frequency of five first modes of the three-dimensional cupula with FEM and RPIM (four meshes).

| | Natural Frequency (Hz) | | | | | | | |
|---|---|---|---|---|---|---|---|---|
| | **FEM** | | | | **RPIM** | | | |
| | M1 | M2 | M3 | M4 | M1 | M2 | M3 | M4 |
| **1** | 52.33 | 47.04 | 46.23 | 43.97 | 42.14 | 40.58 | 40.26 | 39.34 |
| **2** | 62.75 | 58.62 | 57.40 | 56.14 | 50.57 | 52.37 | 53.11 | 51.75 |
| **3** | 108.99 | 99.83 | 95.30 | 90.77 | 87.00 | 84.14 | 83.42 | 82.17 |
| **4** | 144.55 | 133.47 | 130.67 | 124.58 | 117.00 | 114.88 | 114.51 | 111.58 |
| **5** | 146.43 | 136.42 | 134.26 | 130.85 | 123.00 | 124.17 | 124.76 | 122.76 |

108

# 6.Conclusion

In this work, the FEM and the RPIM formulations were used to numerically analyse the dynamic response of the cupular structure of the inner ear. The results show that both methods lead to similar results. However, the most important achievement with this study, is the new research branch in the computational analysis of the vestibular system.

Regarding the results of the convergence obtained from the 2D analysis is it possible to conclude about the solid convergence of both formulations, RPIM and FEM, respectively indicating 51.91 Hz and 53.31 Hz as the natural frequency of the 2D model of the cupula. In the results of the 3D analysis is it possible to observe that the RPIM formulation present high convergence rates (table 2). Nevertheless, when compared with the RPIM, the FEM appears to have a lower convergence rate. This can be justified with the tetrahedral elements used in FEM, which generally lead to a low convergence rate. Notice that the natural frequency of the cupula obtained with the 3D model (in tangent direction) is very close with the natural frequency from the 2D analysis, regardless the numerical method used.

The dynamic response of a structure strongly depends on its geometric shape, material properties and essential boundaries, as confirmed by the results obtained in this work. The response of the cupula when it is surrounded by endolymph (and also with attached otoconia particles) present different natural frequencies, as the results show. Nevertheless, the natural frequencies obtained in the 2D analysis are between 50.60Hz and 57.17Hz, meaning that it is possible to clearly identify the target resonance frequency of the cupula. These magnitudes are slightly lower compared to the ones obtained without the surrounding endolymph (59.47 Hz and 75.62 Hz for FEM and 61.70 Hz for RPIM). This result is relevant because it means that a simulation in which the surrounding endolymph is disregard will permit to obtain a satisfactory approximated solution. This observation will allow to perform sufficiently accurate analyses considering simplified models (analysing only the cupula), reducing the overall computational cost of the analysis.

The results obtained with the particular case of BPPV (cupulolithiasis) studied in this research work show the possibility to develop, in the future, new therapeutics to solve this pathology; based on the induction of the resonance vibration of the cupula by a sound source.

With this work, it was possible to understand that the natural frequency of the cupula with otoconia attached ranges between 56Hz or 82Hz and all the other vibration frequencies possess distinct values. Theoretically, the induction of resonance will force the cupula to vibrate, leading to the detachment of the otoconia from the cupula, even with different sizes and positions (above

and laterally). This procedure aims to reduce the vertigo symptoms and it could be achieved in a non-invasive way, such as listening to music with a predominant set of bass sounds.

## Acknowledgments

## References

[1] S.-H. Lee and J. S. Kim, "Benign Paroxysmal Positional Vertigo," *J Clin Neurol*, vol. 66, pp. 51–6351, 2010.

[2] H. K. Neuhauser and T. Lempert, "Vertigo: epidemiologic aspects.," *Semin. Neurol.*, vol. 29, no. 5, pp. 473–81, Nov. 2009.

[3] R. Jaeger, a Takagi, and T. Haslwanter, "Modeling the relation between head orientations and otolith responses in humans.," *Hear. Res.*, vol. 173, no. 1–2, pp. 29–42, Nov. 2002.

[4] R. K. Duncan and J. W. Grant, "A finite-element model of inner ear hair bundle micromechanics.," *Hear. Res.*, vol. 104, no. 1–2, pp. 15–26, Feb. 1997.

[5] B. Grieser and D. Obrist, "Validation of assumptions on the endolymph motion inside the semicircular canals of the inner ear," *Intern. Reports Inst. Fluid Dyn. ETH Zurich*, pp. 1–16, 2012.

[6] M. Kassemi, D. Deserranno, and J. G. Oas, "Fluid–structural interactions in the inner ear," *Comput. Struct.*, vol. 83, no. 2–3, pp. 181–189, Jan. 2005.

[7] A. Kondrachuk, "Finite element modeling of the 3D otolith structure.," *J. Vestib. Res.*, vol. 11, no. 1, pp. 13–32, Jan. 2001.

[8] G. R. (Gui-R. Liu and S. S. Quek, *The finite element method : a practical course*, 2nd ed. Butterworth-Heinemann, 2013.

[9] V. P. Nguyen, T. Rabczuk, S. Bordas, and M. Duflot, "Meshless methods: A review and computer implementation aspects," *Math. Comput. Simul.*, vol. 79, no. 3, pp. 763–813, Dec. 2008.

[10] P. K. T.Belytschko,Y.Krongauz,D.Organ,M.Fleming, "Meshless methods: An overview and recent developments," *Comput. Methods Appl. Mech. Eng.*, vol. 139, no. 1–4, pp. 3–47, Dec. 1996.

[11] Y. T. GU, "Meshfree Methods and their comparisons," *Int. J. Comput. Methods*, vol. 02, no. 04, pp. 477–515, Dec. 2005.

[12] J. Belinha, *Meshless Methods in Biomechanics - Bone Tissue Remodelling Analysis. (Tavares JMRS, Natal Jorge RM (eds))*. Springer International Publishing Switzerland, 2014.

[13] J. Belinha, A. L. Araújo, A. J. M. Ferreira, L. M. J. S. Dinis, and R. M. Natal Jorge, "The analysis of laminated plates using distinct advanced discretization meshless techniques," *Compos. Struct.*, vol. 143, pp. 165–179, May 2016.

[14] L.M.J.S.Dinis; R.Natal Jorge; J. Belinha, "Analysis of 3D solids using the natural neighbour radial point interpolation method," *Comput. Methods Appl. Mech. Eng.*, vol. 196, no. 13–16, pp. 2009–2028, Mar. 2007.

[15] J. Belinha, L. M. J. S. Dinis, and R. M. Natal Jorge, "The natural radial element method," *Int. J. Numer. Methods Eng.*, vol. 93, no. 12, pp. 1286–1313, Mar. 2013.

[16] N. Sukumar, B. Moran, and T. Belytschko, "The natural element method in solid mechanics," *Int. J. Numer. Methods Eng.*, vol. 43, no. 5, pp. 839–887, Nov. 1998.

[17] N. Sukumar, B. Moran, A. Yu Semenov, and V. V. Belikov, "Natural neighbour Galerkin methods," *Int. J. Numer. Methods Eng.*, vol. 50, no. 1, pp. 1–27, Jan. 2001.

[18] AJM Ferreira, "A formulation of the multiquadric radial basis function method for the analysis of

laminated composite plates," *Compos. Struct.*, vol. 59, no. 3, pp. 385–392, Feb. 2003.

[19]    M.DoblaréE.CuetoB.CalvoM.A.MartínezJ.M.GarciaJ.Cegoñino, "On the employ of meshless methods in biomechanics," *Comput. Methods Appl. Mech. Eng.*, vol. 194, no. 6–8, pp. 801–821, Feb. 2005.

[20]    K. C. L. Wong, L. Wang, H. Zhang, H. Liu, and P. Shi, "Meshfree implementation of individualized active cardiac dynamics," *Comput. Med. Imaging Graph.*, vol. 34, no. 1, pp. 91–103, Jan. 2010.

[21]    G. Chen *et al.*, "A new approach for assigning bone material properties from CT images into finite element models," *J. Biomech.*, vol. 43, no. 5, pp. 1011–1015, Mar. 2010.

[22]    A. J. K. Z. ElZahab, E.Divo, "A localized collocation meshless method (LCMM) for incompressible flows CFD modeling with applications to transient hemodynamics," *Eng. Anal. Bound. Elem.*, vol. 33, no. 8–9, pp. 1045–1061, Aug. 2009.

[23]    A. K. Ho, L. Tsou, S. Green, and S. Fels, "A 3D swallowing simulation using smoothed particle hydrodynamics," *Comput. Methods Biomech. Biomed. Eng. Imaging Vis.*, vol. 2, no. 4, pp. 237–244, Oct. 2014.

[24]    M. J. Gámiz and J. A. Lopez-Escamez, "Health-Related Quality of Life in Patients over Sixty Years Old with Benign Paroxysmal Positional Vertigo," *Gerontology*, vol. 50, no. 2, pp. 82–86, Feb. 2004.

[25]    C. F. Santos, J. Belinha, F. Gentil, M. Parente, and R. N. Jorge, "An alternative 3D numerical method to study the biomechanical behaviour of the human inner ear semicircular canal.," *Acta Bioeng. Biomech.*, vol. 19, no. 1, pp. 3–15, 2017.

[26]    L. M. J. S. Dinis, R. M. Natal Jorge, and J. Belinha, "A natural neighbour meshless method with a 3D shell-like approach in the dynamic analysis of thin 3D structures," *Thin-Walled Struct.*, vol. 49, no. 1, pp. 185–196, Jan. 2011.

[27]    J. G. Wang and G. R. Liu, "A point interpolation meshless method based on radial basis functions," *Int. J. Numer. Methods Eng.*, vol. 54, no. 11, pp. 1623–1648, Aug. 2002.

[28]    G. R. L. J.G.Wang, "On the optimal shape parameters of radial basis functions used for 2-D meshless methods," *Comput. Methods Appl. Mech. Eng.*, vol. 191, no. 23–24, pp. 2611–2630, Mar. 2002.

[29]    T. Belytschko, Y. Y. Lu, and L. Gu, "Element-free Galerkin methods," *Int. J. Numer. Methods Eng.*, vol. 37, no. 2, pp. 229–256, Jan. 1994.

[30]    W. K. Liu, S. Jun, S. Li, J. Adee, and T. Belytschko, "Reproducing kernel particle methods for structural dynamics," *Int. J. Numer. Methods Eng.*, vol. 38, no. 10, pp. 1655–1679, May 1995.

[31]    S. N. Atluri and T. Zhu, "A new Meshless Local Petrov-Galerkin (MLPG) approach in computational mechanics," *Comput. Mech.*, vol. 22, no. 2, pp. 117–127, Aug. 1998.

[32]    O. C. Zienkiewicz and R. L. Taylor, *The Finite Element Method*, 4th ed. London: McGraw-Hill, 1994.

[33]    K.-J. Bathe, *Finite element procedures in engineering analysis*. Prentice-Hall, 1982.

[34]    L. M. J. S. Dinis, R. M. Natal Jorge, and J. Belinha, "Analysis of plates and laminates using the natural neighbour radial point interpolation method," *Eng. Anal. Bound. Elem.*, vol. 32, no. 3, pp. 267–279, 2008.

[35]    J. G. Wang, G. R. Liu, and Y. G. Wu, "A point interpolation method for simulating dissipation process of consolidation," *Comput. Methods Appl. Mech. Eng.*, vol. 190, no. 45, pp. 5907–5922, Aug. 2001.

[36]    Klaus-Jürgen Bathe, *Finite Element Procedures Second Edition*, Englewood Cliffs. Prentice-Hall, 1996.

[37]    Winter DA, "Human balance and posture control during standing and walking," *Gait Posture*, vol. 3, no. 4, pp. 193–214, Dec. 1995.

[38]    H. C. Diener and J. Dichgans, "On the role of vestibular, visual and somatosensory information for dynamic postural control in humans.," *Prog. Brain Res.*, vol. 76, pp. 253–62, 1988.

[39]    M. Karatas, "Central Vertigo and Dizziness," *Neurologist*, vol. 14, no. 6, pp. 355–364, Nov. 2008.

[40]    J. Taylor and H. P. Goodkin, "Dizziness and vertigo in the adolescent.," *Otolaryngol. Clin. North Am.*, vol. 44, no. 2, pp. 309–21, vii–viii, Apr. 2011.

[41]    T. M. Squires, M. S. Weidman, T. C. Hain, and H. a. Stone, "A mathematical model for top-shelf vertigo: The role of sedimenting otoconia in BPPV," *J. Biomech.*, vol. 37, no. 8, pp. 1137–1146, Aug. 2004.

[42]    J. L. Davis, J. Xue, E. H. Peterson, and J. W. Grant, "Layer thickness and curvature effects on otoconial membrane deformation in the utricle of the red-ear slider turtle: static and modal analysis.," *J. Vestib. Res.*, vol. 17, no. 4, pp. 145–62, Jan. 2007.

## 2.7.   Highlights of Contribution VI

The aim of this contribution was analyze how the intensity of physical activity (PA) influence the dizziness symptoms. This evaluation was, for the first time, performed using accurate accelerometer data.

Therefore, the main contents of this publication include:

I.     Review evidencing BPPV physiology and associated symptoms;

II.    Epidemiologic report on the BPPV incidence in Portugal and worldwide;

III.   Literature review on the impact of sports activity in dizziness symptoms:

Dizziness is one of the major complaints among athletes, mainly due to the sharp movements performed during PA [42], even in young population. The unexpected otoconia detachment from the macula could induce BPPV, which could occur as a consequence of intense PA sports, such as swimming, aerobics, jogging and fencing [43,44], as some authors report.

IV.    Physical activity measurement and classification in different intensity levels using an accelerometer:

A sample of 52 females aged between 19 to 34 years-old were randomly selected from the student population of University of Porto. For the present study, women used the accelerometer (from Actigraph[45,46]) over the right hip on an elasticized belt for seven consecutive days to measure the PA. The activity levels were based in mean count/min; and each minute of wear time during the monitoring period was classified into the following categories: sedentary (0–99 counts); light (100–2019 counts); moderate (2020-5998 counts); vigorous (≥5999); or moderate-to-vigorous (MVPA) (≥ 2020) PA, according to cut points reported in a previous validation study [47].

V.     Dizziness data collection by using a validated questionnaire, the Dizziness Handicap Inventory (DHI), which could be find appended;

VI.    Statistic methodology description:

The performed statistical analysis was the Spearman correlation, to verify the associations between the dizziness score and PA levels. The logistic regression model was used to explain the relationship between the dizziness occurrence variable (yes vs no) and PA levels.  The Chi-square test was used

to determine if there is a significant relationship between the categorical variables (high or low-impact sports). All statistical analyses were performed using procedures from sample survey data with software package Statistical Package for Social Sciences (SPSS).

VII.   Analysis and conclusion of the obtained results:

According to the Spearman correlation, the dizziness score had a negative association with light PA (P=0.030, r=-0.301), which means that, in the analyzed sample of young women, those who practice light PA had fewer vertigo symptoms; and a positive association with vigorous PA (P=0.000, r=0.505), which is in line with some research works [48,49]. Furthermore, the logistic regression analysis (Table 1.1) shows that every additional minute of vigorous PA per day increases in 1.2 times the chance of developing dizziness symptoms.

**Table 1.1 -** Relationship between PA levels and dizziness incidence.

| Variables | β estimate | Standard error | OR | P value |
|---|---|---|---|---|
| Sedentary PA | 0.001 | 0.001 | 1.001 | 0.266 |
| Light PA | 0.000 | 0.001 | 1.000 | 0.696 |
| Moderate PA | 0.010 | 0.017 | 1.010 | 0.542 |
| Vigorous PA | 0.117 | 0.047 | 1.164 | 0.013* |

PA: Physical activity; OR: odds ratio; * statistically significant

The complete document can be found in the next sub-chapter.

## 2.7.1.    Contribution VI

# <u>Is the severity of dizziness symptoms depending on the physical activity intensity?</u>

*Submitted to an International Journal*

# Is the Severity of Dizziness Symptoms Depending on the Physical Activity Intensity?

Carla F. Santos [a,e], Thuane DaRoza [b], J. Belinha [a,c], Fernanda Gentil [a,d], and Renato Natal Jorge [a,e]

a INEGI, Institute of Mechanical Engineering and Industrial Management, Rua Dr. Roberto Frias, Porto, Portugal.
b Santa Catarina State University, Florianópolis, Brazil
c School of Engineering, Polytechnic of Porto, (ISEP), Porto, Portugal
d Clínica ORL-Dr. Eurico Almeida, Widex, Escola Superior de Saúde – I.P.Porto, Porto,Portugal
e FEUP, Faculty of Engineering of the University of Porto, Rua Dr. Roberto Frias, Porto, Portugal.

## Abstract

Dizziness, a widespread symptom, is commonly associated with vestibular system disorders; however, it is not always possible to conclude about its definitive causes. The association between physical activity and dizziness is still not fully understood, and it has never been investigated using accelerometer quantified data, as this work aims to accomplish.

To obtain reliable results on how physical activity influences dizziness in young women, a cross-sectional study was performed with 52 participants. The physical activity intensity level was assessed using an accelerometer, and a validated questionnaire acquired the dizziness information.

A negative association between dizziness and light physical activity (P=0.030, r=-0.301), and a positive association with vigorous physical activity (P=0.000, r=0.505) were found. Furthermore, each minute of vigorous physical activity increases the chance to develop dizziness. Physical activity intensity levels seem to influence dizziness symptoms, both by reducing their occurrence due to light physical activity and by increasing their occurrence due to vigorous physical activity.

# 1.Introduction

The vestibular system of the inner ear is the main decoder of body locomotion signs to the brain [1], and many diseases are affecting the vestibular apparatus, which can lead to dizziness symptoms. Dizziness is one of the most common medical complaints, affecting roughly 20%-30% of the world population [2]. It may be present in all age ranges, although its prevalence increases with ageing and, as such, it is the most frequent illness for subjects older than 70 years. In Europe, the dizziness prevalence for ages between 50 and 80 years old is 12.4%, while in Portugal dizziness related hearing problems affect 28.7% of the same age group [3]. Among all dizziness symptoms, vertigo refers to the sensation of rotation inside the head [4], most of the times called dizziness. Nevertheless, other incapacitating signs such as blurred vision, nausea, and difficulties in standing and walking can occur [5]. These symptoms are the result of conflicting information received by the brain concerning the body's position and movement [6].

By considering the fact that the average life expectancy is rising, vertigo should be viewed as a core health concern. It increases the risk of falls, leading to higher healthcare costs, and it affects the mortality in elders related to this risk factor [7]. Benign paroxysmal positional vertigo (BPPV) is the most common cause of vertigo [8] and, as the literature shows, 30% of the worldwide population has experienced it at least once in the lifetime [9]. Even in the young population, BPPV affects females twice as often as males [9]. A study regarding the prevalence of BPPV shows a 0.7% prevalence in women against 0.3% in men, between 18 and 39 years old [10]. BPPV also has an estimated lifetime prevalence of 2.4% in the adult population [11].

The main syndrome-related symptoms appear when specific calcium carbonate particles (also known as otoconia), which should be positioned in the sacs of the inner ear, dislodge from their correct location, inducing a false sensation of movement when the head slightly moves. One of the possible causes of such symptoms could be sharp movements performed during physical activity (PA) practice, with dizziness being one of the main complaints among athletes [12]. The accidental leak of the otoconia, potentially inducing BPPV, could occur as a result of intense PA sports, such as swimming, aerobics, fencing and jogging (even in young people) [13]. Moreover, 61.2% of occurrences associated with sports-related concussions report dizziness [14]. On the other hand, some authors advocate for the importance of practising regular moderate PA to avoid BPPV in women [15,16]. The fact that no consensus regarding this discussion has been reached is the primary motivation for this investigation, which aims to contribute to the scarce existent literature on the subject. To validate the influence of different

levels of PA with BPPV, the present study proposes, for the first time, assessing PA levels with an accelerometer and associate it with the dizziness symptoms among young women.

# 2.Materials and methods

This is a cross-sectional study approved by the ethical committee of Centro Hospital de São João-EPE (code: CES-120-13), which was conducted in accordance with the Declaration of Helsinki and has followed the international standards [17]. Random 52 female individuals aged 19 to 34 years old were selected between September 2013 and May 2014 from the student population of local Universities from the region of Porto, Portugal. All participants gave informed consent to all the performed surveys. Two distinct questionnaires were applied to the participants. The first one enquires about demographic characteristics, containing anthropometric information (age, mass and height) and practised sports. Considering that some head impact sports could dislodge the otoconia from their correct location and promote dizziness, football, handball and volleyball were classified as high-impact sports in this study. Pilates, dance, cycling and gym practice were considered low-impact sports. The second questionnaire had the objective of establishing the presence of dizziness symptoms using the Portuguese validated version of the Dizziness Handicap Inventory (DHI), and it was applied only if the participants affirmatively answered to have experienced, at least once, a dizziness sensation.

The DHI is a self-assessment questionnaire determining the daily life impact of dizziness and unbalance. A total of 25 questions integrate the survey, being the possible answers: 0-"Never", 1–"Rarely"; 2–"Sometimes"; 3–"Often"; 4–"Yes, permanently". The highest possible score is 100, and the questions are conceived to evaluate the functional, physical, and emotional impacts on dizziness disability. The handicap score classification is obtained according the following cut-off: light (1-15), mild (16-35), moderate (36-53) and severe (>54).

## 2.1. Physical Activity Measurement

The level of PA was assessed by using an accelerometer (model GT1M) from Actigraph (Actigraph®, LLC; Ft.Walton Beach, FL). Previous studies show that model GT1M from Actigraph is a technically reliable instrument, both within and across monitors [18], and it is also validated to quantifying activity levels in laboratory and field settings [19]. For the present study, women were asked to use the accelerometer over the right hip on an elasticised belt for

seven consecutive days. Participants were instructed to maintain their usual routine of activities and remove the device when swimming, bathing and sleeping, while a log diary was provided to register relevant information.

Accelerometer data was recorded in 5-s sampling periods (epochs) and then assembled in 60-s epochs for analysis. The requirement to accept the daily PA data as valid to the study is handling the accelerometer at least five days with 8 hours recorded per day for each participant.

Assuming that the monitor was not worn, non-wear time was defined as at least 60 consecutive minutes of zero activity intensity counts. Activity levels were based in mean count/min. Each minute of wear time during the monitoring period was classified into the following categories: sedentary (0–99 counts); light (100–2019 counts); moderate (2020-5998 counts); vigorous (≥5999); or moderate-to-vigorous (MVPA) (≥ 2020) PA, according to cut points reported in a previous validation study [20]. All data were processed with the Actilife software version v6.10.2. The outcome variable was calculated by dividing the sum of activity counts for a valid day by the number of minutes of wear time in that day across all valid days [20].

## 2.2. Statistics

All statistical analyses were performed using procedures from sample survey data with software Statistical Package for Social Sciences (SPSS) version 24.0 (SPSS Inc., Chicago, Illinois, USA). Absolute frequency, relative frequency, mean and standard deviation were used for the description of continuous variables, while proportions were calculated for categorical variables. Spearman correlation was used to verify the associations between the dizziness score and PA levels. To explain the relationship between the dizziness occurrence variable (yes *vs* no) and PA levels, a logistic regression model was performed. The Hosmer-Lemeshow statistic indicates that the model adequately fits the data ($p > 0.05$). Chi-square test was used to determine if there is a significant relationship between the categorical variables (presence or not of dizziness with women practising high or low-impact sports).

# 3. Results

The sample of the present study consisted of a total of 52 young women with 24.9±4.2 years old and with a normal body index mass of 21.3±1.9 Kg/m². Half of the women performed high-impact sports and the remaining half performed low-impact sports. Among them, 67.3% (n=35) self-reported dizziness symptoms. According to the DHI defined score, the outcomes

show that 26 (74.3%) women had a light handicap; 7 (20%) had a mild handicap, and 2 (5.7%) had a moderate handicap. Regarding the dimensions proposed by DHI, the physical dimension was the most affected, followed by the functional dimension and the emotional dimension.

According to Spearman correlation, dizziness score had a negative association with light PA (P=0.030, r=-0.301), and a positive association with vigorous PA (P=0.000, r=0.505), see Figure 1. Practising high or low-impact sports is not related to dizziness (P=0.375). The data in Figure 1 shows the amount of light and vigorous PA practised in minutes, compared with the dizziness score obtained in DHI. The logistic regression analysis (Table 1) shows that every additional minute of vigorous PA per day increases in 1.2 times the chance of developing dizziness symptoms.
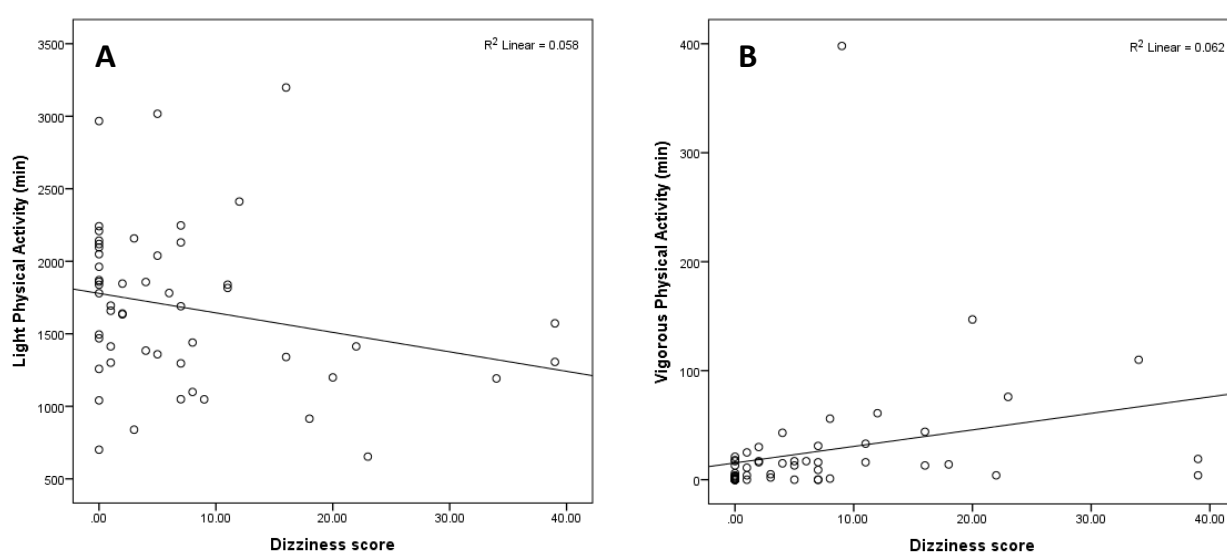


**Figure 1**- Association between Dizziness score with light (A) and vigorous (B) PA assessed by an accelerometer.

**Table 1**- Relationship between PA levels and dizziness incidence.

| Variables | β estimate | Standard error | OR | P value |
|---|---|---|---|---|
| Sedentary PA | 0.001 | 0.001 | 1.001 | 0.266 |
| Light PA | 0.000 | 0.001 | 1.000 | 0.696 |
| Moderate PA | 0.010 | 0.017 | 1.010 | 0.542 |
| Vigorous PA | 0.117 | 0.047 | 1.164 | 0.013* |

PA: Physical activity; OR: odds ratio; * statistically significant

# 4.Discussion

By using accelerometer data, the present study is the first to distinguish between different levels of PA to analyse the potential association with the occurrence of dizziness in young women. While several studies report the harmful effects of sports in dizziness [12], [21], [22], others verify the functional vertigo benefits induced by regular moderate PA [15], [16]. The present study found a negative association between dizziness score and light PA, which means that, in the analysed sample of young women, those who practice light PA had fewer vertigo symptoms. This result is in agreement with other authors, which have found that practising regular PA [15] or performing more activity during leisure, household, and occupational activities [16], could potentially decrease the risk of vertigo and BPPV symptoms. Since the accelerometer data is more accurate than the data obtained with a questionnaire [15], the present study can establish in a more reliable way the PA amount that improves dizziness symptomatology.

Since light PA is measured differently in the accelerometer than sedentary activity, it is also possible to conclude that an active person (who practices light sports activities) is healthier considering dizziness manifestation. Another finding of this work is the positive association between dizziness score and the practice of vigorous PA, which is in line with some research works [21], [23]. This occurs because dizziness symptoms, as a consequence of BPPV, can appear after intense effort, which possibly detaches the otoconia from the sacs, inducing a false sensation of movement. This result confirms the findings of Sennaroglu [22], who theorises that rapid head movements during swimming are one of the causes of BPPV. Another study [21], also adverts about the possibility of repeated acceleration-deceleration events during intensive workout induces vertigo symptoms of BPPV.

Regarding the hypothesis that high and low-impact sports influence the dizziness symptoms, no relationship was found in the analysed data. Despite this result, such factor should not be ignored as there are other studies [12] with athletes reporting dizziness, for example, as a consequence of a concussion during sports practice, even when swimming [22]. In the present study, this observation was not found, suggesting that future works reconsider this aspect, possibly enlarging the sample size.

This study also found that, in young women, every additional minute of vigorous PA per day increases in 1.2 times the chance of developing dizziness symptoms. Despite this significant result, women who do not practice PA at all seem to have a higher risk to develop BPPV according to Bazoni's study [15], who found a 2.62 higher risk of developing BPPV in

sedentary women. The present study has the advantage of using validated and objective measurement of the amount of PA, which is then compared to dizziness.

Some of the strengths of this study include the PA assessed by accelerometer and the fact that the data of the dizziness symptoms was obtained by a validated dizziness questionnaire adapted to the Portuguese language.

Limitations of the present study include the cross-sectional study design, which captures the data in a single point in time and hinders the possibility to establish a real cause and effect relationship. Another component that may be noted is the lack of severe dizziness handicap in the sample studied. Possibly, this observation could also be related to the age range studied, since the BPPV is most common in elders. Also, the inability to examine the relationship between PA and dizziness across all age ranges and the small sample size could increase the likelihood of a type II error.

# 5.Conclusion

This work has successfully studied the effect of PA on the severity of dizziness symptoms in young women. This was accomplished by employing accelerometers that measure continuous PA data, which was then cross-referenced with validated dizziness questionnaires applied to the same subjects. It was found that vigorous PA practice increases the severity of dizziness among young women. At the same time, this work also shows the benefits of practising light PA to avoid dizziness symptoms. Regarding the type of PA, no statistical relationship was found between high and low-impact sports with dizziness symptoms. Therefore, concerning dizziness symptoms and physical activity, possibly the balance is the secret.

# References

[1]    B. L. D. Richard C.Fitzpatrick,Jane E.Butler, "Resolving Head Rotation for Human Bipedalism," *Curr. Biol.*, vol. 16, no. 15, pp. 1509–1514, Aug. 2006.

[2]    M. von Brevern and H. Neuhauser, "Epidemiological evidence for a link between vertigo and migraine.," *J. Vestib. Res.*, vol. 21, no. 6, pp. 299–304, Jan. 2011.

[3]    M. Penger, R. Strobl, and E. Grill, "Country-specific and individual determinants of dizziness in Europe: results from the Survey of Health Ageing and Retirement in Europe (SHARE)," *Public Health*, vol. 149, pp. 1–10, Aug. 2017.

[4]    J. Taylor and H. P. Goodkin, "Dizziness and vertigo in the adolescent.," *Otolaryngol. Clin. North Am.*, vol. 44, no. 2, pp. 309–21, vii–viii, Apr. 2011.

[5]    M. Strupp, M. J. Thurtell, A. G. Shaikh, T. Brandt, D. S. Zee, and R. J. Leigh, "Pharmacotherapy of

vestibular and ocular motor disorders, including nystagmus," *J. Neurol.*, vol. 258, no. 7, pp. 1207–1222, Jul. 2011.

[6]    J. N. Wagner, M. Glaser, T. Brandt, and M. Strupp, "Downbeat nystagmus: aetiology and comorbidity in 117 patients," *J. Neurol. Neurosurg. Psychiatry*, vol. 79, no. 6, pp. 672–677, Oct. 2007.

[7]    L. Felipe, L. C. M. Cunha, F. C. M. Cunha, M. T. G. Cintra, and D. U. Gonçalves, "Presbivertigem como causa de tontura no idoso," *Pró-Fono Rev. Atualização Científica*, vol. 20, no. 2, pp. 99–104, Jun. 2008.

[8]    J. Wipperman, "Dizziness and Vertigo," *Prim. Care Clin. Off. Pract.*, vol. 41, no. 1, pp. 115–131, Mar. 2014.

[9]    M. D. Moreira *et al.*, "Prevalência e associações da vertigem posicional paroxística benigna em idosos," *Rev. CEFAC*, vol. 16, no. 5, pp. 1533–1540, Oct. 2014.

[10]   M. von Brevern *et al.*, "Epidemiology of benign paroxysmal positional vertigo: a population based study," *J. Neurol. Neurosurg. Psychiatry*, vol. 78, no. 7, pp. 710–715, Dec. 2006.

[11]   E. I. Cho and J. A. White, "Positional Vertigo: As Occurs Across All Age Groups," *Otolaryngol. Clin. North Am.*, vol. 44, no. 2, pp. 347–360, Apr. 2011.

[12]   C. A. Klenck, "The dizzy athlete.," *Curr. Sports Med. Rep.*, vol. 6, no. 1, pp. 25–31, Jan. 2007.

[13]   P. G. Giacomini, S. Ferraro, S. Di Girolamo, I. Villanova, and F. Ottaviani, "Benign paroxysmal positional vertigo after intense physical activity: a report of nine cases," *Eur. Arch. Oto-Rhino-Laryngology*, vol. 266, no. 11, pp. 1831–1835, Nov. 2009.

[14]   M. R. Lovell *et al.*, "Measurement of Symptoms Following Sports-Related Concussion: Reliability and Normative Data for the Post-Concussion Scale," *Appl. Neuropsychol.*, vol. 13, no. 3, pp. 166–174, Sep. 2006.

[15]   J. Bazoni *et al.*, "Physical Activity in the Prevention of Benign Paroxysmal Positional Vertigo: Probable Association," *Int. Arch. Otorhinolaryngol.*, vol. 18, no. 4, pp. 387–390, Aug. 2014.

[16]   L. Pollak, M. Kushnir, and H. S. Goldberg, "Physical inactivity as a contributing factor for onset of idiopathic benign paroxysmal positional vertigo," *Acta Otolaryngol.*, vol. 131, no. 6, pp. 624–627, Jun. 2011.

[17]   D. Harriss and G. Atkinson, "Ethical Standards in Sport and Exercise Science Research: 2014 Update·," *Int. J. Sports Med.*, vol. 34, no. 12, pp. 1025–1028, Nov. 2013.

[18]   M. P. Rothney, G. A. Apker, Y. Song, and K. Y. Chen, "Comparing the performance of three generations of ActiGraph accelerometers," *J. Appl. Physiol.*, vol. 105, no. 4, pp. 1091–1097, Jul. 2008.

[19]   S. G. Trost, K. L. McIver, and R. R. Pate, "Conducting accelerometer-based activity assessments in field-based research.," *Med. Sci. Sports Exerc.*, vol. 37, no. 11 Suppl, pp. S531-43, Nov. 2005.

[20]   R. P. TROIANO, D. BERRIGAN, K. W. DODD, L. C. MÂSSE, T. TILERT, and M. MCDOWELL, "Physical Activity in the United States Measured by Accelerometer," *Med. Sci. Sport. Exerc.*, vol. 40, no. 1, pp. 181–188, Jan. 2008.

[21]   D. Vibert, R. C. Redfield, and R. Häusler, "Benign Paroxysmal Positional Vertigo in Mountain Bikers," *Ann. Otol. Rhinol. Laryngol.*, vol. 116, no. 12, pp. 887–890, Dec. 2007.

[22]   S. Aksoy and L. Sennaroğlu, "Benign paroxysmal positional vertigo in swimmers.," *Kulak Burun Bogaz Ihtis. Derg.*, vol. 17, no. 6, pp. 307–10, 2007.

[23]   A. Katsarkas, "Benign paroxysmal positional vertigo (BPPV): idiopathic versus post-traumatic." *Acta Otolaryngol.*, vol. 119, no. 7, pp. 745–9, 1999.

# Chapter III
# Thesis Considerations

## 3.1.   General Discussion

Patients suffering from vertigo, still have to go through a long and exhausting set of tests to be able to be diagnosed. Furthermore, most of the patients complain about the insecurity and discomfort during all the rehabilitation process, mainly due to long sessions and slow results. The work developed during this thesis aims to improve the current knowledge and open simulation possibilities in the vestibular rehabilitation field, and ultimately improve the quality of life of all those affected.

The first step consisted in building the geometrical model of the vestibular system through an evolutionary process of constant validation, detailed mainly in Contributions I and III. The first main task of this process was the validation of the applied fluid methodology, presented in Contribution I. The selected FSI simulation option was the monolithic approach, due to its better accuracy in a multidisciplinary problem, such as the detailed vestibular system components. However, since the equations that govern the fluid flow and the displacement of the structure are solved simultaneously, such approach requires more computational resources, which translates to a larger simulation time. The reduced dimensions of the otoconia particles and all the vestibular structures led to choosing accuracy over computational time. Since the SPH is a particle method, it could also interfere in the indirect validation of the model, when comparing with other authors who do not use particle methods to simulate the endolymph. Consequently, the fluid simulation became one of the most challenging parts of the whole work. Nevertheless, the obtained results were quite similar to other authors, a comparison is shown in Contribution I. These reliable results were an important first step, allowing the method validation and encouraging further progression of the model. The evolution of the built vestibular model was present in Contribution III, where a simple experimental validation was performed. The SCC computational model was validated using a silicone mold, which was close to

the real SCC structure since it includes the cupula. The angle measured between the otoconia pathway and the cupula in three different situations in both models (numerical and experimental) allowed the model validation, which supported the following simulations using this SCC numerical model. Nevertheless, the silicone experimental model has some limitations as it should be thicker to enable sharpened evaluation.

The SCC simulation with or without otoconia allowed to support the distinct brain's perception between both situations, which endorse the model reliability and open a branch to further cupula behavior investigations. Furthermore, the global vestibular model disorder simulation allowed a novel perception on the rehabilitation maneuvers, which was the main goal of the present thesis.

The main disadvantage of the numerical simulation performed was the high computational cost, to which contributed the reduced structure and elements dimension, and the common soft tissues mechanical properties. Additionally, the application of explicit condition in ABAQUS software, mainly used to handle nonlinear behavior, which is the vestibular case, also increased the computation cost.

These two contributions focused on the numerical model validation, with FEM proving once again that it is a robust technique that leads to reliable results in the biomechanical field, even when specifically analyzing a small structure such as the inner ear. Furthermore, the SPH allows for a more realistic representation of the endolymph behavior. Considering the biomechanical properties of the vestibular components available in the literature, the FEM allowed to build a robust and reliable model, leading to advances of knowledge in the vestibular numerical field and rehabilitation.

Regarding the aim to accurately simulate the vestibular maneuvers, Contribution II had an active role. The use of an accelerometer was the methodology applied to collect the acceleration as a function of time during the performed movements, which was afterwards converted into displacement, to be used in the FEM simulation of the SCC. Despite some restrictions, the used approach allowed to correlate the movements performed outside by the audiologist expert with the ones occurring inside the canal at each step.

Another advantage of using an accelerometer on this study for data acquisition is the fact that, currently, most available cell phones feature built-in accelerometers. The health care provider

could obtain any accelerometer data in an easy and faster way, and afterwards directly share the output needed to perform the simulation. However, the presented methodology has some limitations, as it should also be certified to be applicable in cases where the movements happens in different spatial planes at the same time. Also, a motion picture of the performed movements could enhance the methodology, allowing for accurately extracting the position.

The main advantage of acquiring and simulate the exact movement of the vestibular system during a rehabilitation maneuver is the possibility to track the otoconia particles while moving along the pathway, inside the ducts.

In an attempt to continue developing an improved solution to vertiginous syndromes, the analysis of the free vibrations of the cupula was also performed. This analysis had also the concern of integrating the comparison of distinct numerical methods. FEM is a widely used numerical method in different backgrounds, even in some biological fields, mainly in recent years. However, the anatomical structures are commonly considered soft tissue with a non-linear shape, which often increases numerical restrictions. These constraints opened a window of opportunity to apply some meshless methods to the inner ear simulation under analysis. Therefore, the NNRPIM and RPIM approaches were used to analyze the free vibrations of the cupula and both were compared with the results from FEM. Such results are presented in Contributions IV and V.

These contributions include a wide range of numerical analyses, including mesh convergence studies of the cupula's computational model. This mesh convergence analysis was performed for the two-dimensional and three-dimensional geometrical models, using the three numerical methodologies. Even though the used software (FEMAS) was academic, it allowed to obtain robust results, while taking into account the two distinct dimensional cupula models and the particular analyzed environments, including fluid materials.

The first ten vibration modes of the cupula and respective natural frequencies were obtained, which constitutes with an important data base to increase the knowledge about the cupula behavior. Considering that balance maintenance, which is one of the most important functions of the human body, is mainly handled by this small structure, the increase of knowledge in this field is an important goal. Additionally, the influence of fluid around the cupula and the cupulolithiasis condition were

analyzed. Cupulolithiasis is an incapacitating disorder of the vestibular system, defined by the presence of otoconia attached to the cupula, inducing dizziness sensations to the patients.

One of the most interesting conclusions of this work was that the natural frequencies of the cupula are comprised in the human hearing range (20 Hz to 20,000 Hz) [50], in both situations: the case of a healthy ear and the case of cupulolithiasis. From this result, the hypothesis of dislodging the otoconia from the cupula, by inducing vibrations through a sound source, was considered. This theory further gains some strength after discovering that other authors have recently demonstrated the use of the mastoid bone vibration mechanism to solve similar cases of otoconia repositioning [51]. Using a sound source to solve the problem could be a more pleasant option for the patient. In order to evaluate this possibility, an accurate analysis of the sound frequency needed to induce cupula vibration and detachment of the otoconia, after crossing all the skin and bone layers, would have to be performed.

Additionally, this analysis supports the FEM, RPIM and NNRPIM application in studying biological structures, including soft tissues, due to their reliable results and scientific approval.

Finally, the inclusion of contribution VI in the present thesis fits the scope of the biomedical engineering doctoral program. While keeping the focus on the main vestibular symptoms such as dizziness, a statistical analysis was carried out to evaluate the influence of different intensity physical activity on developing vertiginous syndrome. The main conclusion of this contribution, carried out using the DHI and an accelerometer regarding the physical activity data collection, was that every additional minute of vigorous PA per day increases in 1.2 times the chance of developing dizziness symptoms, in young women. To further improve these results, samples from all age ranges should be used. Moreover, a cross-sectional analysis comparing patients with dizziness with a healthy control group should also be performed. Such approach could ultimately lead to results that help developing methods to prevent dizziness symptoms.

## 3.2. Conclusion and Future Work

The treatments used today for inner ear diseases are mostly based on classical vestibular rehabilitation. However, this is a set of movements, performed without any visual help of what is currently happening inside the canals, which could lead to low accuracy and consecutively bad experiences to the patients.

The main advantage of these rehabilitation solutions is the cost effectiveness, since only an audiologist expert is needed to perform the maneuvers, without any technology resources. However, considering that technological costs have been decreasing, and continue to decrease, the development of a technological solution, using computational models that have been proving to be efficient and accurate tools, with a lower cost when compared to using human resources, should be considered.

The vertiginous syndromes analysis, from a biomechanical point of view, is an important approach, in order to reduce the patient's suffering and anxiety associated with this process. The development of a computational model, in close relationship with medical professionals, such as doctors and healthcare providers, in order to research and put into practice more effective methods of diagnosis and treatment, was an achieved aim that should be further studied and refined to obtain better solutions.

In conclusion, all the proposed aims and challenges were successfully achieved, leading to a knowledge improvement in the vestibular field, mainly expressed in the presented scientific publications.

As for future work with relevance to this subject that affects the daily insecurity of a significant part of the population in an active life phase, the continuous improvement of numerical models is suggested, mainly considering finding/researching techniques to decrease the computing time. The simulation optimization process, or other improvements made possible by technological advances, are important steps mainly if they enable faster results or support the clinician's live and real-time interaction.

Additionally, with the vestibular system global model already built and validated, the next steps include obtaining the electrical potential produced by the cupula, in order to analyze the electrical impulses patterns.

Furthermore, using the available biomechanical tools, the study of other vestibular related conditions could be considered. Another branch that may have potential interest is the development of technological solutions, using computer simulation models, in order to assist or stimulate unbalance diagnoses such as posturography, videonystagmography and vestibular evoked myogenic potential.

# References

1.  Wolfe, J. M. *Sensation &amp; perception*. (Sinauer Associates, 2012).
2.  Hall, J. E. *Guyton and Hall textbook of medical physiology*. (Elsevier Inc.).
3.  Reisine, H., Simpson, J. I. & Henn, V. A geometric analysis of semicircular canals and induced activity in their peripheral afferents in the rhesus monkey. *Ann. N. Y. Acad. Sci.* **545,** 10–20 (1988).
4.  Herdman, S. *Vestibular rehabilitation*. (F.A. Davis, 2007).
5.  Wu, C. *et al.* Dynamic analysis of fluid-structure interaction of endolymph and cupula in the lateral semicircular canal of inner ear. *J. Hydrodyn. Ser. B* **23,** 777–783 (2011).
6.  Winter DA. Human balance and posture control during standing and walking. *Gait Posture* **3,** 193–214 (1995).
7.  Horak, F. B. Clinical assessment of balance disorders. *Gait Posture* **6,** 76–84 (1997).
8.  Diener, H. C. & Dichgans, J. On the role of vestibular, visual and somatosensory information for dynamic postural control in humans. *Prog. Brain Res.* **76,** 253–62 (1988).
9.  Strupp, M. & Brandt, T. Peripheral vestibular disorders. *Curr. Opin. Neurol.* **26,** 81–89 (2013).
10. Fife, T. D. *et al.* Practice Parameter: Therapies for benign paroxysmal positional vertigo (an evidence-based review): [RETIRED]. *Neurology* **70,** 2067–2074 (2008).
11. Boyer, F. C. *et al.* Vestibular rehabilitation therapy. *Neurophysiol. Clin.* **38,** 479–87 (2008).
12. Gold, D. R., Morris, L., Kheradmand, A. & Schubert, M. C. Repositioning Maneuvers for Benign Paroxysmal Positional Vertigo. *Curr. Treat. Options Neurol.* **16,** 307 (2014).
13. Kim, S. H., Jo, S.-W., Chung, W.-K., Byeon, H. K. & Lee, W.-S. A cupulolith repositioning maneuver in the treatment of horizontal canal cupulolithiasis. *Auris Nasus Larynx* **39,** 163–168 (2012).
14. Epley, J. M. New dimensions of benign paroxysmal positional vertigo. *Otolaryngol. Head Neck Surg. (1979).* **88,** 599–605
15. Epley, J. M. Positional vertigo related to semicircular canalithiasis. *Otolaryngol. Head. Neck Surg.* **112,** 154–61 (1995).
16. Burzynski, J., Sulway, S. & Rutka, J. A. Vestibular Rehabilitation: Review of Indications, Treatments, Advances, and Limitations. *Curr. Otorhinolaryngol. Rep.* **5,** 160–166 (2017).
17. Herdman, S. J. *Vestibular rehabilitation. Current opinion in neurology* **26,** (2013).
18. Zienkiewicz, O. C., Taylor, R. L. (Robert L., Zhu, J. Z., Zienkiewicz, O. C. & Zienkiewicz, O. C. *The finite element method : its basis and fundamentals*. (Elsevier Butterworth-Heinemann, 2005).
19. Reddy, J. N. (Junuthula N. *An introduction to the finite element method*. (McGraw-Hill Higher Education, 2006).
20. Bungartz, H.-J. (Hans-J. & Schäfer, M. *Fluid-structure interaction : modelling, simulation, optimisation*. (Springer-Verlag, 2006).
21. Hou, G., Wang, J. & Layton, A. Numerical Methods for Fluid-Structure Interaction — A Review. *Commun. Comput. Phys.* **12,** 337–377 (2012).
22. Ryzhakov, P. B., Rossi, · R, Idelsohn, · S R & Oñate, · E. A monolithic Lagrangian approach for fluid-structure interaction problems. **46,** 883–899 (2010).
23. Bui, H. H., Sako, K. & Fukagawa, R. Numerical simulation of soil–water interaction using smoothed particle hydrodynamics (SPH) method. *J. Terramechanics* **44,** 339–346 (2007).
24. Monaghan, J. J. Smoothed particle hydrodynamics. *Reports Prog. Phys.* **68,** 1703–1759 (2005).
25. Liu, G. R. & Liu, M. B. *Smoothed Particle Hydrodynamics*. (WORLD SCIENTIFIC, 2003). doi:10.1142/5340
26. Nguyen, V. P., Rabczuk, T., Bordas, S. & Duflot, M. Meshless methods: A review and computer implementation aspects. *Math. Comput. Simul.* **79,** 763–813 (2008).
27. T.Belytschko,Y.Krongauz,D.Organ,M.Fleming, P. K. Meshless methods: An overview and recent developments. *Comput. Methods Appl. Mech. Eng.* **139,** 3–47 (1996).
28. GU, Y. T. Meshfree Methods and their comparisons. *Int. J. Comput. Methods* **02,** 477–515 (2005).
29. Belinha, J. *Meshless Methods in Biomechanics - Bone Tissue Remodelling Analysis*. (Lecture Notes in Computational Vision and Biomechanics, Springer Netherlands, 2014).
30. Belinha, J., Araújo, A. L., Ferreira, A. J. M., Dinis, L. M. J. S. & Natal Jorge, R. M. The analysis of laminated plates using distinct advanced discretization meshless techniques. *Compos. Struct.* **143,** 165–179 (2016).
31. Wagner, J. N., Glaser, M., Brandt, T. & Strupp, M. Downbeat nystagmus: aetiology and comorbidity in 117 patients. *J. Neurol. Neurosurg. Psychiatry* **79,** 672–677 (2007).
32. von Brevern, M. & Neuhauser, H. Epidemiological evidence for a link between vertigo and migraine.

*J. Vestib. Res.* **21,** 299–304 (2011).

33. Taylor, J. & Goodkin, H. P. Dizziness and vertigo in the adolescent. *Otolaryngol. Clin. North Am.* **44,** 309–21, vii–viii (2011).

34. Strupp, M. *et al.* Pharmacotherapy of vestibular and ocular motor disorders, including nystagmus. *J. Neurol.* **258,** 1207–1222 (2011).

35. Wipperman, J. Dizziness and Vertigo. *Prim. Care Clin. Off. Pract.* **41,** 115–131 (2014).

36. Moreira, M. D. *et al.* Prevalência e associações da vertigem posicional paroxística benigna em idosos. *Rev. CEFAC* **16,** 1533–1540 (2014).

37. Penger, M., Strobl, R. & Grill, E. Country-specific and individual determinants of dizziness in Europe: results from the Survey of Health Ageing and Retirement in Europe (SHARE). *Public Health* **149,** 1–10 (2017).

38. Felipe, L., Cunha, L. C. M., Cunha, F. C. M., Cintra, M. T. G. & Gonçalves, D. U. Presbivertigem como causa de tontura no idoso. *Pró-Fono Rev. Atualização Científica* **20,** 99–104 (2008).

39. Florence, C. S. *et al.* Medical Costs of Fatal and Nonfatal Falls in Older Adults. *J. Am. Geriatr. Soc.* **66,** 693–698 (2018).

40. Selva, P., Morlier, J. & Gourinat, Y. Toward a three-dimensional finite-element model of the human inner ear angular accelerometers sensors. *International Journal for Computational Vision and Biomechanics (IJCV & B)* (2010).

41. Belinha, J., Azevedo, J. M. C., Dinis, L. M. J. S. & Natal Jorge, R. M. The Natural Neighbor Radial Point Interpolation Method Extended to the Crack Growth Simulation. *Int. J. Appl. Mech.* **08,** 1650006 (2016).

42. Klenck, C. A. The dizzy athlete. *Curr. Sports Med. Rep.* **6,** 25–31 (2007).

43. Giacomini, P. G., Ferraro, S., Di Girolamo, S., Villanova, I. & Ottaviani, F. Benign paroxysmal positional vertigo after intense physical activity: a report of nine cases. *Eur. Arch. Oto-Rhino-Laryngology* **266,** 1831–1835 (2009).

44. Lovell, M. R. *et al.* Measurement of Symptoms Following Sports-Related Concussion: Reliability and Normative Data for the Post-Concussion Scale. *Appl. Neuropsychol.* **13,** 166–174 (2006).

45. Rothney, M. P., Apker, G. A., Song, Y. & Chen, K. Y. Comparing the performance of three generations of ActiGraph accelerometers. *J. Appl. Physiol.* **105,** 1091–1097 (2008).

46. Trost, S. G., McIver, K. L. & Pate, R. R. Conducting accelerometer-based activity assessments in field-based research. *Med. Sci. Sports Exerc.* **37,** S531-43 (2005).

47. TROIANO, R. P. *et al.* Physical Activity in the United States Measured by Accelerometer. *Med. Sci. Sport. Exerc.* **40,** 181–188 (2008).

48. Vibert, D., Redfield, R. C. & Häusler, R. Benign Paroxysmal Positional Vertigo in Mountain Bikers. *Ann. Otol. Rhinol. Laryngol.* **116,** 887–890 (2007).

49. Katsarkas, A. Benign paroxysmal positional vertigo (BPPV): idiopathic versus post-traumatic. *Acta Otolaryngol.* **119,** 745–9 (1999).

50. Barmack, N. H. Central vestibular system: vestibular nuclei and posterior cerebellum. *Brain Res. Bull.* **60,** 511–541 (2003).

51. Griech, S. F. & Carroll, M. A. The use of mastoid vibration with canalith repositioning procedure to treat persistent benign paroxysmal positional vertigo: A case report. *Physiother. Theory Pract.* **34,** 894–899 (2018).

# Appendix I

# DIZZINESS HANDICAP INVENTORY (DHI)

Gary P. Jacobson; Craig W. Newman, 1990.

Traduzido, validado e adaptado para a língua e população portuguesa por Dr. Vaz Garcia, Ft. Cristina Luzio, Ft. Teresa Benzinho e Dr. Gabão Veiga, 2006.

Este questionário é de auto-preenchimento. O objectivo é identificar as dificuldades que sente no dia-a-dia, devido às vertigens e/ou ao seu desequilíbrio.

Responda a cada pergunta, tendo em conta exclusivamente a influência das vertigens e/ou desequilíbrio, durante o período relativo às quatro semanas anteriores.

| | Não, nunca | Raramente | Por vezes | Frequentemente | Sim, permanentemente |
|---|---|---|---|---|---|
| | 0 | 1 | 2 | 3 | 4 |
| 1. As suas queixas agravam-se quando olha para cima? | | | | | |
| 2. Sente-se frustrado / decepcionado por causa do seu problema? | | | | | |
| 3. Limita as suas deslocações de trabalho ou lazer, por causa das suas queixas? | | | | | |
| 4. O seu problema agrava-se ao fazer compras no supermercado, hipermercado ou centro comercial? | | | | | |
| 5. Devido ao seu problema, tem dificuldade em deitar-se e levantar-se da cama? | | | | | |
| 6. As suas queixas limitam-no significativamente em actividades sociais, tais como: jantar fora, ir ao cinema, dançar ou ir a festas? | | | | | |
| 7. Tem dificuldade em ler por causa das suas queixas? | | | | | |
| 8. As suas queixas agravam ao realizar actividades mais exigentes, tais como: desporto, dançar ou tarefas domésticas (varrer, arrumar a loiça...)? | | | | | |
| 9. Tem receio em sair de casa sozinho, por causa do seu problema? | | | | | |
| 10. Devido ao seu problema, já se sentiu embaraçado perante outras pessoas? | | | | | |
| 11. As suas queixas agravam-se com movimentos rápidos / bruscos da cabeça? | | | | | |
| 12. Evita alturas, por causa das suas queixas? | | | | | |
| 13. As suas queixas agravam-se quando se vira na cama? | | | | | |
| 14. Devido às suas queixas, tem dificuldade em executar tarefas domésticas ou de lazer, que exijam maior esforço? | | | | | |
| 15. Tem receio que, devido ao seu problema, as pessoas possam pensar que está sob o efeito de álcool ou droga? | | | | | |
| 16. Tem dificuldade em dar um passeio sozinho? | | | | | |

| | | | | | |
|---|---|---|---|---|---|
| 17. As suas queixas agravam-se quando caminha ao longo de um passeio? | | | | | |
| 18. Devido ao seu problema, tem dificuldade em concentrar-se? | | | | | |
| 19. Devido às suas queixas, é-lhe difícil andar pela casa às escuras? | | | | | |
| 20. Devido ao seu problema, tem receio em ficar sozinho em casa? | | | | | |
| 21. Sente-se limitado / incapacitado, devido ao seu problema? | | | | | |
| 22. O seu problema tem afectado o seu relacionamento com a família ou amigos? | | | | | |
| 23. Sente-se deprimido, por causa do seu problema? | | | | | |
| 24. As suas queixas afectam as suas responsabilidades profissionais, domésticas ou familiares? | | | | | |
| 25. As suas queixas agravam-se quando se inclina para a frente? | | | | | |

| Física | Funcional | Emocional |
|---|---|---|
| 1: | 3: | 2: |
| 4: | 5: | 9: |
| 8: | 6: | 10: |
| 11: | 7: | 15: |
| 13: | 12: | 18: |
| 17: | 14: | 20: |
| 25: | 16: | 21: |
| | 19: | 22: |
| _____ | 24: | 23: |
| 28 | _____ | _____ |
| | 36 | 36 |
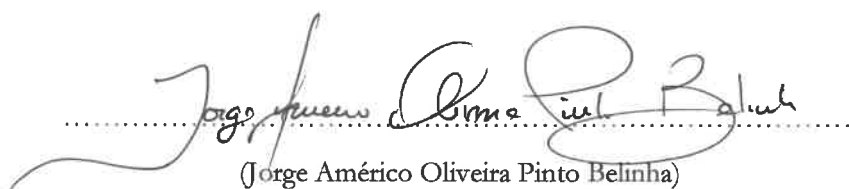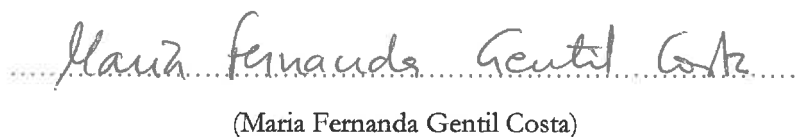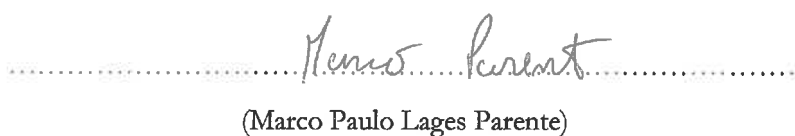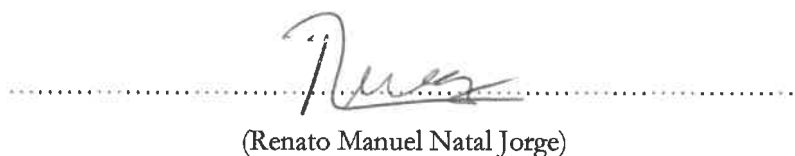
136

# Appendix II

138

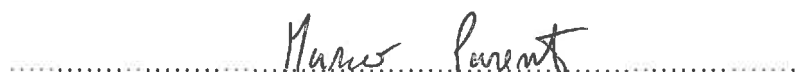## Autorização de compilação

Jorge Américo Oliveira Pinto Belinha, Maria Fernanda Gentil Costa, Marco Paulo Lages Parente e Renato Manuel Natal Jorge na qualidade de co-autores do artigo "An alternative 3D numerical method to study the biomechanical behaviour of the human inner ear semicircular canal" publicado na revista *Acta of Bioengineering and Biomechanics*, declaram que autorizam a inclusão do mesmo na dissertação de doutoramento da candidata Carla Bibiana Monteiro França Santos, intitulada "Study of Vestibular Rehabilitation in Vertiginous Syndrome using a Biomechanical Approach".

Porto e FEUP, 25 de Janeiro 2019,

(Jorge Américo Oliveira Pinto Belinha)

(Maria Fernanda Gentil Costa)

(Marco Paulo Lages Parente)

(Renato Manuel Natal Jorge)

## Autorização de compilação

Jorge Américo Oliveira Pinto Belinha, Maria Fernanda Gentil Costa, Bruno André Faria Areias, Marco Paulo Lages Parente e Renato Manuel Natal Jorge na qualidade de co-autores do artigo "A computational framework to simulate the endolymph flow due to vestibular rehabilitation maneuvers assessed from accelerometer data" publicado na revista *Computer Methods in Biomechanics and Biomedical Engineering*, declaram que autorizam a inclusão do mesmo na dissertação de doutoramento da candidata Carla Bibiana Monteiro França Santos, intitulada "Study of Vestibular Rehabilitation in Vertiginous Syndrome using a Biomechanical Approach".

Porto e FEUP, 25 de Janeiro 2019,

(Jorge Américo Oliveira Pinto Belinha)

(Maria Fernanda Gentil Costa)

(Marco Paulo Lages Parente)

(Bruno André Faria Areias)

(Renato Manuel Natal Jorge)

## Autorização de compilação

Jorge Américo Oliveira Pinto Belinha, Maria Fernanda Gentil Costa, Marco Paulo Lages Parente, Maria Margarida Fernandes Machado e Renato Manuel Natal Jorge na qualidade de co-autores do artigo "Simulation of Epley Maneuver using an Enhanced Vestibular System Computational Model developed using a Realistic Anatomical Human Shape" submetido para publicação numa revista internacional, declaram que autorizam a inclusão do mesmo na dissertação de doutoramento da candidata Carla Bibiana Monteiro França Santos, intitulada "Study of Vestibular Rehabilitation in Vertiginous Syndrome using a Biomechanical Approach".

Porto e FEUP, 25 de Janeiro 2019,

(Jorge Américo Oliveira Pinto Belinha)
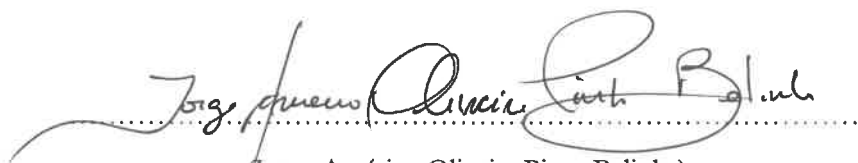
(Maria Fernanda Gentil Costa)

(Marco Paulo Lages Parente)

(Maria Margarida Fernandes Machado)

(Renato Manuel Natal Jorge)

## Autorização de compilação

Jorge Américo Oliveira Pinto Belinha, Maria Fernanda Gentil Costa, Marco Paulo Lages Parente, e Renato Manuel Natal Jorge na qualidade de co-autores do artigo "The free vibrations analysis of the cupula in the inner ear using a natural neighbor meshless method" publicado na revista *Engineering Analysis with Boundary Elements*, declaram que autorizam a inclusão do mesmo na dissertação de doutoramento da candidata Carla Bibiana Monteiro França Santos, intitulada "Study of Vestibular Rehabilitation in Vertiginous Syndrome using a Biomechanical Approach".

Porto e FEUP, 25 de Janeiro 2019,

(Jorge Américo Oliveira Pinto Belinha)

(Maria Fernanda Gentil Costa)

(Marco Paulo Lages Parente)

(Renato Manuel Natal Jorge)

# Autorização de compilação

Jorge Américo Oliveira Pinto Belinha, Maria Fernanda Gentil Costa, Marco Paulo Lages Parente, e Renato Manuel Natal Jorge na qualidade de co-autores do artigo "Analyses of Free Vibrations of the Cupula in the Human Vestibular System during Cupulolithiasis: a Meshless approach" submetido para publicação numa revista internacional, declaram que autorizam a inclusão do mesmo na dissertação de doutoramento da candidata Carla Bibiana Monteiro França Santos, intitulada "Study of Vestibular Rehabilitation in Vertiginous Syndrome using a Biomechanical Approach".

Porto e FEUP, 25 de Janeiro 2019,


(Jorge Américo Oliveira Pinto Belinha)

(Maria Fernanda Gentil Costa)

(Marco Paulo Lages Parente)
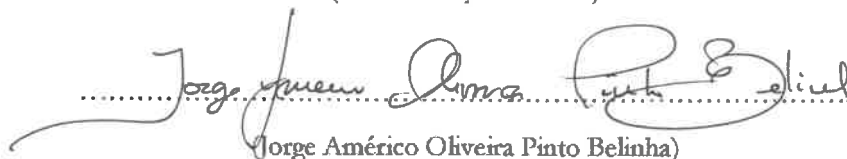
(Renato Manuel Natal Jorge)

## Autorização de compilação

Thuane Huyer da Roza, Jorge Américo Oliveira Pinto Belinha, Maria Fernanda Gentil Costa, e Renato Manuel Natal Jorge na qualidade de co-autores do artigo "Is the severity of dizziness symptoms depending on the physical activity intensity?" submetido para publicação numa revista internacional, declaram que autorizam a inclusão do mesmo na dissertação de doutoramento da candidata Carla Bibiana Monteiro França Santos, intitulada "Study of Vestibular Rehabilitation in Vertiginous Syndrome using a Biomechanical Approach".

Porto e FEUP, 25 de Janeiro 2019,

..................................................................................................................
(Thuane Huyer da Roza)

..................................................................................................................
(Jorge Américo Oliveira Pinto Belinha)

..................................................................................................................
(Maria Fernanda Gentil Costa)

..................................................................................................................
(Renato Manuel Natal Jorge)

144